Master's thesis

NTNU
Norwegian University of Science and Technology
Faculty of Engineering
Department of Mechanical and Industrial Engineering

Steinar Hunskaar

Structural Integrity of Bimaterials Fabricated via Fused Deposition Modeling

Master's thesis in Mechanical Engineering
Supervisor: Seyed Mohammad Javad Razavi
Co-supervisor: Zhuo Xu
June 2022

NTNU
Kunnskap for en bedre verden

Steinar Hunskaar

Structural Integrity of Bimaterials Fabricated via Fused Deposition Modeling

Master's thesis in Mechanical Engineering
Supervisor: Seyed Mohammad Javad Razavi
Co-supervisor: Zhuo Xu
June 2022

Norwegian University of Science and Technology
Faculty of Engineering
Department of Mechanical and Industrial Engineering

NTNU
Norwegian University of
Science and Technology

Preface

This master's thesis was written during the spring of 2022 as the final work of a two year masters of science program of mechanical engineering at the department of mechanical and industrial engineering at the Norwegian University of Science and Technology. The work presented serves as an continuation of my specialization project "Hybrid Multifunctional Printing of Mechanical Parts". The thesis was written under the supervision of Associate Professor Seyed Mohammad Javad Razavi.

I would like to express my deepest gratitude to Associate Professor Seyed Mohammad Javad Razavi. Your theoretical guidance, expertise and input has been greatly appreciated during this semester.

I would also like to thank Zhuo Xu for the equipment training, guidance and assistance i have received during the project.

Abstract

After successful fabrication of mechanically strong bimaterials during the specialization project, this master thesis is defined on a wide range of studies including fabrication and mechanical characterisation of FDM bimaterials. Bimaterial Semi Circular Bend (SCB) specimen were manufactured using same filament material with different colours before being tested under a wide range of mixed mode loading conditions to evaluate the inter-material bonding strength of the fabricated parts. Single material SCB-specimen were also produced and tested to compare the results and to measure the strength reduction due to the use of a dual nozzle setup. The obtained experimental results were then compared with theoretical fracture prediction using Strain Energy Density to evaluate the capability of numerical tools in prediction of failure in the printed bimaterial parts.

Sammendrag

Etter vellyket fremstilling av mekanisk sterke bimaterialer under spesialiseringsprosjektet er denne masteroppgaven definert på ett bredt spekter av studier inkludert fabrikasjon og mekanisk karakterisering av 3D-printede bimaterialer. Bimateriale semi sirkulære bøyningsprøver ble produsert av ett materiale i 2 forskjellige farger før de ble testet under ett bredt spekter av blandede modusbelastningsforhold for å evaluere bindestyrken mellom materialene til de fremstilte delene. Enkeltmateriale semi sirkulære bøyningsprøver ble også produsert og testet for å sammenligne resultatene og for å måle styrkereduksjonen på grunn av et dobbeltdyseoppsett. De oppnådde eksperimentelle resultatene ble deretter sammenlignet med teoretisk bruddprediksjon ved bruk av tøyningsenergitetthet for å evaluere evnent numeriske verktøy har til å forutsi brudd i de produserte bimateriale delene.

List of Figures

1 Three modes of fracture [5] 2
2 CreatBot f430 printer[33]. 10
3 Two dogbone halves loaded in Cura and aligned for multi-material printing. 12
4 One laying and one standing SCB disc in Cura. 12
5 Dimentions of SCB-specimen disc. 13
6 Minimum angle of overhang while printing notch tip. 14
7 Difference between a ”red half lower” (left) and a ”grey half lower” (right) SCB-specimen. 14
8 Dimensions of ASTM D638 Type 1 tensile test specimen[36]. 17
9 Result of inconsistent automatic bed levelling. 19
10 4 Laying SCB-specimen in printer. 20
11 Oval notch in laying SCB-specimen. 20
12 Adjustment of standing SCB-specimen support structure. 21
13 Porosity in standing bimaterial interface. 21
14 Forcing prime tower throughout the entire print. 22
15 Under-extrusion at the beginning of an extrusion-path. 22
16 SCB-specimen with slanted cut after laser-cutting. 23
17 SCB-disc cutting fixture. 24
18 SCB-disc and alignment fixture in laser cutter. 25
19 Face milling. [40] 25
20 TOS FA3A-U mill. 26
21 SCB-specimen fixture. 27
22 SCB-specimen loaded in fixture with vice. 27
23 SCB-specimen mounted in mill and machined. 28
24 Getting the correct crack depth with the specimen fixture. 29
25 Angled notch alignment tools. 30
26 A 40° SCB-specimen getting aligned for crack sharpening. 30
27 SCB-specimen prepared with speckle pattern for DIC capturing. 31
28 SCB-specimen alignment tool for 3-point bend fixture. 32
29 SCB-specimen placed in front of the alignment tool. 32
30 SCB-specimen sliding during testing. 33
31 Instron test system with and without extensions. 33

32 40° SCB-specimen which did not fracture during testing. 34
33 0 Degree specimen partitioned in Abaqus. 35
34 SCB-specimen with boundary conditions and load in Abaqus. 36
35 SCB-specimen meshed in Abaqus. 36
36 SCB-specimen meshed in Abaqus. 39
37 Elastic strain energy within control volume simulated in Abaqus. 39
38 Mean fracture load of SCB-specimen where crack initiated from the crack tip. 41
39 Mean fracture load for all SCB-specimen. 42
40 Fracture load of laying compared to standing specimen. 43
41 Mean fracture load for bimaterial specimen with ”grey half lower” compared to ”red half lower”. 44
42 Ultimate tensile strength of red, grey and bimaterial dogbones printed in laying and standing orientation. 47
43 Young’s modulus of red, grey and bimaterial dogbones printed in laying and standing orientation. 48
44 Poisson’s ratio of red and grey dogbones printed in laying and standing orientation. 48
45 Strain field for SCB-specimen 1, 6, 10, 13, 17 and 22. 50
46 Strain field for SCB-specimen 26, 29, 33, 37, 41 and 45. 51
47 Strain field for SCB-specimen 49, 56, 57, 61, 67 and 71. 52
48 Strain field for SCB-specimen 74, 78, 81, 87, 89 and 93. 53
49 Strain field for SCB-specimen 97, 101, 105, 109, 113 and 117. 54
50 Crack path of laying bimaterial SCB-specimen. 55
51 Crack path of laying red and grey SCB-specimen. 56
52 Crack path of standing bimaterial SCB-specimen. 57
53 Crack path of standing red and grey SCB-specimen. 58
54 Fracture surface of specimen 36 and 50. 60
55 Fracture surface of specimen 58 and 60. 60
56 Fracture surface of specimen 1, 2, 3 and 4. 62
57 Fracture surface of specimen 89, 90, 91 and 92. 62
58 Fracture surface of specimen 105, 106, 107 and 108. 63
59 Fracture surface of specimen 61, 62, 63 and 64. 63
60 Overview of the laying tensile specimen after testing. 65
61 Fracture surface of laying red tensile specimen, T2. 65

62 Fracture surface of laying grey tensile specimen, T5. 66
63 Fracture surfaces of laying bimaterial tensile specimen, T8. 66
64 Overview of the standing tensile specimen after testing. 67
65 Fracture surface of standing grey tensile specimen, T12. 67
66 Fracture surface of standing red tensile specimen, T14. 67
67 Fracture surface of standing bimaterial tensile specimen, T16. 68

List of Tables

1 Material and printing properties of PLA[34][35]. (*value not specific to 3DNet PLA) 11

2 List of laying SCB-specimen. Specimen highlighted in green were tested with DIC. 15

3 List of standing SCB-specimen. Specimen highlighted in green were tested with DIC. 16

4 Changes made to the infill motion settings. 23

5 Laser cutting settings used for cutting SCB-specimen. 24

6 Stress intensity factor of SCB-specimen with different crack angles. . . . 45

7 Fracture Toughness of the material in different conditions. 45

8 Fracture prediction using strain energy density. 46

9 Results from mesh sensitivity analysis for ELSE simulation of 0° SCB-specimen. 47

Table of Contents

Preface i

Abstract iii

Sammendrag v

List of Figures vii

List of Tables xi

1 Introduction 1

1.1 Project Scope 1

1.2 Thesis Structure 1

2 Theory 2

2.1 Fracture Mechanics 2

2.1.1 Semi-Circular Bend Test 3

3 Literature Review 4

3.1 FDM Printing 4

3.1.1 Important Process Parameters 4

3.2 Multi-Material Printing 6

3.3 Relevant Studies 7

4 Method 10

4.1 Preliminary Work 10

4.2 Specimen Fabrication 10

4.2.1 Printer 10

4.2.2 Software 10

4.2.3 Filament 11

4.2.4 Multi-Material Printing in Cura 11

4.3 Fracture Specimen 11

4.3.1 Printing Orientation 12

4.3.2 SCB-specimen Disc 13

4.3.3 Bimaterial SCB-specimen 13

4.3.4 Overview of produced SCB specimen 14

4.4 Tensile Specimen 17

4.5 Printing 17
4.5.1 Automatic Bed Levelling 18
4.5.2 Laying Specimen 18
4.5.3 Standing Specimen 18
4.5.4 Porosity in Standing Specimen 20
4.5.5 Underextrusion in Infill 21
4.6 Laser Cutting 23
4.7 Facing of Cut 24
4.8 Crack Sharpening 28
4.9 Digital Image Correlation 29
4.10 Fracture Testing 31
4.11 Stress Intensity Factor 34
4.12 Fracture Toughness 36
4.13 Fracture Prediction Using Strain Energy Density 37
4.13.1 Elastic Strain Energy Density 38
4.13.2 Mesh Sensitivity analysis 40
4.14 Tensile Testing 40

5 Results **40**

5.1 Fracture Load 40
5.2 Stress Intensity Factor 45
5.3 Fracture Toughness 45
5.4 Fracture Prediction 45
5.5 Mesh Sensitivity Analysis 45
5.6 Material Properties 47
5.6.1 Ultimate Tensile Strength 47
5.6.2 Young's Modulus 48
5.6.3 Poisson's Ratio 48
5.7 Strain Fields SCB-Specimen 49
5.8 Fracture Path 55

6 Discussion **59**

6.1 Fracture Loads 59
6.2 Fracture Toughness 61

6.3 Fracture Prediction 64
6.4 Mesh Sensitivity Analysis 64
6.5 Material Properties 64
6.5.1 Ultimate Tensile Strength 64
6.5.2 Young's Modulus 68
6.5.3 Poisson's Ratio 68
6.6 Strain Fields and Crack Path 68

7 Conclusion 69

7.1 Further work 69

Reference list 70

Appendix 75

A Cura Settings Nozzle 1 76

B Cura Settings Nozzle 2 84

C Fracture Specimen Manufacturing Data 93

D Code 96

E Fracture Loads 102

F Average Strain Energy Density 105

1 Introduction

Additive manufacturing, more commonly known as three dimensional (3D) printing, is a process where physical objects are made from a 3D-model from the ground up. The objects are successively created layer-by-layer in a process where material is added to the object layer by layer. There are different types of 3D-printers which utilise varying print methods, which makes it possible to 3D-print in almost any material [1]. Additive manufacturing differs from traditional manufacturing where material is subtracted from a piece of material (subtractive manufacturing) or casting [2]. 3D-printers have been around for decades, but since the expiration of a patent protecting the fused deposition modelling (FDM) method in 2009 [3], the development and accessibility of 3D-printers has increased exponentially. Due to the gain in accessibility, the path from idea to physical product has been streamlined, making it a powerful tool for engineers. It makes it possible to produce prototypes, spare parts and finished products at a fraction of the time, compared to through professional manufacturers.

This project came to life after NTNU purchased a 3D-printer capable of bimaterial printing to use as a tool for research within incorporation of bimaterials for fabrication of damage tolerant components. The idea is that the introduction of soft material in specific locations of a part, can create a dampener for energy which can increase the load bearing capacity and fatigue life of the part.

1.1 Project Scope

The purpose of this project is to produce and evaluate bimaterial semi circular bend (SCB) specimen manufactured with a multi nozzle 3D-printer, made of same material but different coloured filament. The fabricated specimen will be tested under a broad range of mixed mode loading conditions to evaluate the inter-material bonding strength of the parts. Single material SCB-specimen are also to be produced to evaluate any change in strength due to the use of a dual-nozzle printer. The results will then be compared to predicted fracture loads using strain energy density (SED) to evaluate the compatibility of these numerical tools.

1.2 Thesis Structure

The reports begins with a brief introduction of relevant theory in Section 2 before a review of relevant literature to the thesis is evaluated in Section 3. Then the manufacturing and post processing of the specimen as well as FEA simulations needed to calculate the results are explained in Section 4. The testing of SCB test specimen is also explained in Section 4. The results are reported in Section 5 while the discussion of the results are located in Section 6. Finally, a conclusion and overview of further work is presented in Section 7

2 Theory

This section contains a brief explanation of the theoretical background used in this thesis.

2.1 Fracture Mechanics

Fracture mechanics is the field of mechanics where crack propagation in materials are studied. The presence of cracks in materials can weaken it, causing the material to fail at stresses below the yield point of the material. The fracture toughness, K_{Ic}, is a measure of a material's ability to withstand failure due to a crack. A good understanding fracture mechanics is important because material flaws and cracks appear frequently in materials. [4]

In fracture mechanics, there are three modes of fracture, illustrated in Figure 1, where mode I is described as opening mode (K_I), mode II is shearing mode (K_{II}) and mode III is tearing mode (K_{III}) [4]. Mode I and 2 are in plane fracture modes which are fracture modes which are present in the fracture experiments performed in this project.

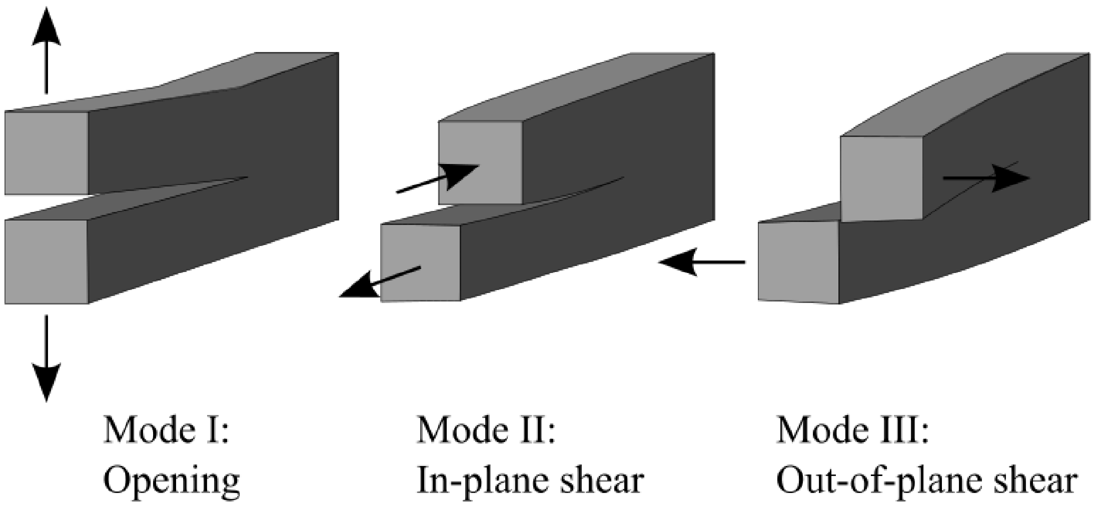

Figure 1: Three modes of fracture [5]

.

In fracture mechanics the stress intensity factor (K) is an commonly used quantity. K is used to describe the stress intensity near the tip or crack of a notch. The magnitude of K is dependant on the geometry, size, location and applied stress of a crack or notch. A material can inherent a crack without fracture occuring as long as the magnitude of K is below a critical value K_c. The K_c value for a material varies depending on the thickness of a material. The critical value of K_c decreases until the material reaches a thickness where the material has plane strain properties. When a material has the properties of plane strain, the critical fracture toughness is then denoted K_{Ic}, which is called the plane strain fracture tougness.[4]

The experiments done in this project have been performed under the assumption that the specimen have a thickness where plane strain conditions occur.

In this thesis, the fracture toughness of the bimaterial interface of additively manufactured parts are determined using an experimental approach. Using a FEA software, the K_1 values for the specimen are calculated when the specimen is loaded with a 1N unit load. Using the K_1 values from these simulations, the K_Ic values for the material can be determined with Equation 1, where P is the experimental fracture load.

$$K_{Ic} = K_I * P \tag{1}$$

2.1.1 Semi-Circular Bend Test

Semi circular bend (SCB) specimen were produced and tested to determine the fracture toughness of the materials in this thesis. SCB-specimen were chosen for the fracture tests because of its simple geometry making it easy to produce. It also has the possibility to produce mode I, mode II as well as mixed mode I and 2 fracture cases, determined by the angle of the crack.

3 Literature Review

3.1 FDM Printing

Today, the most common additive manufacturing technique on the market is a FDM-process [1]. This is due to the cost efficiency of the materials and printers, as well as the user-friendliness of the process [1]. FDM-printers work by extruding melted material thorough a nozzle. Most consumer and commercial FDM-printers can only print thermoplastics today [1]. The material, also called filament, is most often supplied as a spooled wire, although some printers can be fed with thermoplastic-pellets. The filament comes in a wide range of different polymers such as polylactic acid (PLA), acrylonitrile butadiene styrene (ABS), polycarbonate (PC), Nylon [1] and many more. There are also composite filaments available such as PLA mixed with wood fibres, metal dust or carbon fibres. The filament is fed by a feeder motor in to the print head, which consists of a heating element and a nozzle. After being heated to its melting point, the filament gets extruded along a predefined path on the print bed. The path is made from a 3D computer aided design (CAD) model by a slicing software. The slicing software divides the model in to thin slices and generates a list of code, which tells the printer how to move and operate. The code is called G-code, and is the most common programming language for computer numerical control (CNC) machines, and tells the printer where to move, what temperature to print at and what speed the filament should be extruded at [6].

3.1.1 Important Process Parameters

Although 3D-printing is a powerful tool for quick part production, it does come with some shortcomings compared to traditionally manufactured components. Because the part is being produced layer-by-layer, 3D-printed parts have reduced mechanical properties, surface quality and dimensional accuracy compared to equal parts manufactured in a traditional way [7]. These shortcomings can become even bigger if the print parameters aren't optimised. In order to maximise the quality and performance of 3D-printed parts and reduce post-production work, a good understanding in process parameters and how affects the end result is important[7].

Because of the nature of FDM, any 3D-printed part will have an anisotropic behaviour [8]. This is because the weakest part of a FDM 3D-printed part is in between the layer borders. Therefore, a 3D-printed part which have stress in the direction of the print layers, will withstand a larger load than an identical part where the load is normal to the print layers [8]. To reduce the amount of anisotropy, the process parameters must be adjusted to increase the interlayer cohesion of the individual print layers.

The FDM-process has many process parameters which decides printing efficiency, geometry and characteristics [7]. For an advanced user, there are hundreds of different process parameters which can be manipulated to decide how the printer will operate. However, some parameters have a greater influence in the finished result than other. It is therefore more important to have a good understanding of these parameters. The following list contains some of the more important process parameters to consider when configuring a print.

- Print orientation: Print orientation is important to consider when printing a part. it can impact both surface finish and mechanical performance. For instance, a part loaded at multiple axis, should have the greatest force act along the print layers in order to reduce the chance of failure by layer separation [9].
- Extrusion temperature: Correct extrusion temperature is important to ensure optimal cohesion between print layers. If the temperature is too low, the print layers will not fuse properly together. On the other hand, having the extrusion temperature too high will result in a dimensional inaccurate print result. In a paper by Yadav, Chhabra, Gupta *et al.* [10], it is investigated how extrusion temperature influence the strength of 3D-printed PLA and ABS.
- Ambient temperature: Ambient temperature can be influenced by a heated print bed and a heated print chamber. Like extrusion temperature, ambient temperature can influence layer cohesion. A printer with high ambient temperature will maintain temperature in the deposited layers, making the temperature difference between the extruded material and previous layer smaller, resulting in better layer cohesion [11]. A lower temperature difference between deposited and extruded material will also reduce the residual stress, reducing the warping of the print. Wang, Xi and Jin [12] showed that there is a linear correlation between print warping and the chamber temperature during the print.
- Cooling-fan speed: 3D-printing with a cooling fan ensures that the deposited material solidifies at the point of extrusion, which reduces the amount of stringing and sagging when bridging. It also makes it possible to print with a higher extrusion temperature, without sacrificing the geometrical accuracy of the finished part. However, the fan speed cant be too high. Excessive airflow will cool the previous layer too quickly, which can reduce the layer cohesion.
- Infill density and pattern: To save time and reduce material costs, the infill density can be reduced. Although a reduction in infill density comes at the cost of strength, it does not decrease linearly with the infill density. In a study conducted by Alani, Othman and Ali [13], the compressive strength of a test specimen is compared relative to its infill density. Different infill patterns can also increase the strength of a 3D-printed part without increasing the infill density. In a comprehensive study performed by Pandžić, Hodzic and Milovanović [14], the tensile strength of 130 PLA test specimens with different infill pattern and density was compared in order to determine the most effective infill pattern. Although this experiment was conclusive, the most effective infill pattern for a different load case might differ.
- Layer thickness: The increase of layer thickness is an effective method to decrease the printing time of a part, although it can come at the cost of the part strength. Luzanin, Movrin and Plancak [15] showed that the layer thickness had

a effect on maximum flexural force, during a three-point bend test. Here, a increase in layer thickness decreased the maximum withstood load. Similar results was showed by Wu, Geng, Li *et al.* [16] and Rajpurohit and Dave [17] in their studies. An increase in layer thickness will also reduce the geometrical accuracy, as demonstrated by Polák, Sedláček and Raz [18] in their study.

- Print speed: The speed of the printer nozzle is another parameter which can reduce the time of a print. Hashemi Sanatgar, Campagne and Nierstrasz [19] discovered that the adhesion force between PLA and a textile were the lowest at the slowest and fastest possible printing speed, with the highest adhesion force being in the middle of the speed range. Yang and Yeh [20] on the other hand showed that flexural and compressive properties increased when printer speed was lowered while tensile was unaffected by the speed, while Christiyan, Chandrasekhar and Venkateswarlu [21] showed that tensile and flexural strength increased when the printing speed was lowered.
- Extrusion width: Changing to a extrusion nozzle with a wider opening will reduce the print time and can also increase the strength of the part. The wider nozzle makes it possible to reduce the amount of passes needed to print a part, resulting in a less porous part [22]. The reduced porosity in return makes a larger cohesion area between layers, which makes the part stronger [23]. Although the adhesion strength can be improved, the larger extrusion width makes the XY resolution and the geometrical accuracy of the printer smaller.

3.2 Multi-Material Printing

Multi-material FDM is 3D-printing where the finished part is made out of two or more materials. A multi-material printer offers the possibility to produce aesthetically pleasing prints with multiple colours, or potentially improved mechanical properties. For instance, a water soluble material can be used as a support material, making the post process work of cleaning the support easy. It also makes it possible to print support at tight areas where it would be difficult to remove if it were to be made of PLA. Even though printing with multiple materials have great potential and advantages, it comes with a set of challenges which increases the difficulty of the printing operation.

There are different types of multi-material FDM printers. Mainly, single- and multi-nozzle printers. A single nozzle printer has a mechanism which changes what filament is being fed in to the extruder. Although there is no physical limitation as to how many materials a single-nozzle printer can print, there are challenges tied up with using a shared nozzle. When printing with different coloured filament, the material being extruded after a filament change will be a colour mixture of the current and last filament. This can be worked around by either printing a ”purge tower”, which makes the printer extrude a layer on to a throw-away structure, or program the printer to print the infill of the part after a material change, and before any visible material is extruded. If the single nozzle printer is used to print filament with different polymers, the selected material should have thermal properties close to each other. For instance, PLA printed with PEEK can cause problems, as the auto ignition temperature of PLA is lower than the recommended printing temperature of PEEK [24][25]. Lastly, the filament change can be a slow operation, costing time if having to be done often.

With a multi-nozzle printer, each nozzle's parameters can be set to work optimally with its designated filament. The material is ready at all times, which saves time and there is no cross-contamination of filaments. It does however require more work when calibrating and configuring the printer. Each nozzle must be at the exact same height in order to ensure proper layer adhesion and to prevent the nozzles from crashing in to the extruded and solidified material. The location of the nozzles must also be calibrated in relation to each other in order to achieve seamless material transitions.

3.3 Relevant Studies

To analyse how various print variables influence the strength of a 3D-printed part, Kim, Park, Kim *et al.* [26] has compared the strength of a single material test specimen with varying print variables. The purpose if the experiment was to learn how to optimise the strength of a 3D-printed part. There was also performed tensile tests on a dual material test specimen with varying material ratio and structural arrangement in order to investigate the effectiveness of dual material printed products. During the experiment, an analysis of variance showed that voids and overlaps may occur in the material boundary which could cause an early failure. In order to solve this problem, the structural arrangement was modified to disperse the different materials throughout the cross section of the test specimen. This increased the adhesion area in between the material borders, leading to increased strength.

Multi-material printing opens the opportunity to strengthen or reinforce areas of a component which experiences large amount of stress or strain. Roger and Krawczak [27] has published a study which aims at improving the design of 3D-printed structures using topological optimisation. This is done by either filling or replacing over-stressed parts of the structure with a different material with improved mechanical properties. This can potentially increase the strength or lifetime of a part, without changing the physical dimensions. One of the difficulties of printing with multiple materials in a single part is to ensure a strong interface between different materials. This issue is also addressed in this paper. The authors found that when printing bimaterial mechanical parts, the strength of the part is limited by the strength of the material interface. A good understanding of how to achieve a strong interface is crucial in order to maximise the total strength of the part.

Another example of reinforcing stress and strain exposed areas can be seen in a paper published by Wang, Chang, Chen *et al.* [28] where a dual extrusion 3D-printer is used to modify the mechanical properties of an auxetic metamaterial. The auxetic behaviour is achieved by a specific structure where large strain might occur. Using a single material design makes the Young's modulus and Poisson's dependant of each other. However, when replacing the parts of the structure which is exposed to large strain, the mechanical properties of the metamaterial can be independent of each other. In this experiment, the strain exposed areas was replaced with a flexible polymer. It was demonstrated that with the use of dual extrusion printer the test specimen could be exposed to greater strains compared to an equivalent single material specimen. It was also possible to tune the mechanical properties of the auxetic metamaterial independently of each other.

Yet another study which bear resemblance to the study of Wang, Chang, Chen *et al.*[28] and is written by many of the same authors, are exploring the use of dual-material 3D-printers to recreate a metamaterial with a soft tissue behaviour capable of enduring large strains. In biomedical science, phantoms are used as stand-ins for human tissues to ensure that systems and methods for imaging the human body are operating correctly [29]. With a single material printer, soft tissue can be mimicked geometrically accurate, but only at low strain. To achieve this, Wang, Wu, Qian *et al.*[30] uses a combination of a stiff fiber filament and an elastic filament. With these two materials, the soft tissue can be tuned to match the properties of a specific patient. During the experiment, three different modifiable geometries are tested in order to approximate the strain-stiffening behaviour of soft tissue. Two of the designs reached a strain of 8% which is theoretically impossible to reach with a single material phantom. Although the result showed that the mechanical behaviour of soft tissue phantoms can be and tuned by changing the design parameters, some limitations were discovered. It was amongst other problems found that the interface between the different materials were not good.

Insufficient interface adhesion is a common occurrence when printing with two different materials. In order to maximise the mechanical performance of a multi-material part, the adhesion between different materials has to be as strong as possible. There are many parameters which influence the adhesion of two materials. In a article published by Lopes, Silva and Carneiro[31], the authors investigate how the affinity of the materials influence the boundary interface. The materials used in this article were polylactic acid (PLA), thermoplastic polyurethane (TPU) and polyethylene terephthalate (PET). The goal of the tests were to compare the interface strength between different materials to the interface strength of between equal materials. The test specimens were printed in three groups. First group of specimens were printed in a single material without a material boundary. This was done to benchmark the strength of the material. The second group was printed in a single material with material boundaries. Lastly the third group were printed with two different materials. This makes it possible to see how the boundary strength is effected when it is composed of different materials. The tests showed that a single material test specimen without borders performed the best. Next, the single material with material boundaries showed that the presence of a boundary had weakened the test sepcimen, making it perform between 22% and 45% worse than the single material test specimen. Lastly, the multi material test specimens performed the worse, where a PLA-PET interface only sustained $12.2MPa$ before fracture, compared to PLA-PLA interface which sustained $45.3MPa$ before fracture. The authors concluded the paper by pointing out the need to develop a proper interface geometry if the printed part is to have any performance increase.

One way the interface strength between two different materials can be enhanced, is by having a gradient transition from one material to the other. These gradual material transitions are called functionally graded materials (FGMs). Mirzaali, Herranz de la Nava, Gunashekar *et al.* [32] has published a paper where the mechanical properties of test specimens with varying degree of step-wise and continuous gradients are compared to each other. The purpose of the papers was to gain an understanding of how the mechanical properties of FGMs and how it fractures during different loading conditions. The gradual transition is printed by using a precise PolyJet printer. Tests were perfomed on a dogbone and single-edge notched uniaxial test speciment which were printed in a combination of hard and a soft material. The specimens were printed in a orientation where the material fraction would go from a complete hard phase to a complete soft phase, before returning to a complete hard phase. Different step-wise and continuous transition variables were used to decide the shape of the material transition. Test specimens with no transition were also made in order to compare to the gradual transition specimens. The test results showed that the ultimate tensile strength of the linear gradient transition specimen exceeded the control specimen by a factor of 1.75. However the increase in ultimate tensile strength came at the cost of toughness and elongation, which dropped 35% and 65% respectively.

4 Method

In this section of the thesis the production, post-processing, testing of the specimen and the numerical simulation procedure are explained in detail. Some of the problems that occurred during the project and each problem's solution are also discussed.

4.1 Preliminary Work

A specialization project were conducted during the fall of 2021 where the main object was to familiarise with bimaterial printing and calibrate the slicer and printer to produce bimaterial parts with high density and smooth surface quality.

4.2 Specimen Fabrication

4.2.1 Printer

The printer which has been used in this project is a CreatBot F430 3D-printer, pictured in Figure 2. It is a dual nozzle FDM-printer capable of extruding material at temperatures up to 420 °C. the print volume is enclosed in a heated chamber which can be heated to 70 °C. The print bed has a width of 400mm, depth of 300mm with a maximum print height of 300mm. The print bed is capable of reaching 140 °C and is leveled with 4 thumb screws, one in each corner. As well as manual bed-levelling, the printer has an automatic bed levelling function. [33]

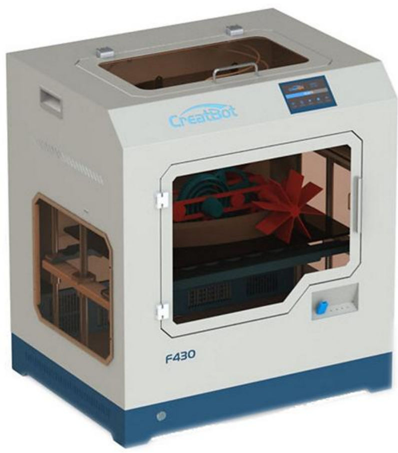

Figure 2: CreatBot f430 printer[33].

4.2.2 Software

For slicing of the prints, Ultimaker Cura was the software used in this project. Cura is a good choice of slicer as the complexity of the slicer can be adjusted to match the experience of the user. Cura is an open-source slicing engine which is had been developed through years by dedicated developers and community users. Ultimaker also has many years of experience with producing dual-extruder printers, which is why Cura has a wide range of custom settings, especially dedicated towards bimaterial printing.

4.2.3 Filament

All specimen printed during the project was printed with PLA filament from 3DNet[34] with a diameter of 1.75mm. PLA was the material of choice as it is a tried and tested material for 3D-printing which yields high quality prints with relatively low effort. PLA has a low thermal expansion coefficient[35] compared to other FDM filaments, which reduces warping during printing. PLA also has a high ultimate tensile strength[35]. Material and printing properties of 3DNet Pla can be seen in Table 1.

During the project, grey PLA filament was used for nozzle no. 1, while red PLA filament was used for nozzle no. 2. The colours was chosen because of their high contrast to each other. This makes it easier to examine residual filament on the interface fracture surfaces later in the project. The colours were also chosen because of their ease of availability.

3DNet PLA					
Diameter:	Print temp.:	Bed temp.:	Glass transition temp.:	UTS:	Density:
1.75mm	200 - 230 °C	0 - 70 °C	59 °C	65 MPa *	1.24 $\frac{g}{cm^3}$ *

Table 1: Material and printing properties of PLA[34][35].
(*value not specific to 3DNet PLA)

4.2.4 Multi-Material Printing in Cura

Cura only allows for one nozzle to be assigned for a model. In order to print a part with multiple nozzles, the model to be printed must be divided in CAD prior to loading it in Cura. The parts must then be aligned so that the interface of the part is aligned to each other, like shown in Figure 3. For the printing done in this project, the models were aligned with no overlap in the interface.

4.3 Fracture Specimen

SCB specimen were produced to determine the fracture toughness coefficients of the bimaterial interface in this project.

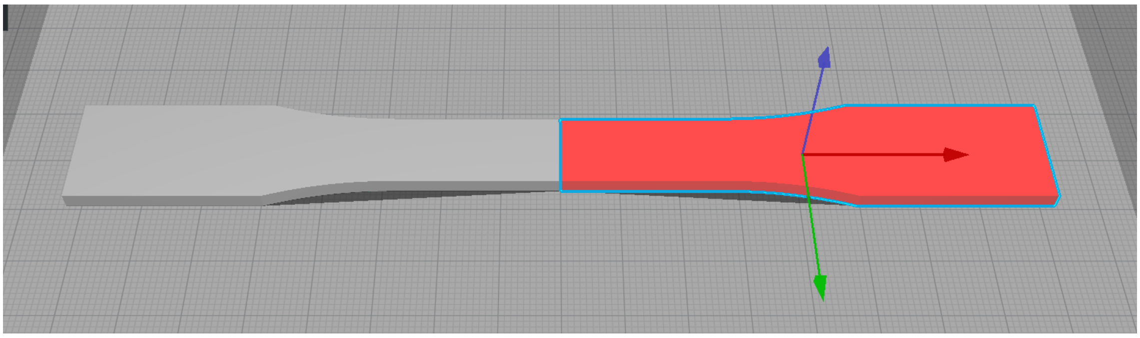

Figure 3: Two dogbone halves loaded in Cura and aligned for multi-material printing.

4.3.1 Printing Orientation

The SCB specimen were printed in two different orientations. Laying and standing, as shown in Figure 4. Printing the specimen in these two orientations creates different bimaterial interface conditions. The laying disc will have a interface in the vertical direction where the material is printed next to each other, melting the two different materials together. For the standing one the interface will be in the horizontal direction where one material is printed on top of the other. This was done to see how the orientation of the bimaterial interface influences the strength of the print.

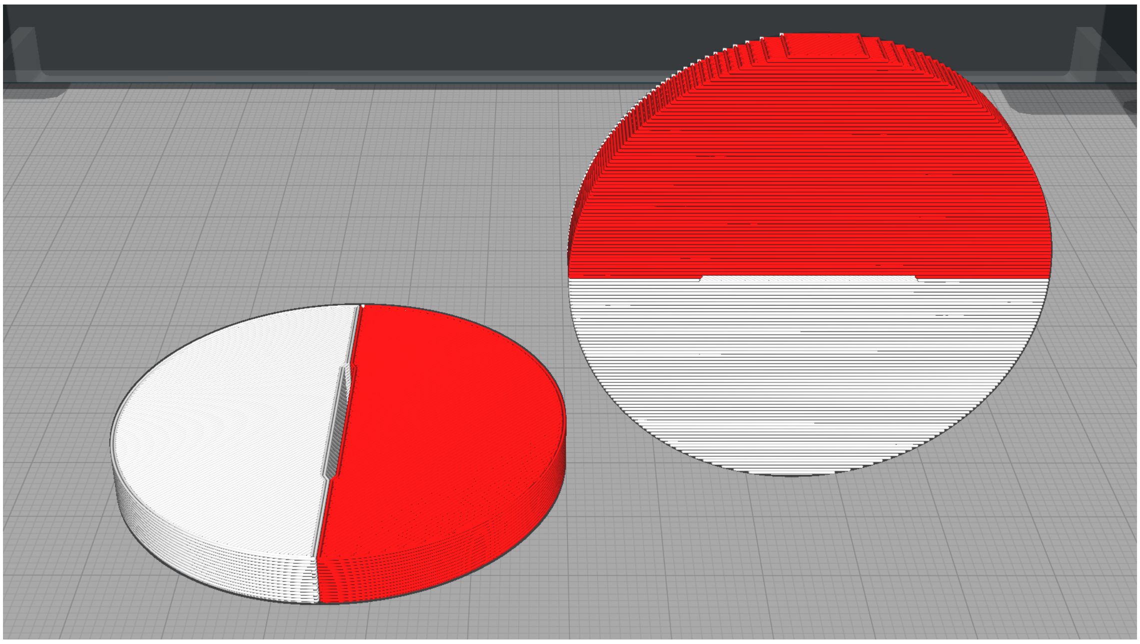

Figure 4: One laying and one standing SCB disc in Cura.

These two orientations will be identified with ”laying” and ”standing” through out the project, where the ”laying” specimen have a vertical interface printed next to each other and the ”standing” specimen will have a horizontal interface printed on top of each other.

4.3.2 SCB-specimen Disc

The SCB specimen were printed as whole discs, which were later to be cut at different angles. This meant that one 3D model could be used to make specimen for all fracture conditions which were tested during the project.

The SCB-specimen used in this project were 50mm in diameter and 6mm thick with a 1mm wide and 11.5mm long notch (see Figure 5). The notch width was set to 1mm to make it possible to remove the support printed in the notch when the specimen were printed in the standing orientation. The notch was given a 11.5mm length to make space for a 1mm crack at the tip of the notch, making the total length from the crack tip to the centre of the specimen, 12.5mm.

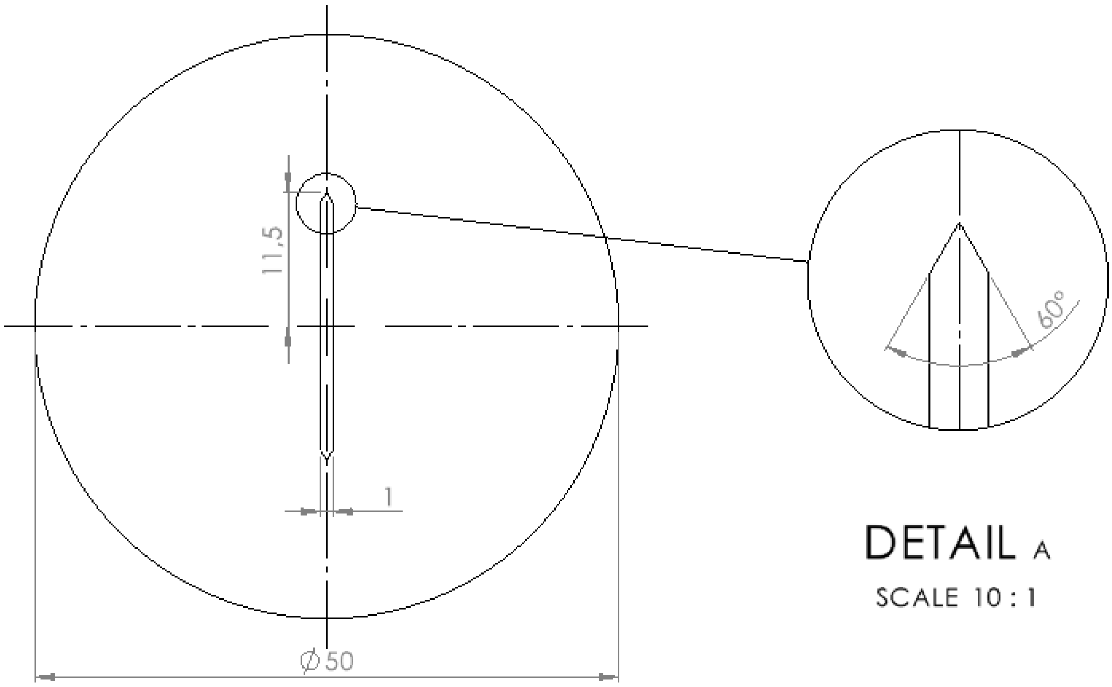

Figure 5: Dimentions of SCB-specimen disc.

The notch tip was given a 60° point to minimise printing defects due to steep overhangs. This angle is chosen so that less than half of the width of the outer wall is printed in mid air. This can be seen illustrated in Figure 6. Here we can see that the overhang angle should be no more than 26.5° to ensure that at least half of the line is printed on top of the previous layer.

4.3.3 Bimaterial SCB-specimen

The bimaterial SCB-specimen discs are cut, the two resulting SCB-specimen will have an unequal ratio of grey and red material compared to each other. This is shown in Figure 7. Two sets of bimaterial SCB-specimen were therefore produced to investigate if this difference affects the test results. The bimaterial specimen in Table 2 and Table 3 are identified with either ”Grey half lower” or ”Red half lower” to describe which colour

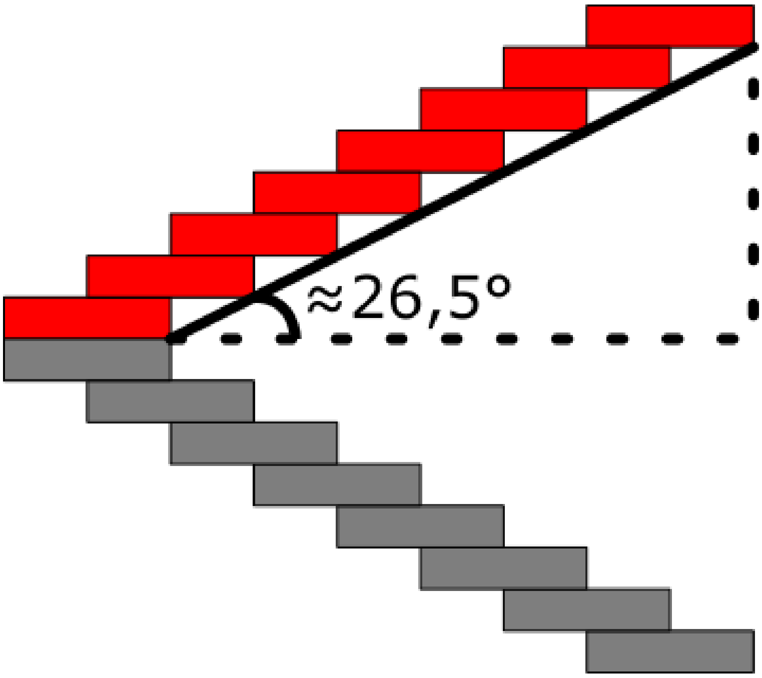

Figure 6: Minimum angle of overhang while printing notch tip.

the smaller portion of the specimen has. An example of this difference can be seen in Figure 7.

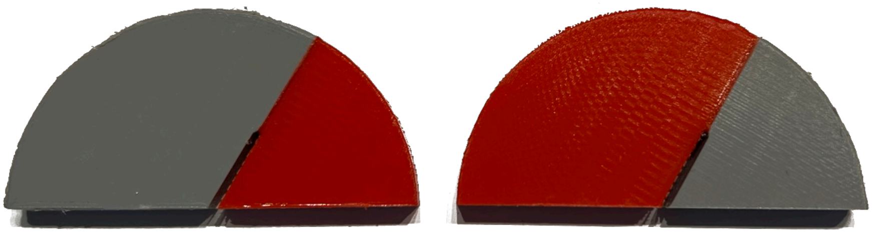

Figure 7: Difference between a ”red half lower” (left) and a ”grey half lower” (right) SCB-specimen.

4.3.4 Overview of produced SCB specimen

A complete overview of the SCB-specimen produced an tested in this project can be seen in Table 3 and Table 2, where the specimen highlighted in green text were tested with digital image correlation (DIC) to capture surface strain during testing. A complete overview of the fracture specimen with production and testing dates can be seen in Appendix C.

Table 2: List of laying SCB-specimen. Specimen highlighted in green were tested with DIC.

SCB number:	Date printed:	Location:	Angle[°]:	Type	Material	Bimaterial orientation:
1	14.2.2022	1	0	Bimaterial	PLA/PLA	
2	14.2.2022	1	0	Bimaterial	PLA/PLA	
3	14.2.2022	2	0	Bimaterial	PLA/PLA	
4	14.2.2022	2	0	Bimaterial	PLA/PLA	
5	14.2.2022	3	15	Bimaterial	PLA/PLA	Red half lower
6	15.2.2022	1	15	Bimaterial	PLA/PLA	Red half lower
7	18.3.2022	3	15	Bimaterial	PLA/PLA	Red half lower
8	16.2.2022	1	15	Bimaterial	PLA/PLA	Red half lower
9	14.2.2022	3	15	Bimaterial	PLA/PLA	Grey half lower
10	15.2.2022	1	15	Bimaterial	PLA/PLA	Grey half lower
11	18.3.2022	2	15	Bimaterial	PLA/PLA	Grey half lower
12	6.5.2022	2	15	Bimaterial	PLA/PLA	Grey half lower
13	16.2.2022	2	30	Bimaterial	PLA/PLA	Red half lower
14	17.2.2022	1	30	Bimaterial	PLA/PLA	Red half lower
15	17.2.2022	2	30	Bimaterial	PLA/PLA	Red half lower
16	17.2.2022	3	30	Bimaterial	PLA/PLA	Red half lower
17	16.2.2022	2	30	Bimaterial	PLA/PLA	Grey half lower
18	17.2.2022	1	30	Bimaterial	PLA/PLA	Grey half lower
19	17.2.2022	2	30	Bimaterial	PLA/PLA	Grey half lower
20	17.2.2022	3	30	Bimaterial	PLA/PLA	Grey half lower
21	6.5.2022	3	40	Bimaterial	PLA/PLA	Red half lower
22	18.2.2022	1	40	Bimaterial	PLA/PLA	Red half lower
23	18.3.2022	2	40	Bimaterial	PLA/PLA	Red half lower
24	6.5.2022	4	40	Bimaterial	PLA/PLA	Red half lower
25	17.2.2022	4	40	Bimaterial	PLA/PLA	Grey half lower
26	18.2.2022	1	40	Bimaterial	PLA/PLA	Grey half lower
27	6.5.2022	3	40	Bimaterial	PLA/PLA	Grey half lower
28	6.5.2022	4	40	Bimaterial	PLA/PLA	Grey half lower
29	21.2.2022	1	0	Single-material	GREY PLA	
30	21.2.2022	1	0	Single-material	GREY PLA	
31	21.2.2022	2	0	Single-material	GREY PLA	
32	21.2.2022	2	0	Single-material	GREY PLA	
33	21.2.2022	3	15	Single-material	GREY PLA	
34	21.2.2022	3	15	Single-material	GREY PLA	
35	21.2.2022	4	15	Single-material	GREY PLA	
36	21.2.2022	4	15	Single-material	GREY PLA	
37	22.2.2022	1	30	Single-material	GREY PLA	
38	22.2.2022	1	30	Single-material	GREY PLA	
39	22.2.2022	2	30	Single-material	GREY PLA	
40	22.2.2022	2	30	Single-material	GREY PLA	
41	22.2.2022	3	40	Single-material	GREY PLA	
42	20.5.2022	1	40	Single-material	GREY PLA	
43	20.5.2022	1	40	Single-material	GREY PLA	
44	22.2.2022	4	40	Single-material	GREY PLA	
45	28.2.2022	1	0	Single-material	RED PLA	
46	28.2.2022	1	0	Single-material	RED PLA	
47	23.2.2022	2	0	Single-material	RED PLA	
48	23.2.2022	2	0	Single-material	RED PLA	
49	23.2.2022	3	15	Single-material	RED PLA	
50	23.2.2022	3	15	Single-material	RED PLA	
51	25.4.2022	1	15	Single-material	RED PLA	
52	25.4.2022	1	15	Single-material	RED PLA	
53	20.5.2022	1	30	Single-material	RED PLA	
54	25.2.2022	1	30	Single-material	RED PLA	
55	25.2.2022	2	30	Single-material	RED PLA	
56	25.2.2022	2	30	Single-material	RED PLA	
57	25.2.2022	3	40	Single-material	RED PLA	
58	20.5.2022	2	40	Single-material	RED PLA	
59	20.5.2022	2	40	Single-material	RED PLA	
60	25.2.2022	4	40	Single-material	RED PLA	

Table 3: List of standing SCB-specimen. Specimen highlighted in green were tested with DIC.

SCB number:	Date printed:	Location:	Angle[°]:	Type	Material	Bimaterial orientation:
61	31.3.2022	1	0	Bimaterial	PLA/PLA	
62	31.3.2022	1	0	Bimaterial	PLA/PLA	
63	20.4.2022	1	0	Bimaterial	PLA/PLA	
64	31.3.2022	2	0	Bimaterial	PLA/PLA	
65	20.4.2022	2	15	Bimaterial	PLA/PLA	Red half lower
66	31.3.2022	4	15	Bimaterial	PLA/PLA	Red half lower
67	1.4.2022	1	15	Bimaterial	PLA/PLA	Red half lower
68	1.4.2022	2	15	Bimaterial	PLA/PLA	Red half lower
69	20.4.2022	2	15	Bimaterial	PLA/PLA	Grey half lower
70	31.3.2022	4	15	Bimaterial	PLA/PLA	Grey half lower
71	1.4.2022	1	15	Bimaterial	PLA/PLA	Grey half lower
72	1.4.2022	2	15	Bimaterial	PLA/PLA	Grey half lower
73	6.5.2022	1	30	Bimaterial	PLA/PLA	Red half lower
74	2.4.2022	1	30	Bimaterial	PLA/PLA	Red half lower
75	9.5.2022	1	30	Bimaterial	PLA/PLA	Red half lower
76	3.4.2022	1	30	Bimaterial	PLA/PLA	Red half lower
77	1.4.2022	4	30	Bimaterial	PLA/PLA	Grey half lower
78	2.4.2022	1	30	Bimaterial	PLA/PLA	Grey half lower
79	2.4.2022	2	30	Bimaterial	PLA/PLA	Grey half lower
80	3.4.2022	1	30	Bimaterial	PLA/PLA	Grey half lower
81	3.4.2022	2	40	Bimaterial	PLA/PLA	Red half lower
82	20.4.2022	3	40	Bimaterial	PLA/PLA	Red half lower
83	6.5.2022	2	40	Bimaterial	PLA/PLA	Red half lower
84	6.5.2022	3	40	Bimaterial	PLA/PLA	Red half lower
85	3.4.2022	2	40	Bimaterial	PLA/PLA	Grey half lower
86	6.5.2022	2	40	Bimaterial	PLA/PLA	Grey half lower
87	20.4.2022	3	40	Bimaterial	PLA/PLA	Grey half lower
88	6.5.2022	3	40	Bimaterial	PLA/PLA	Grey half lower
89	21.4.2022	1	0	Single-material	GREY PLA	
90	21.4.2022	1	0	Single-material	GREY PLA	
91	21.4.2022	2	0	Single-material	GREY PLA	
92	21.4.2022	2	0	Single-material	GREY PLA	
93	21.4.2022	3	15	Single-material	GREY PLA	
94	21.4.2022	3	15	Single-material	GREY PLA	
95	21.4.2022	4	15	Single-material	GREY PLA	
96	21.4.2022	4	15	Single-material	GREY PLA	
97	19.5.2022	1	30	Single-material	GREY PLA	
98	26.4.2022	1	30	Single-material	GREY PLA	
99	26.4.2022	2	30	Single-material	GREY PLA	
100	26.4.2022	2	30	Single-material	GREY PLA	
101	26.4.2022	3	40	Single-material	GREY PLA	
102	26.4.2022	3	40	Single-material	GREY PLA	
103	26.4.2022	4	40	Single-material	GREY PLA	
104	26.4.2022	4	40	Single-material	GREY PLA	
105	11.5.2022	1	0	Single-material	RED PLA	
106	11.5.2022	1	0	Single-material	RED PLA	
107	11.5.2022	2	0	Single-material	RED PLA	
108	11.5.2022	2	0	Single-material	RED PLA	
109	11.5.2022	3	15	Single-material	RED PLA	
110	11.5.2022	3	15	Single-material	RED PLA	
111	11.5.2022	4	15	Single-material	RED PLA	
112	11.5.2022	4	15	Single-material	RED PLA	
113	12.5.2022	1	30	Single-material	RED PLA	
114	12.5.2022	1	30	Single-material	RED PLA	
115	12.5.2022	2	30	Single-material	RED PLA	
116	12.5.2022	2	30	Single-material	RED PLA	
117	12.5.2022	1	40	Single-material	RED PLA	
118	12.5.2022	1	40	Single-material	RED PLA	
119	12.5.2022	2	40	Single-material	RED PLA	
120	12.5.2022	2	40	Single-material	RED PLA	

4.4 Tensile Specimen

The tensile test specimen manufactured and tested in this thesis were modelled after ASTM D638 Type 1 tensile test specimen, as can be seen in Figure 8. The tensile specimen were printed to obtain the properties of the material. The material properties was captured using DIC, and is explained further is Section 4.9.

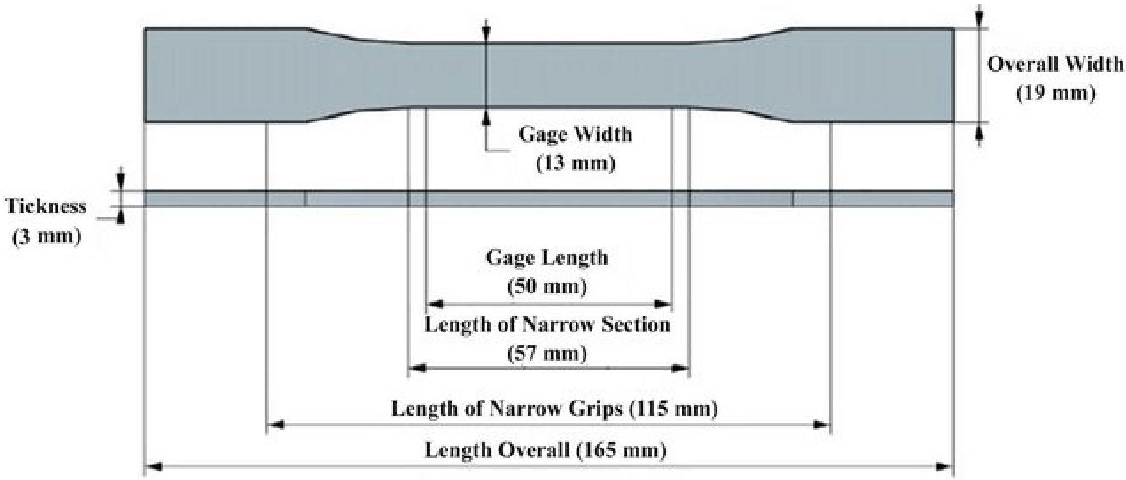

Figure 8: Dimensions of ASTM D638 Type 1 tensile test specimen[36].

Single material red, single material gray and bimaterial specimen were printed in laying and standing orientation. Each specimen was printed 3 times to get a mean value for the material properties. To minimize the defects caused by printing slim tall objects, the height of the standing tensile specimen were reduced by 2/3, making them 55mm high.

4.5 Printing

The SCB specimen were printed 4 at a time with a sequential printing order, meaning the printer will print each specimen fully before starting a new specimen. This is repeated until the 4 specimen are printed, and the specimen needs to be removed from the print-bed and the printer must be restarted. It was initially planned to print more specimen per print, however due to problems with the printer´s automatic bed levelling, this was not possible.

Before the printing of the SCB-specimen began, the printer was calibrated to where the printer could produce parts without any gaps or porosity in the infill. After the process parameters had been set in the slicer and the production of the SCB-specimen had begun, the settings were not to be changed for the rest of the project. A complete overview of the settings used in Cura can be seen in Appendix A and Appendix B.

All specimen were printed with a layer of Dimafix [37] applied to the print bed. Dimafix is a heat activated fixative made for 3D printing. This has ensured good adhesion throughout the project without any warping during the specimen production.

4.5.1 Automatic Bed Levelling

As mentioned in Section 4.2.1, the printer is equipped with automatic bed levelling, however this feature has turned out to be unusable for this project, as it is to unreliable. To ensure a good and consistent specimen quality, it is important that the first layer is properly printed. During the beginning of the project, there was inconsistencies in the distance between the nozzle and print-bed. A ”Bed Level Calibration Test” (Figure 9a) from the ”Calibration Shapes” plugin for Cura[38] was printed to visualise the issue. The results from the bed levelling test can be seen in Figure 9a. In Figure 9c the nozzle is too far away from the print bed, while in Figure 9c the nozzle is too close to the print bed. These images were taken from the same print. In attempt to rectify this issue the bed was manually and automatically levelled, the probe sensor for the automatic levelling was changed and settings adjusting the levelling fade height was adjusted. However these actions lead to little to none improvement of the first layer. The automatic bed levelling was therefore disabled, and the bed was manually levelled instead.

4.5.2 Laying Specimen

The laying SCB-specimen were printed with the notch aligned along the Y-axis of the print bed with the grey PLA printed on the left half and the red PLA on the right half, as shown in Figure 10.

After the first batch of laying SCB-specimen had been printed, a difference in the geometry of the notch was noticed. The notch appeared to be oval rather than straight, and the degree of ovalness was varying between the specimen, as shown in Figure 11. Due to the print bed temperature being set to 70°C, which is above the 58°C [34] glass transition temperature of the 3DNet PLA, the high heat over time had caused the specimen to deform. Because of the sequential print order the specimen which was printed first had been on the heated bed for 6 hours longer than the last specimen to be printed, causing the deformation of the notch of the SCB-specimen to be gradually decreasing according to its position on the print bed. To solve this issue the bed temperature was lowered to 50°C and the specimen were re-printed.

4.5.3 Standing Specimen

The standing specimen were printed with the notch aligned along the X-axis of the print bed with the grey PLA printed at the bottom half and red PLA at the top half of the specimen, as can be seen in Figure 14. To print the specimen in the standing orientation, there is need for support structure to be generated.

The support was generated in Cura, with the ”Lines” support pattern and a 1.3mm innfill distance for any overhang with a steeper incline than 15°. The ”Support Z distance” was set to 0.2mm to make the process of removing the support from the notch easier. A complete overview of the slicer settings can be seen in Appendix A

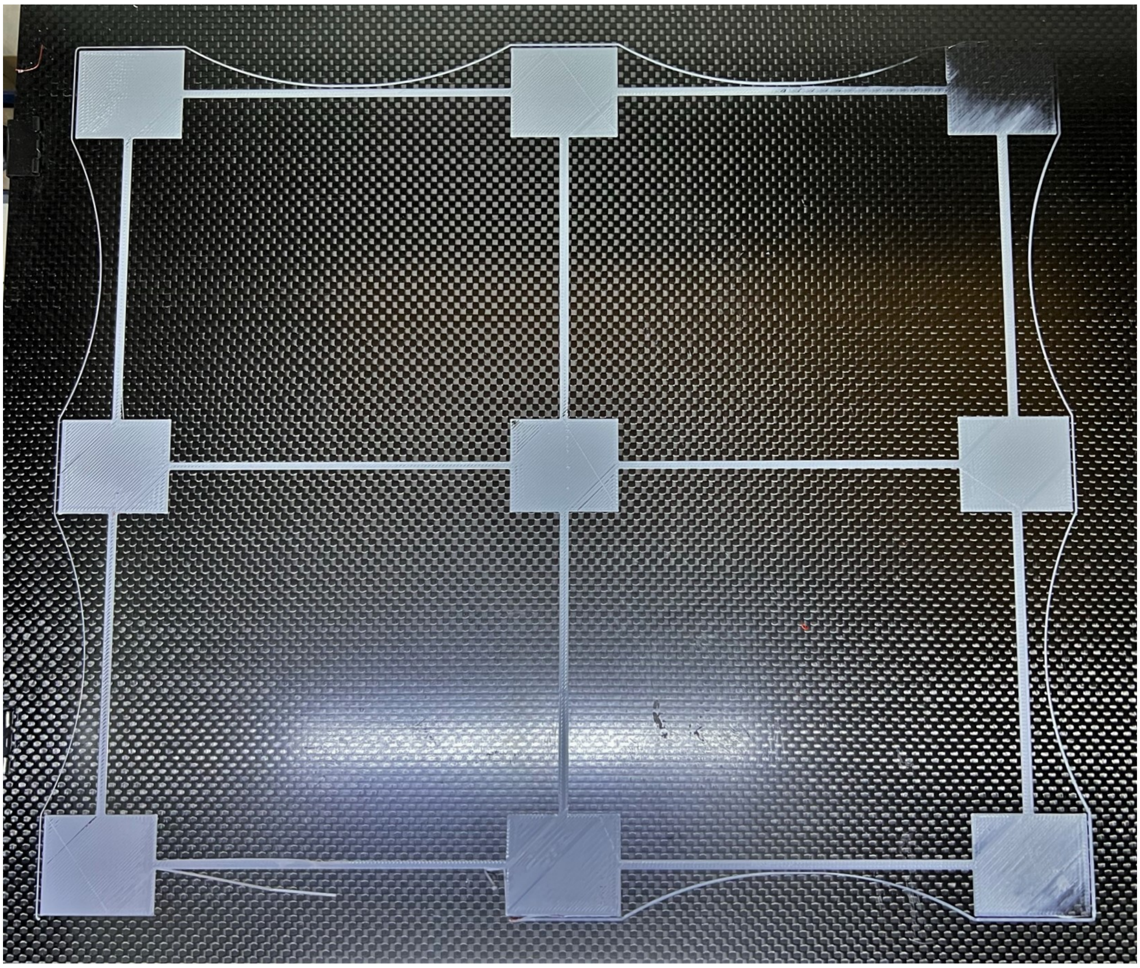

(a) Overview of ”Bed Level Calibration Test”.

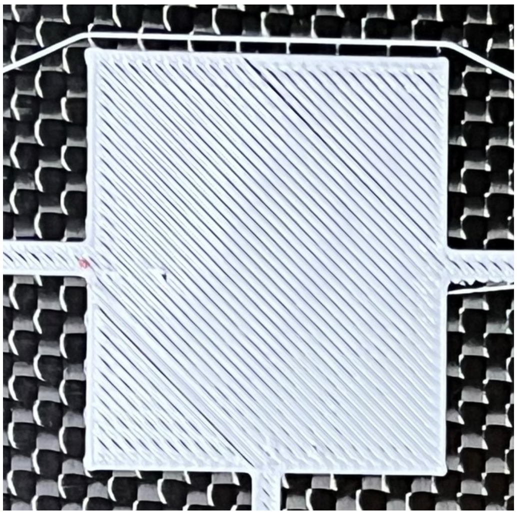

(b) Nozzle printing too far off the print bed.

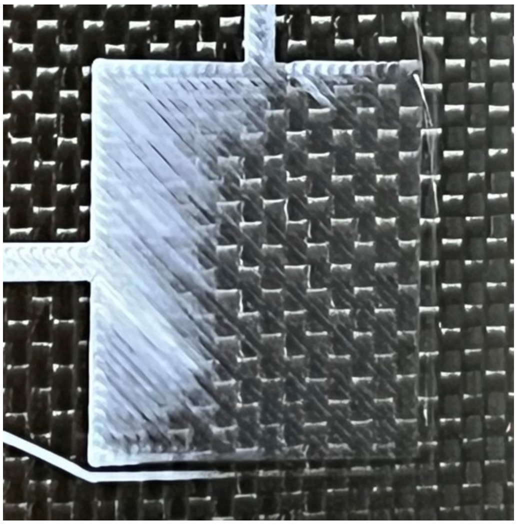

(c) Nozzle printing too close to the print bed.

Figure 9: Result of inconsistent automatic bed levelling.

and Appendix B. In Cura, the support is generated relative to the build plate and not the geometry of the part being printed. This means that the exact arrangement of the support structure can be different for two equal parts, printed at different locations. To

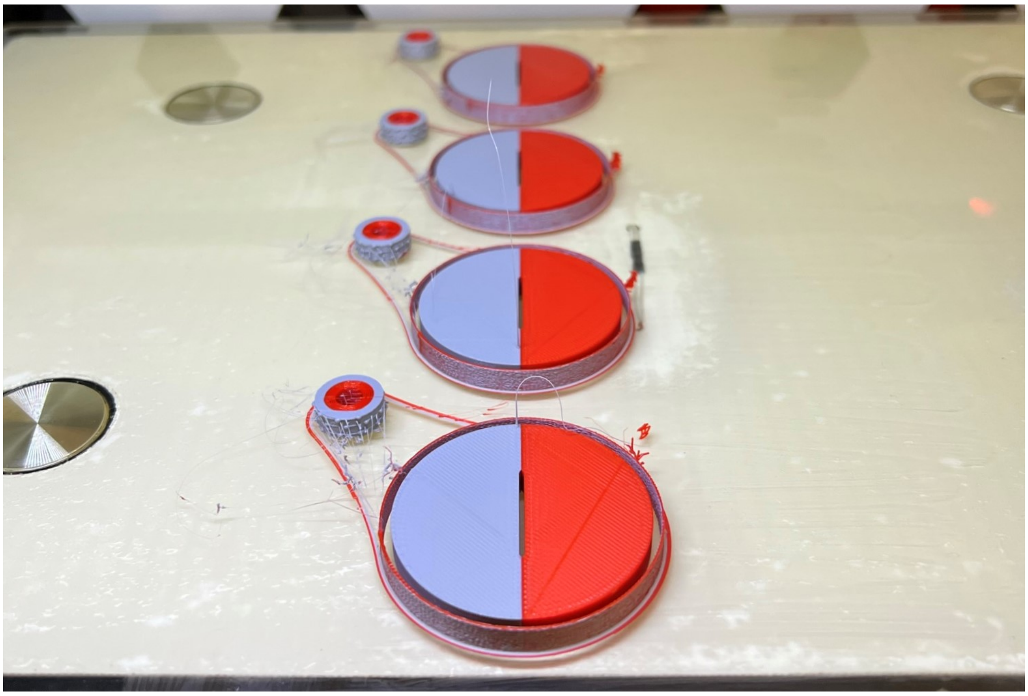

Figure 10: 4 Laying SCB-specimen in printer.

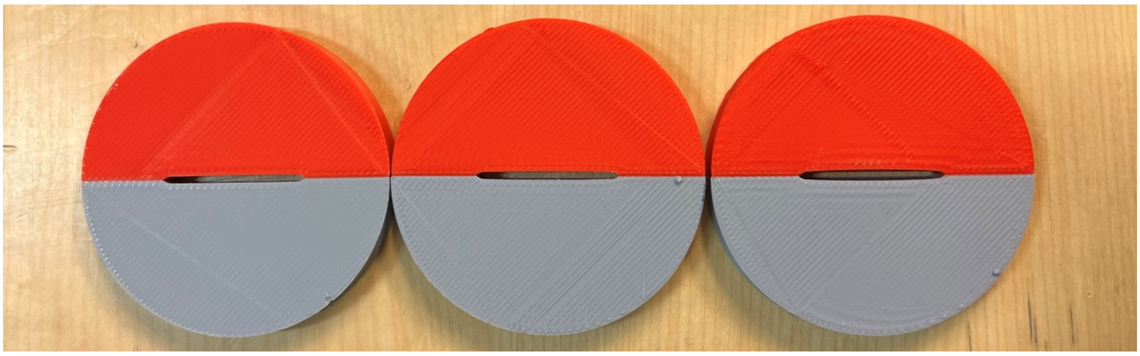

Figure 11: Oval notch in laying SCB-specimen.

make sure the support were generated equally for each specimen, the position of the specimen were precisely set so that the support structure would be the same for each specimen. in Figure 12 it is shown how the support changed when the specimen was moved 0.7mm in Y-direction. In Figure 12a the edge of the specimen is not supported which results in poor quality, while Figure 12b has proper support from edge to edge. Due to this, the position of each specimen was adjusted so that every specimen had the same support structure when printing.

4.5.4 Porosity in Standing Specimen

During sharpening of the crack tip of the standing bimaterial SCB-specimen, there was discovered severe defects in the bimaterial interface. Each specimen would split open while sharpening the crack, exposing porosity as seen in Figure 13. This porosity would only appear in the red material, which was the material printed on top of the

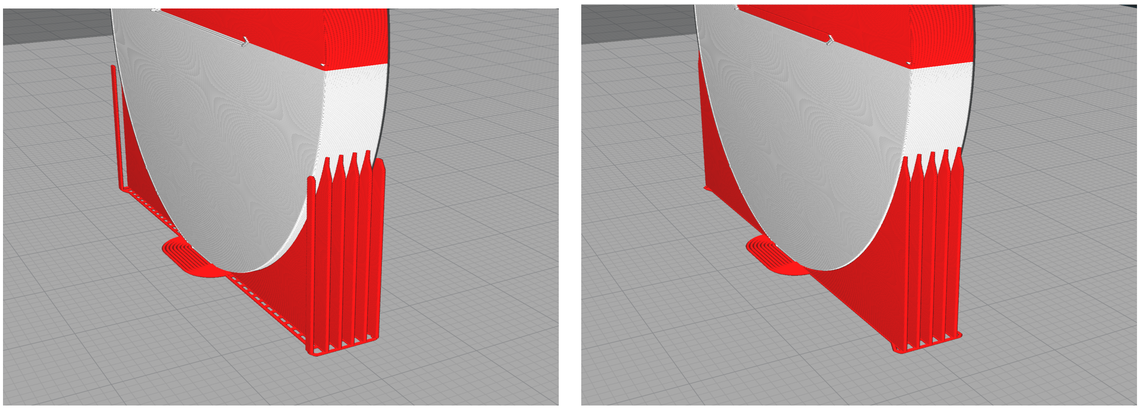

(a) Standing SCB-specimen with poor support. (b) Standing SCB-specimen with good support.

Figure 12: Adjustment of standing SCB-specimen support structure.

grey half of the SCB-specimen. This porosity was a result of the way Cura generates priming towers, which caused the red nozzle to start printing with an under-primed nozzle. Cura only primes a nozzle if the nozzle is used in a layer. When printing the standing SCB-specimen the red nozzle would stay active for 2 hours without priming, due to the grey nozzle only being used. This causes the red nozzle to ooze a large amount of material. When it is time for the red nozzle to start printing, the amount of material extruded in the prime tower was lower than the material which had oozed during printing of the first half. This means that the first layers in the red half of the SCB-specimen would be under-extruded, causing the porosity.

Figure 13: Porosity in standing bimaterial interface.

To work around this limitation in Cura, an extra tower was placed next to the SCB-specimen which had the opposite material of the SCB-specimen at each layer. In Figure 14 the tower to the right is placed with cylinders from the "Calibrations shapes" plugin [38] for Cura. This forces Cura to prime both nozzles for each layer, which ensures that the red nozzle will perform as intended when printing the red half of the SCB-specimen.

4.5.5 Underextrusion in Infill

During the troubleshooting process in Section 4.5.4, there was noticed some temporary under-extrusion during the first second of the printing of the infill. The under-

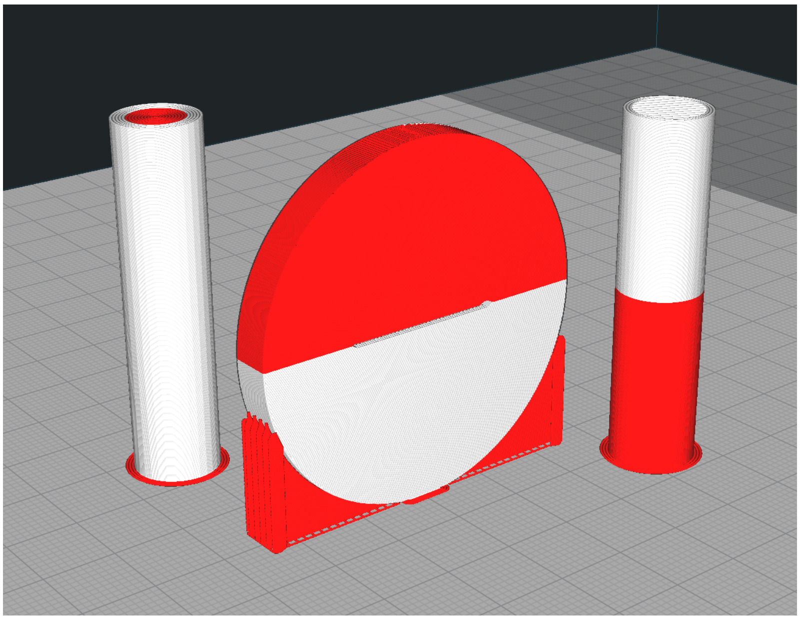

Figure 14: Forcing prime tower throughout the entire print.

extrusion would gradually improve before returning to printing solid infill without voids. An example of this is shown in Figure 15. Here, the green dot is the start of the infill path, the solid line is an extrusion path and the dotted line is a travel path. Here the grey filament from the previous layers can be seen between the first couple of red infill passes. The amount of grey visible between the red infill is gradually decreasing as the infill is being printed.

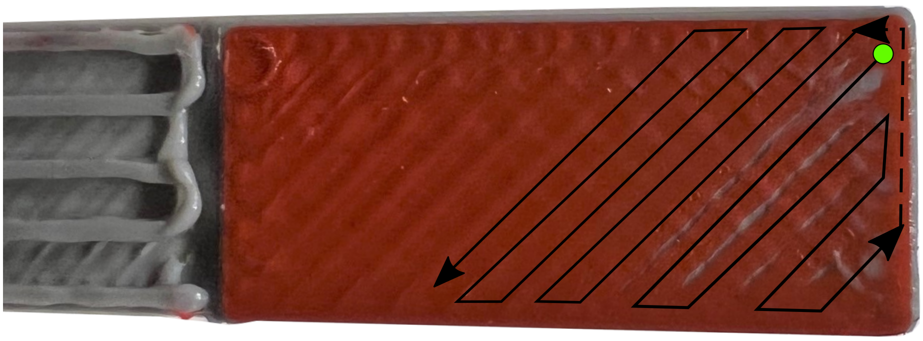

Figure 15: Under-extrusion at the beginning of an extrusion-path.

Some changes to the motion settings during infill-printing were done which lead to some improvements to the infill, however there was still some under-extrusion present. The under-extrusion can be symptoms of the printer not being able to build the nozzle pressure quickly enough to extrude the correct amount of material. The changes which were made to the motion settings can be seen in Table 4.

Table 4: Changes made to the infill motion settings.

	Infill Acceleration [mm/s^2]:	Infill Jerk [mm/s^3]:
Standard setting:	3000	20
New setting:	1500	10

4.6 Laser Cutting

Once the SCB-discs had been printed, they needed to be cut before the fracture tests could be performed. A 120W Epilog Fusion M2 CO_2 laser cutter was used to cut the SCB-discs and create the SCB-specimen. To determine the best cutting parameters, discarded SCB-specimen were used to do test-cuts and evaluate the quality of the cut. A variation of single- and multiple-pass cuts were tested with varying laser power, cutting speed, frequency and laser focal points were made, without achieving a cut with acceptable quality. It was learned that PLA is not a material that is suitable for laser cutting, as the heat from the laser would melt the PLA, rather than burn away the material. This resulted in an uneven cut which was slightly slanted. In Figure 16 a SCB-specimen is placed with the cut down on a flat surface next to a machining parallel, which is a highly precise machining tool. This is not acceptable as it can cause out of plane fracture modes if tested in this condition. The solution used to correct this issue is described in Section 4.7

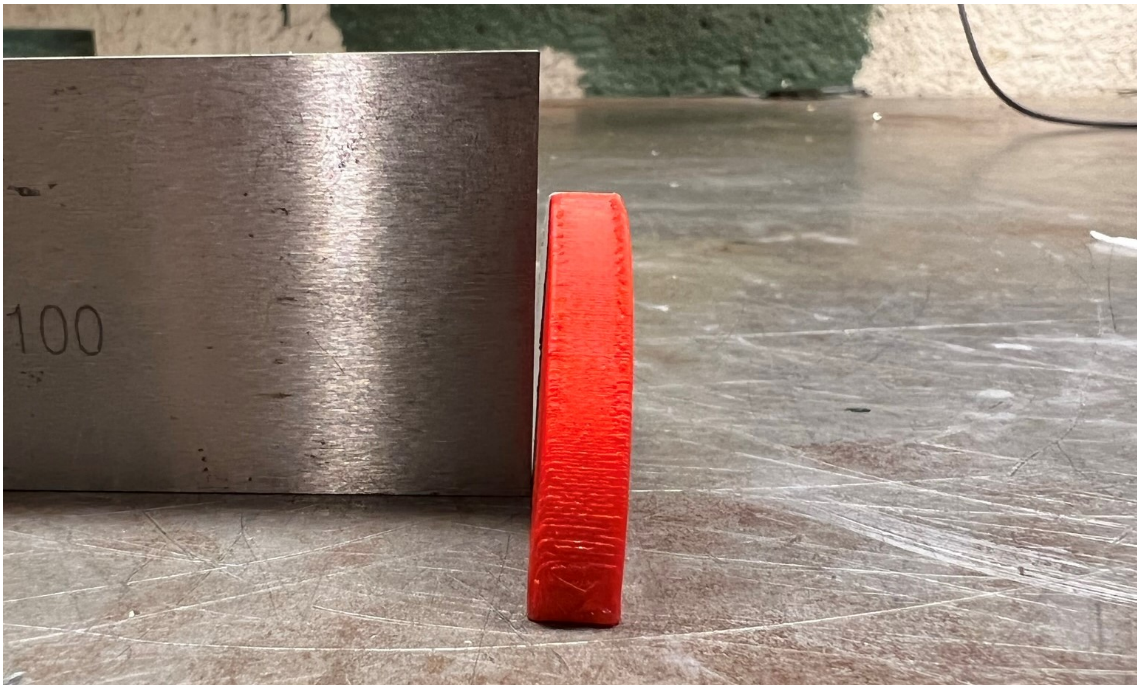

Figure 16: SCB-specimen with slanted cut after laser-cutting.

After a method to square up an smooth out the cut was developed, the cutting of the SCB-specimen could proceed. The final process cutting settings were determined after getting recommendations from the norwegian supplier of Epilog laser cutters. The final laser cutter settings can be found in Table 5.

To ensure a precise and repeatable cut at different notch angles, a tool to

Table 5: Laser cutting settings used for cutting SCB-specimen.

	Power	Frequency	Speed
6mm Thick SCB	95	50	10

properly align the specimen in the laser cutter had to be made. The tool had to be easily positioned at the correct position in the printer and have marks for 0°, 15°, 30° and 40° angles to properly align the notch. The tool also needs a reference point in order to zero the origin of the laser, to get the cut at the correct position. A render of the result can be seen in Figure 17.

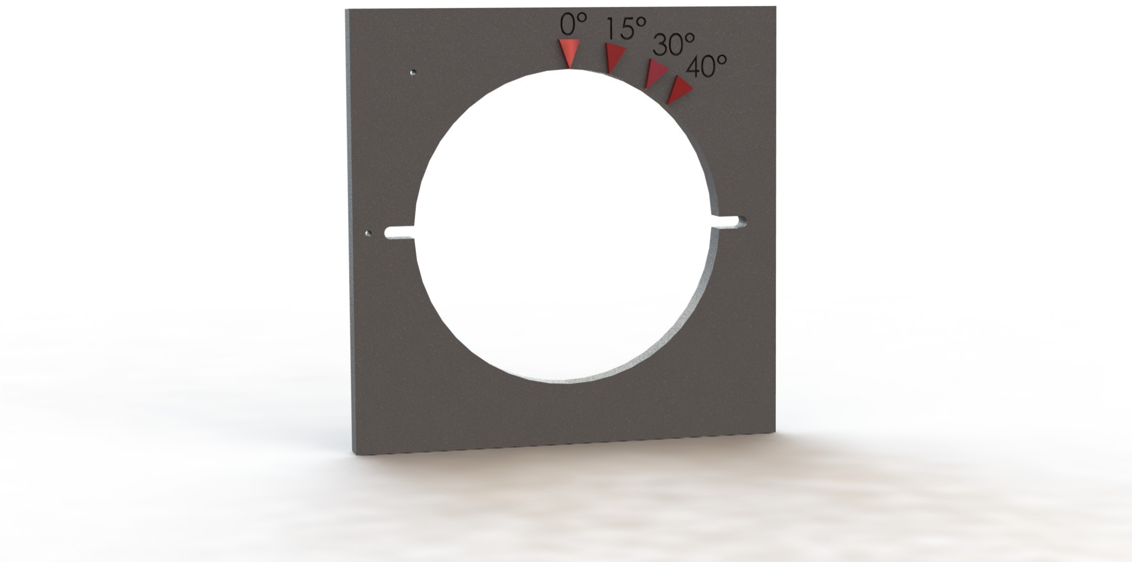

Figure 17: SCB-disc cutting fixture.

To use this alignment fixture, the entire fixture is placed in one of the corners of the cutting area of the cutter. This way the fixture can be placed and removed without needing to re-zero the print origin. The origin of the printer is then aligned at one of the alignment-holes at the face of the fixture. The hole at the left of the angle embossment at the front face of the fixture is placed perpendicular to the top and side of the SCB-disc hole, making it easy to program the laser cutter to do the correct cut, once the origin zero has been set. The alignment hole to the left of the SCB-disc slot can also be used. In Figure 18 the fixture can be seen in use with a SCB-disc aligned at 40°. In this picture the laser is zeroed at the top left alignment hole and is placed against the top and right table edge.

4.7 Facing of Cut

Due to the poor quality of the cut left by the laser cutter, a method for smoothing out and making the cut square to its neighbouring edges had to be developed. For this, a mill with a facing tool was used to machine off a small layer of material, leaving a

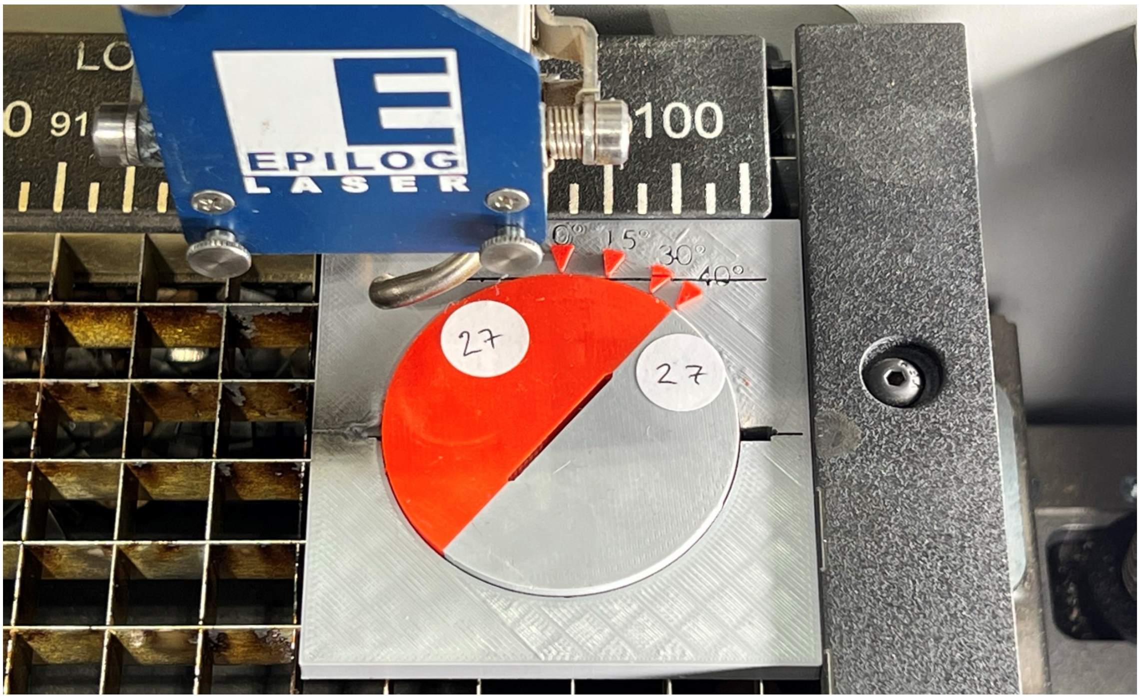

Figure 18: SCB-disc and alignment fixture in laser cutter.

completely flat and square finish. A facing tool is used for a milling operation called face milling, and is the operation of cutting surfaces that are perpendicular to the cutter axis, and is demonstrated in Figure 19.[39]

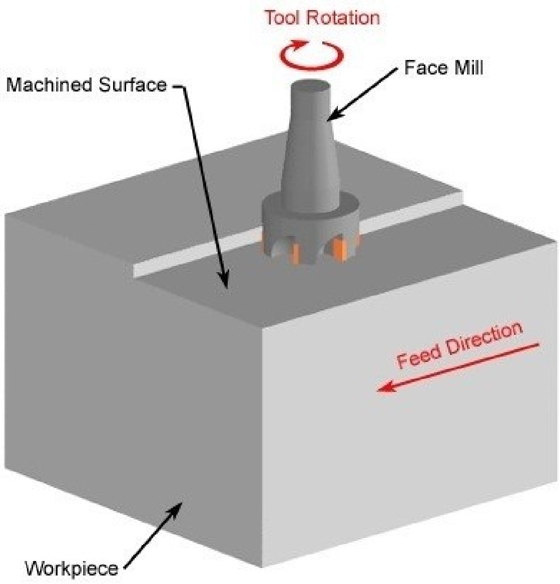

Figure 19: Face milling. [40]

The mill used for this opearion was a TOS FA3A-U with a SECO R220.69-0080-16 facing tool. The face mill was equipped with six SECO APMX160408TR-M14 F40M carbide inserts. The carbide inserts has sharp edges, resulting in a clean cut. The mill is equipped with a digital readout (DRO) system, which allows for digital measurements on a manual mill. The DRO has a resolution of 5 microns, which makes it possible to cut very thin layers of the specimen. Despite its old age, the machine is well maintained and calibrated to ensure an accurate result. The mill used for the face milling is displayed in Figure 20.

Figure 20: TOS FA3A-U mill.

When machining with a mill, it is important that the workpiece is properly secured to the table of the mill. The mill is equipped with a hydraulic precision vice, where workpieces can be tightly clamped before machining. however, due to the vice is equipped with a hydraulic pressure booster, directly fastening the SCB-specimen would introduce the risk of overtightening the vice, which could cause damage or deteriorate the structural integrity of the specimen. Directly mounting the specimen in the vice would also make it difficult to align the edge of the specimen parallel to the table of the mill. It is important to keep the specimen parallel to the table to not change the angle of the notch. Due to these conditions, a custom fixture needed to be created in order to properly fix the specimen to the mill.

During development it was therefore desirable to make a fixture which prevented too much force to be applied the SCB-specimen and made it easy to align the laser-cut surface of the specimen parallel to the table of the mill. The final fixture is displayed in Figure 21.

The fixture has a half circle cutout with the same geometry as the SCB-specimen, allowing the specimen to be slid down in to the pocket. There is a cut along the pocket to make the fixture-sides flexible. This allows the clamping force from the vice to be transferred to the specimen, which tightly secures it. The fixture is printed in PLA, with a infill-density of 20%. This makes the fixture quick and easy

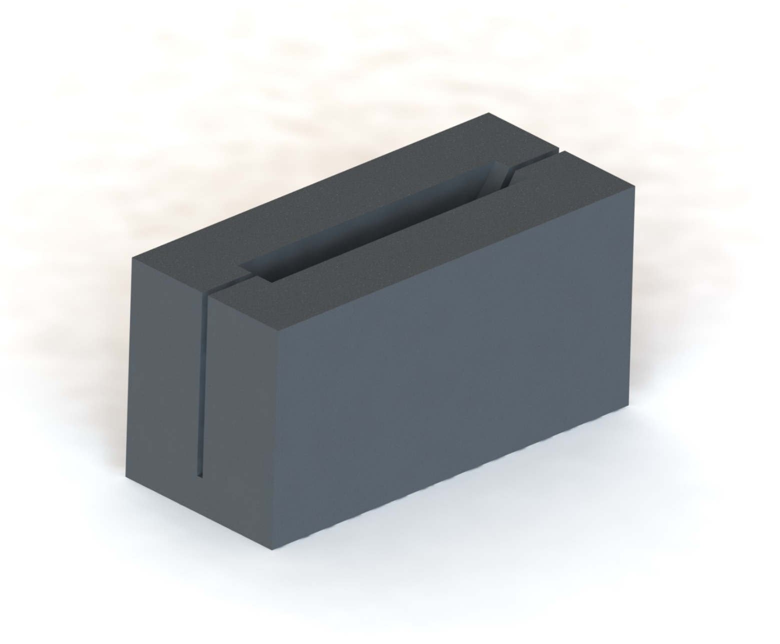

Figure 21: SCB-specimen fixture.

to make. The low infill-density allows the fixture to crumble, if the vice were to be overtightened. This protects the specimen from any damage caused by excessive force.

To make the laser-cut surface parallel to the mill-table, which will make the face cut parallel to the surface of the specimen, the specimen was loaded in the fixture with a high precision vice. These vices are precisely assembled which means the jaws of the vice are perfectly parallel. Loading the specimen with the vice will also ensure that the specimen is properly seated in the fixture. A illustration of this process can be seen in Figure 22.

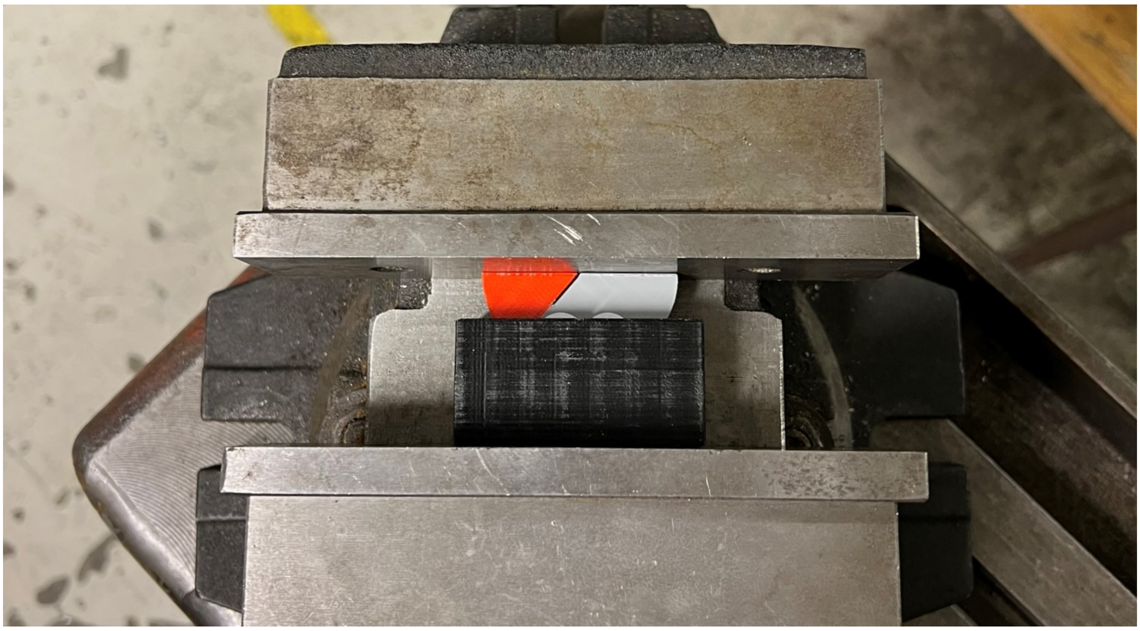

Figure 22: SCB-specimen loaded in fixture with vice.

When the SCB-specimen is loaded in the fixture, the loaded fixture is placed on parallel supports in the mill-mounted vice, ready to be machined. This can be seen in Figure 23

Figure 23: SCB-specimen mounted in mill and machined.

4.8 Crack Sharpening

After the specimen had been machined, the tip of the notch was sharpened to create a crack tip. To sharpen the crack tip, a blade from a window scraping tool [41] was gently hammered 1mm in to the tip of the notch. The window scraping tool was used because it had a sharp edge, but also because it was thin enough to fit the 1mm wide notch while being sturdy enough to withstand the hits from a hammer without shattering. A nylon tip hammer was used to further prevent the blades from being destroyed while sharpening the tip. The crack depth of 1mm was chosen because a deeper crack significantly increases the risk of splitting the SCB-specimen while hammering the blade in the specimen, as was the case during the preliminary work. The standing specimen had support material in the notch which was removed with a putty knife prior to the crack sharpening.

To achieve a consistent crack depth for all the specimen, a method for gauging the depth of the crack had to be developed. Since the the tip of the crack should be located at the midpoint of the specimen height, the distance from the edge of the specimen to the crack tip should be $0.5 * r = 0.5 * 25mm = 12.5mm$. The fixture developed in Section 4.7 was therefore made with this dimension in mind. The depth of the slot made for the SCB-specimen was set to 12.5mm, which placed the edge of the notch 1mm above the top of the fixture. This means that when the blade was hammered down to where it was flush with the top of the fixture, the crack tip would be 12.5mm away from the edge of the specimen. This is visualised in Figure 24.

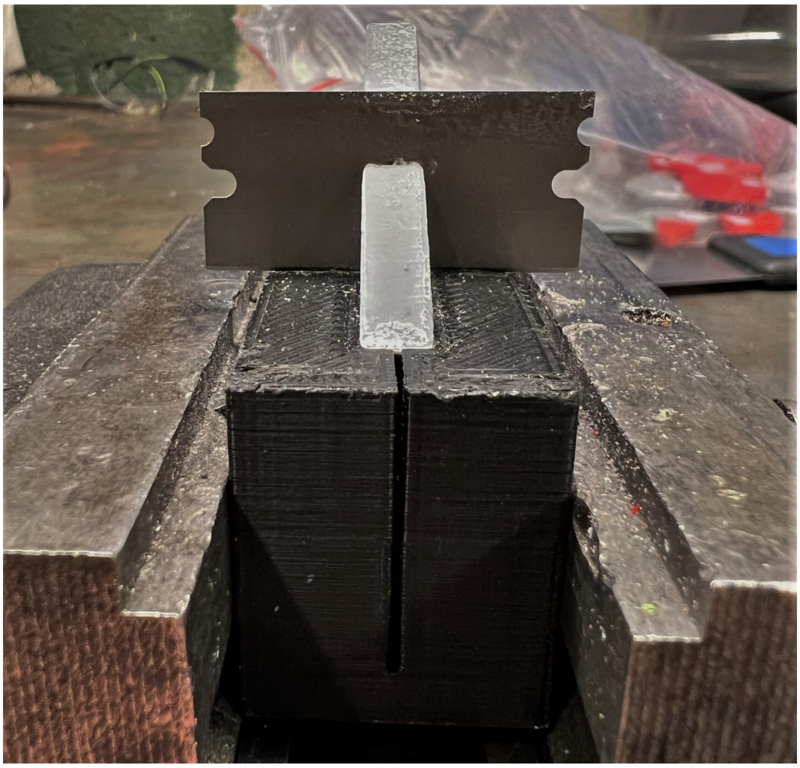

Figure 24: Getting the correct crack depth with the specimen fixture.

When using this fixture, it is important that the notch is perpendicular to the top of the fixture to get the correct crack length. If the notch is not perpendicular to the top of the specimen, the distance from the crack tip to the edge of the specimen would not be 12.5mm. For the specimen with 0° notch, this was done the same way the specimen were aligned before machining, showed in Figure 22. For the specimen with 15° 30° and 40° notch, this was more challenging to achieve. To help with this, three alignment-tools were made.

In Figure 25 a picture of the alignment-tools can be seen. The purpose of these was make the notch perpendicular to the specimen prior to cracking. This was necessary in order to get the correct crack depth. Each tool has a sloped part with a 15°, 30° or 40° incline. The tools are meant to be used with the specimen fixture and a precise vise. This will rotate the specimen correctly when tightening the vise, making the specimen ready for crack sharpening. Figure 26 shows the tools in use with a 40° specimen.

4.9 Digital Image Correlation

Digital image Correlation (DIC) is a method of capturing surface deformation during loading of a specimen. The DIC system works by photographing the specimen covered in a speckle pattern, during testing. The images is then processed in a software which generates a full-field strain image.

Figure 25: Angled notch alignment tools.

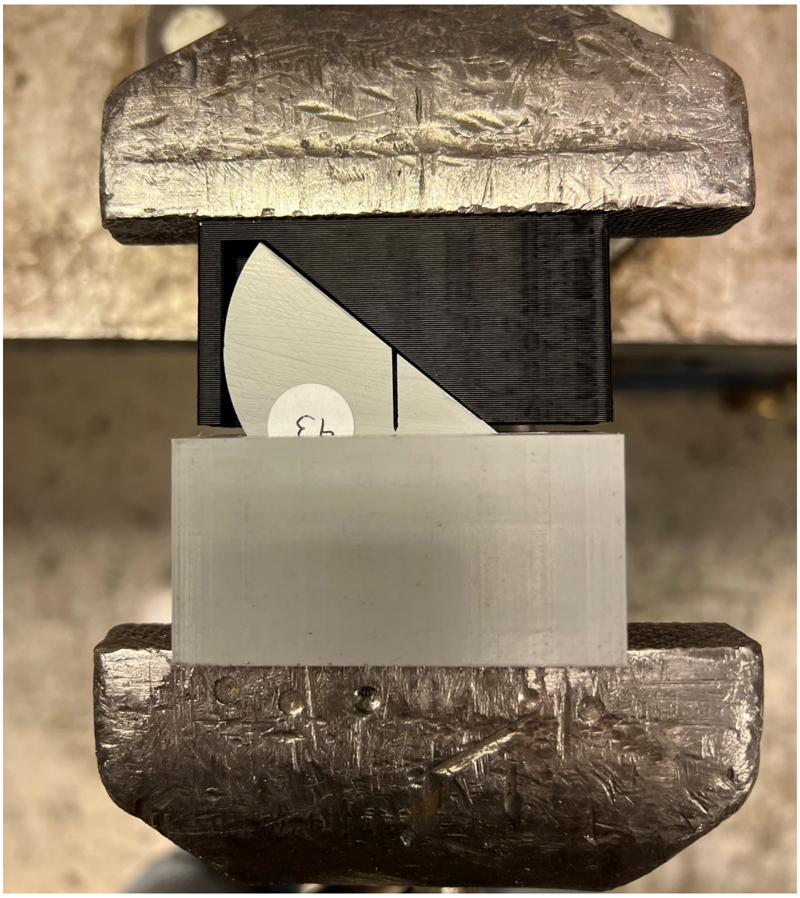

Figure 26: A 40° SCB-specimen getting aligned for crack sharpening.

Before capturing specimen deformation using DIC, the specimen need so be prepared with a speckle pattern. To prepare the specimen, a can of white and black spray paint was used. The specimen was first coated with a white layer to create contrast for the speckles. The black spray can was then used to carefully mist the surface of the specimen, leaving a fine speckle pattern as can be seen in Figure 27. The speckle pattern allows the DIC processing software to observe the change in the position of the dots relative to each other.

DIC was used while testing SCB-specimen and dogbone specimen. At least one of each unique SCB-specimen case were captured to calculate the strain field during loading. The SCB-specimen captured with DIC is highlighted with green text in Table 2 and Table 3. For the dogbone tests, each test was captured with DIC. The strain

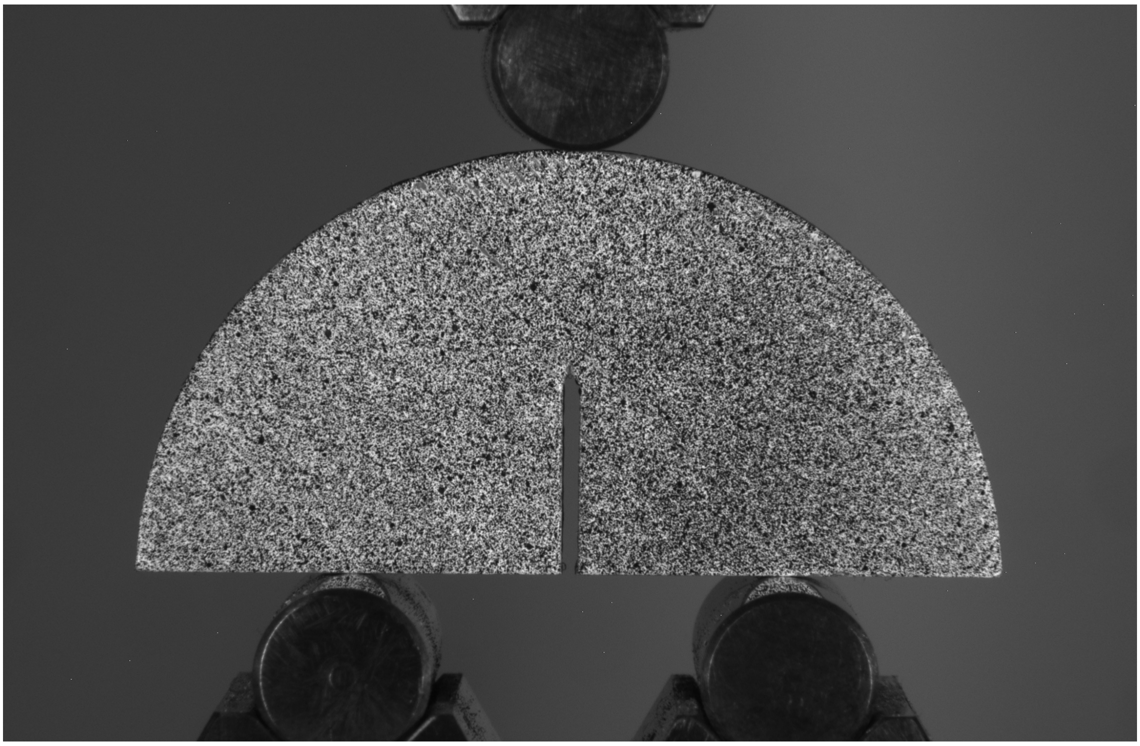

Figure 27: SCB-specimen prepared with speckle pattern for DIC capturing.

in X- and Y-direction were retrieved from the DIC software during post-processing, allowing the Young's modulus and Poisson's ratio to be measured.

4.10 Fracture Testing

The fracture testing was performed on a Instron ElectroPuls E10000 test system equipped with a Instron 3-point bend fixture with 10kN load capacity. During the tests, both applied load and displacement of the top anvil of the 3-point bend fixture were sampled at 20Hz. Specimen deformation was also captured for a select set of the specimen during the testing. This was done with a digital image correlation(DIC) system, which is explained in Section 4.9. In total, The fracture data of 120 specimen were gathered during the project.

One of the difficulties experienced in the preliminary work was to accurately adjust the span of the two lower anvils of the 3-point bend fixture, as well as correctly aligning the SCB-specimen in the fixture. To help with placing the specimen at the correct position for each test, an alignment tool was made to increase the accuracy of the placement. A picture of this tool can be seen in Figure 28.

The tool has the same shape as the lower half of a SCB-specimen plus an extra 5mm extension under for the semi-circle cutouts. These cutouts are have the same diameter of the support anvils on the Instron 3-point bend fixture. The cutouts are placed 25mm apart, from centre to centre. This makes it easy to get the proper width between the lower supports. The tool also help position the specimen at the correct position before a test. As can be seen in Figure 29, the sides of the

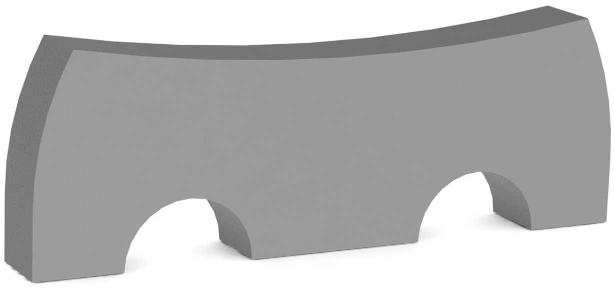

Figure 28: SCB-specimen alignment tool for 3-point bend fixture.

SCB-specimen is placed flush with the alignment tool. The cutouts of the alignment tool makes it so that the tool only can be placed square in all directions. It prevents it from rotating along its vertical axis, being tilted forwards or backwards and being miscentred. Placing the SCB-specimen next to and flush with the tool will therefore ensure with proper alignment. Once the specimen has been properly aligned, the test machine loads the specimen with 10N to keep it in place while the tool is lifted from the fixture.

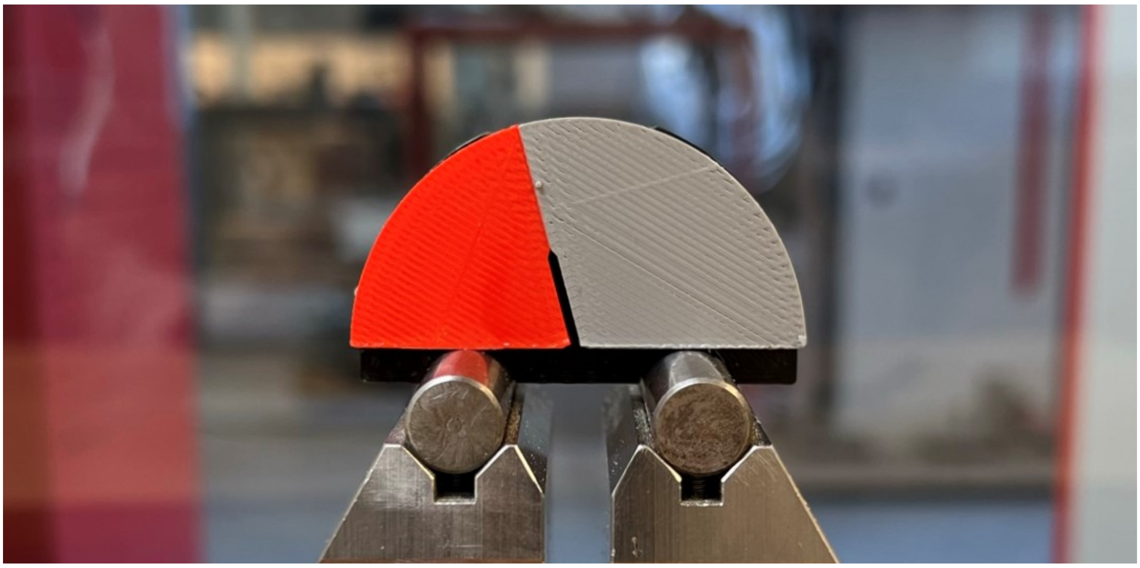

Figure 29: SCB-specimen placed in front of the alignment tool.

During the first testing session there were some specimen with a 30° and 40° crack which slid out of the fixture (Figure 30) before fracture at high load. This creates an out of plane fracture condition which meant the result from these test could no be used.

During these tests, the test machine was equipped with extensions (Figure 31a) from a previous experiment. These extensions were unnecessary long which added flexibility to the machine. This flexibility allowed the anvils of the 3-point bend fixture to move in relation to each other, causing the specimen to slide during loading. Removing these extensions (Figure 31b) reduced the overall length of the machine,

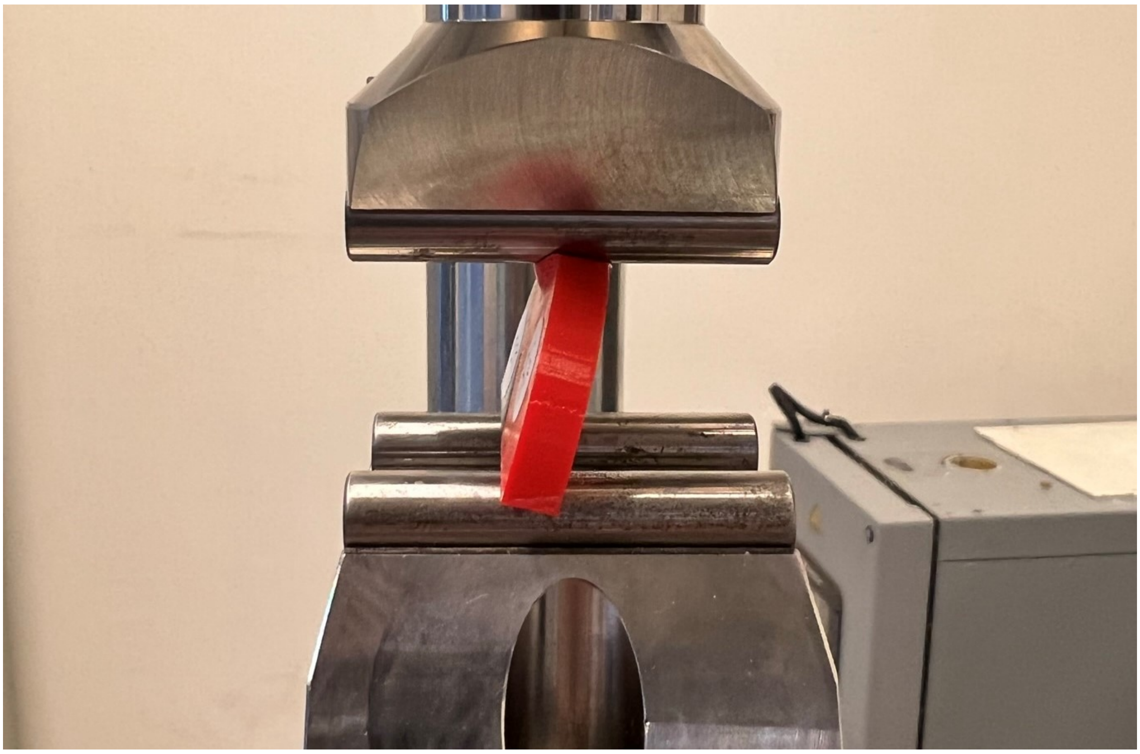

Figure 30: SCB-specimen sliding during testing.

which increased the stiffness of the machine. This change in the machine setup prevented any more specimen to slide out during testing.

(a) With extensions.

(b) Without extensions.

Figure 31: Instron test system with and without extensions.

There were also problems for the 40° SCB-specimen during the initial testing. The mode II fracture strength was greater than expected, causing the specimen not to fracture. Instead the specimen were severely deformed before the test machine aborted the test because the actuator had reached its maximum stroke length. The result of these tests can be seen in Figure 32. To work around this, the span length for the bottom rollers in the three point fixture was set to 36mm for the 40° specimen, instead of the 25mm span length which was initially intended. This change introduces mode I fracture forces during the test, causing the specimen to fracture properly.

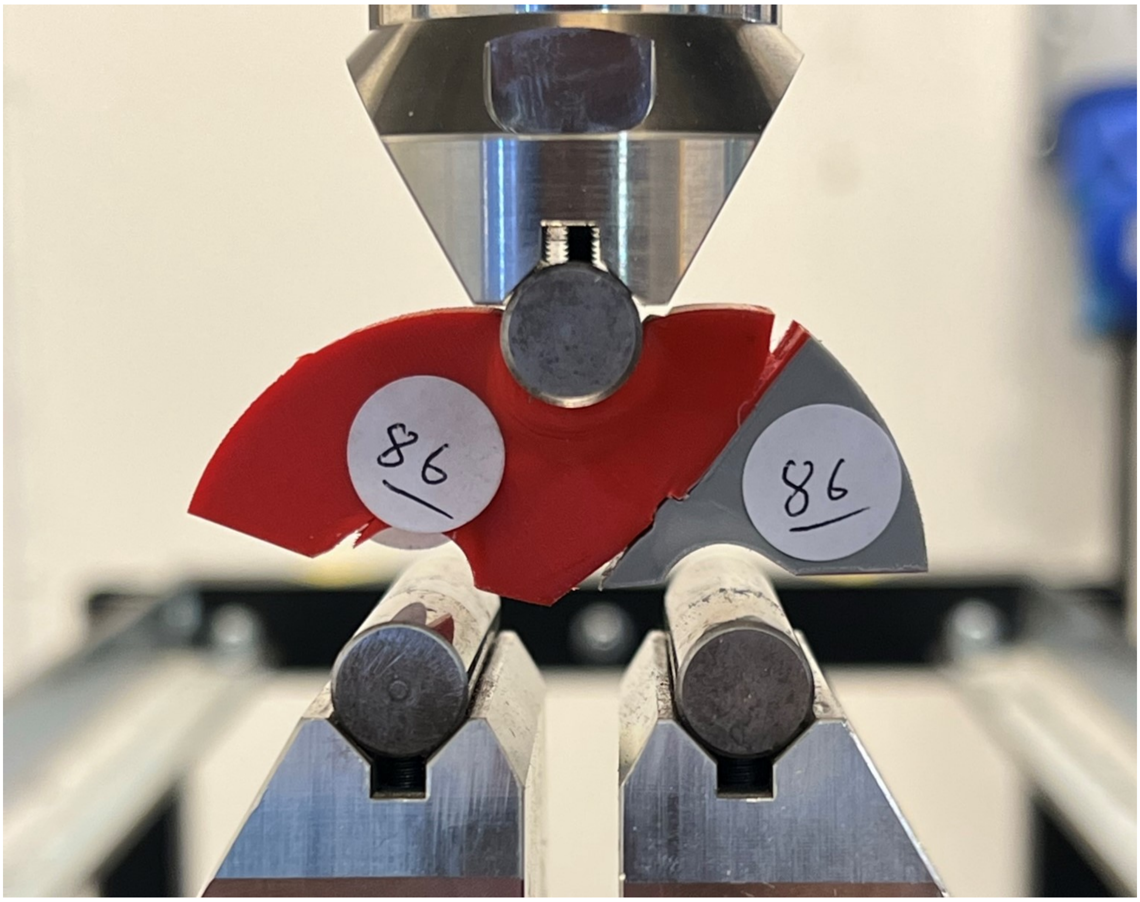

Figure 32: 40° SCB-specimen which did not fracture during testing.

During and after the fracture testing, the data was processed using python scripts. The scripts were made to plot fracture load relative to notch angle, get the fracture force for all specimen and plot the data to evaluate the load-displacement graph of the test. These scripts can be found in Appendix D.

4.11 Stress Intensity Factor

To determine the plane strain fracture toughness, denoted K_{Ic}, from the fracture loads, the stress intensity factor (SIF) at the crack tip must be determined. This is done with a simulation of the SCB-specimen in Abaqus. A 2D SCB-Specimen is modelled in Abaqus with a 50mm diameter and 12.5mm long crack, with a plane strain thickness of 6mm. The model is then assigned elastic material behaviour. The magnitude of the material properties were set to the material properties collected in

Section 5.6, however the properties can be set to any number as the SIF is geometrically defined. The face of the specimen was then partitioned with the path of the crack and with some extra lines to prepare for mesh refinement, which can be seen in Figure 33.

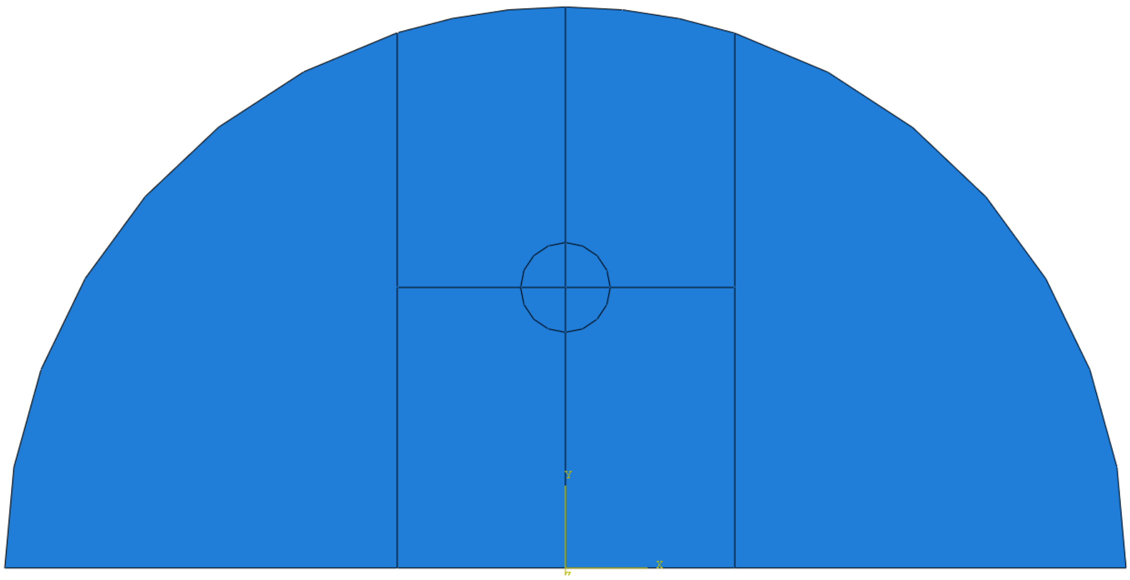

Figure 33: 0 Degree specimen partitioned in Abaqus.

A crack tip was then assigned to the center of the circle, with the crack extension direction assigned as a q-vector in the direction of the crack path. The crack was modelled as a contour integral crack with a midside node parameter of 0.25 and with the ”Collapsed element side, single node” option chosen under the ”Degenerate Element Control at Crack Tip/Line” section. A history output request was then created for the crack, to get the SIF at the crack tip after the simulaton has been completed. The history output was configured with 10 contours and with a maximum tangential stress crack initiation criterion.

The model was then bounded with a X and Y displacement boundary condition 12.5mm to the left of the crack and a Y displacement boundary condition 12.5mm to the right of the crack. A unit load of 1N was also added to the top of the specimen, in negative Y-direction. The constraints and load can be seen in Figure 34.

When meshing the model, the global mesh size was set to 1. The mesh in the circle around the crack tip was refined to a total of 40 nodes evenly dispersed around the circle while the cross in the circle also had 40 nodes, the nodes was placed with a bias ratio of 5, making the mesh gradually finer towards the tip of the crack. When assigning mesh controls the areas outside the circle was given quadratic element shape with structured meshing technique and the area inside the circle was given quad-dominated element shape with sweep meshing technique. Finally the element type was set to be eight-node plane strain element (CPE8R). The final mesh result can be seen in Figure 35.

After the meshing had been done, the simulation could be submitted to get the SIF at the crack.

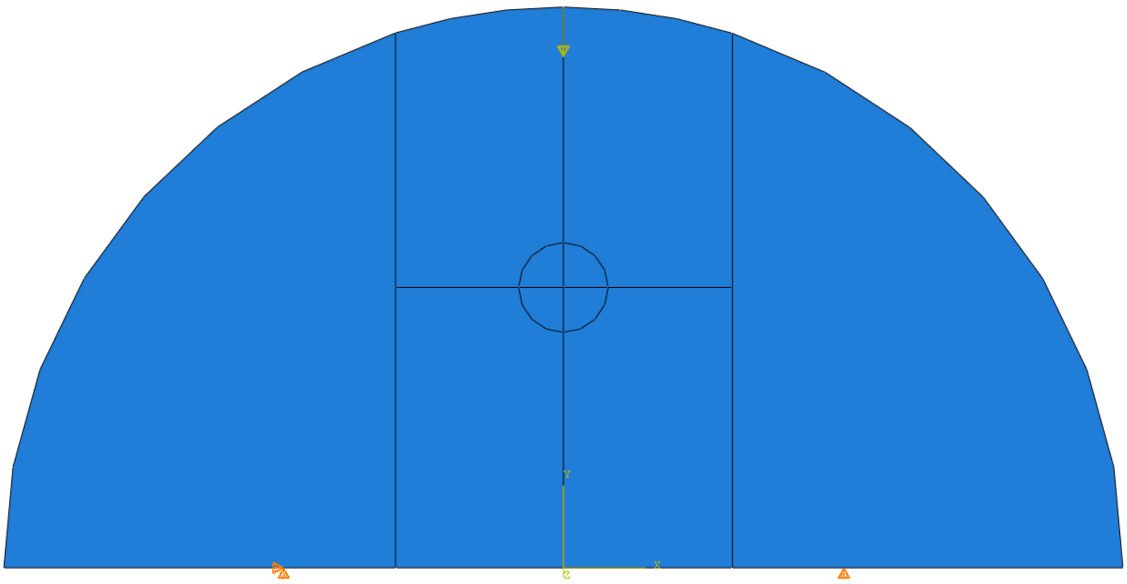

Figure 34: SCB-specimen with boundary conditions and load in Abaqus.

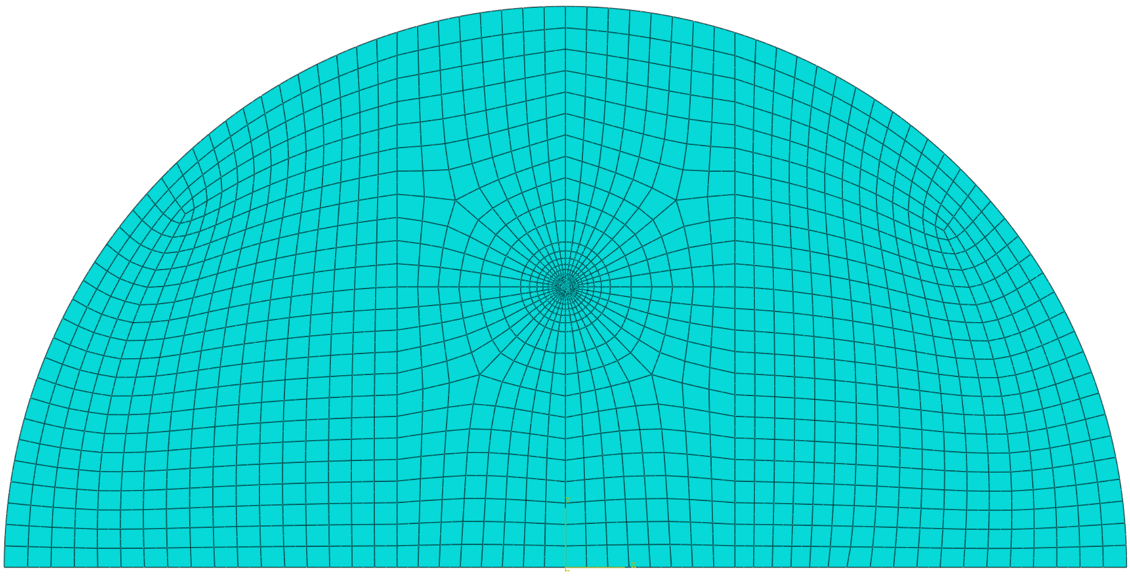

Figure 35: SCB-specimen meshed in Abaqus.

This process was repeated for SCB-specimen models with 15° 30° and 40° crack angle to get the SIF for each configuration.

4.12 Fracture Toughness

With the fracture loads for the 0° SCB-specimen and the stress intensity factor (SIF) calculated in Section 4.11, the fracture toughness (K_{Ic}) of the bimaterial interface and materials can be calculated. The fracture toughness is found using Equation 2

$$K_{Ic} = K * P \tag{2}$$

Where K is the stress intensity factor and P is the experimantal fracture load.

4.13 Fracture Prediction Using Strain Energy Density

Fracture load predictions were conducted using the average strain energy density (SED) method for the SCB-specimen. To predict the fracture load using SED, a fracture criterion must be established based on the material around the crack tip. For this project the Averaged Strain Energy Density (ASED) criterion is used for prediction of the fracture loads. The ASED criterion states that a specimen will fracture when the strain energy within a given control volume around the crack tip is equal to the critical strain energy density of the material. [42]

The control volume around the crack tip is determined from the specimen material properties. The process of measuring the properties of the materials used in this project is described in Section 4.14.

The following expression is used to determine the radius, R_c, of the control volume around the crack tip [42]:

$$R_c = \frac{(1+\nu)(5-8\nu)}{4\pi}\left(\frac{K_{Ic}}{\sigma_t}\right)^2 \tag{3}$$

where ν is the Poisson's ratio of the material, K_{Ic} is the fracture toughness of the material and σ_t is the ultimate tensile strength of the material.

With the critical radius, R_c, known the elastic strain energy and volume within the control circle can be calculated in a FEA software. In this project, Abaqus was used to simulate elastic strain energy density (ELSE) and the element volume (EVOL) within the control circle. The process of getting values for ELSE and EVOL is explained further in Section 4.13.1. Using Equation 4, the average strain energy density (ASED) within the control volume can be calculated.

$$ASED = \frac{ELSE}{EVOL} \tag{4}$$

With the ASED ($\overline{W}$) value calculated, a critical SED (W_c) must be determined before the fracture predictions can be calculated. The critical SED value varies from material to material, and can be calculated with σ_t and E using Equation 5 if the material behaviour is ideally brittle.[43]

$$W_c = \frac{\sigma_t^2}{2E} \tag{5}$$

Now that $\overline{W}$ and W_c has been determined, the theoretical fracture loads (P_{th}) can be calculated using the relation in Equation 6.[42]

$$\frac{P_{th}}{P} = \sqrt{\frac{W_c}{\overline{W}}} \tag{6}$$

Where P is the load applied in the ASED simulations explained in Section 4.13.1.

4.13.1 Elastic Strain Energy Density

To predict the fracture loads using strain energy density, the average strain energy density of the SCB-specimen must be determined. This is done with a simulation of the SCB-specimen in Abaqus. To do this, a 2D SCB-specimen is modelled in Abaqus with a 50mm diameter and 12.5mm long crack, with a plane strain thickness of 6mm. The model is then assigned elastic material behaviour. The material properties were set to the material properties collected in Section 5.6. Once the specimen has been modelled, the face is partitioned with a path for the crack and a circle around the crack tip with a radius of the calculated control area radius determined by Equation 3.

A crack tip was then assigned to the centre of the circle with the crack extension direction assigned as a q-vector in the same direction as the crack path. The crack was modelled as a contour integral crack with a midside node parameter of 0.25 and with the ”Collapsed element side, single node” option chosen under the ”Degenerate Element Control at Crack Tip/Line” section. A set called ”Circle” was then assigned to the area inside the control circle. A field output request for ”Energy” and ”Volume/Thickness/Coordinates” was then created where the domain was set to ”Circle”.

The model was then bounded with a X and Y displacement boundary condition 12.5mm to the left of the crack and a Y displacement boundary condition 12.5mm to the right of the crack. A unit load of 1N was also added to the top of the specimen, in negative Y direction.

A global element size of 1mm was set for the model, while the element size in the circle around the crack tip was set to 0.2mm. A mesh size analysis was performed to validate the accuracy of the element size (see Section 4.13.2). The elements of the area outside the control circle was given ”Quad” element shape with a Structured meshing technique. The elements inside the control circle was given ”Quad-dominated” element shape with a sweep meshing technique. Finally the element type was set to be eight-node plane strain elements (CPE8R). The final result can be seen in Figure 36

After the meshing had been done, the simulation could be submitted. After the simulation had finished, a display group containing the ”Circle” set was created and ELSE was selected in the ”Field output dialog”. This makes Abaqus display the elastic strain energy (ELSE) within the control volume, which is shown in Figure 37. The exact total amount of elastic strain energy within the control volume can then be obtained with the ”Query” tool by choosing ”Probe values”, selecting the ”Circle” display group and clicking ”Write to File”. To get the size of the control volume ”EVOL” must be selected in the ”Field output dialog”. The volume can then be extracted following the same procedure as when getting ”ELSE”.

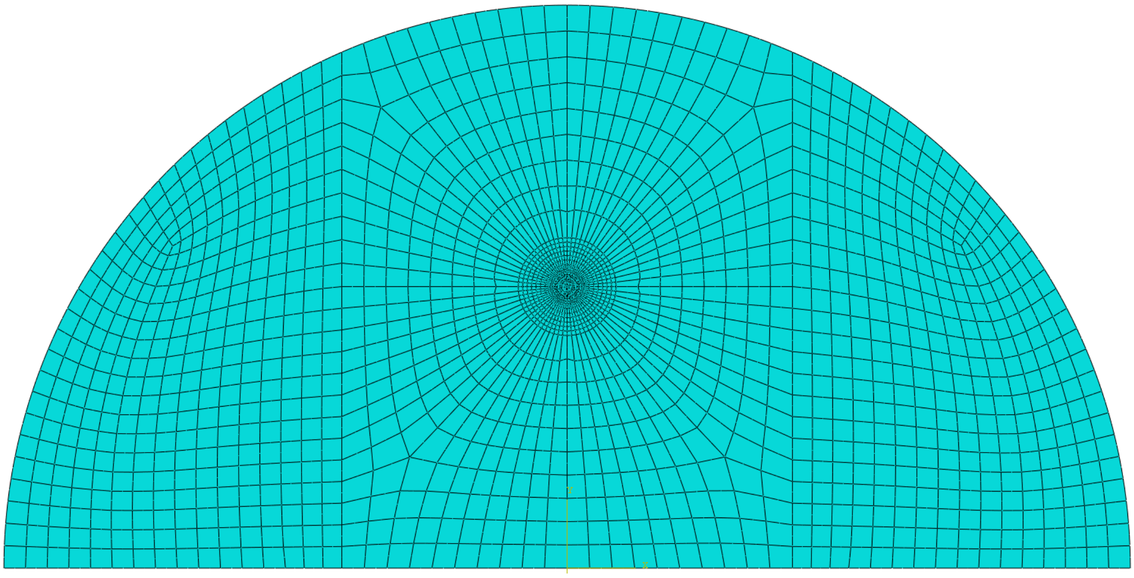

Figure 36: SCB-specimen meshed in Abaqus.

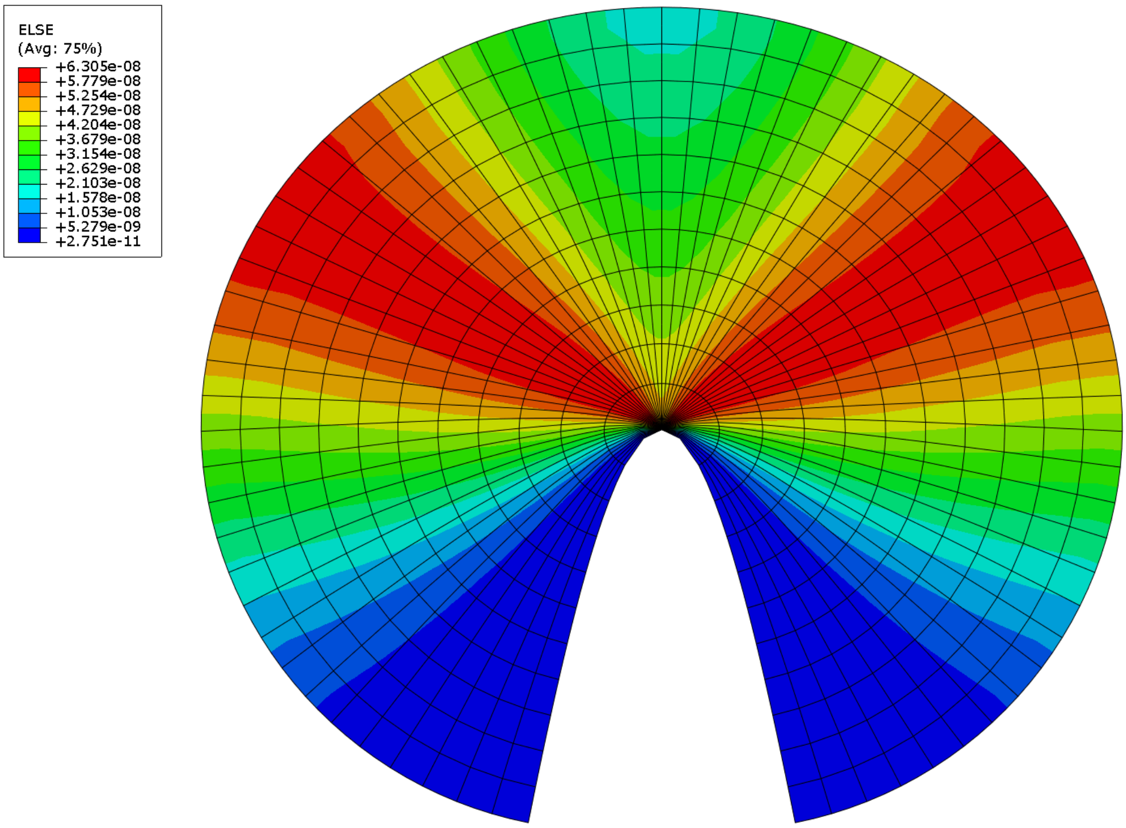

Figure 37: Elastic strain energy within control volume simulated in Abaqus.

This process was repeated for SCB-specimen with 15°, 30° and 40° crack angle for each of the 6 material properites.

4.13.2 Mesh Sensitivity analysis

To verify if the mesh in the SED analysis was sufficiently refined, a mesh sensitivity analysis was performed. The elastic strain energy was gathered from a SCB-specimen with varying element sizes within the control circle. The analysis was performed on a 0° SCB-specimen with a 2.67mm control radius around the crack tip. Meshes with element size from 2mm to 0.01mm was tested. Each result was compared to the previous mesh size to see the change in accuracy.

4.14 Tensile Testing

The tensile test specimen printed in Section 4.4 were tested in a MTS Criterion Model 42 test system equipped with manual wedge grips. The testing was performed with a constant cross head speed of 2 mm/minute while cross head displacement, force and time was logged at a rate of 10Hz. Wile the specimen were loaded, the surface deformation of the specimen were captured with DIC.

5 Results

In this section the results from the experimental fracture and tensile tests are presented. The fracture toughness, fracture prediction, UTS, Young's modulus and Poisson's ratio are also presented along with the results from the SIF and ASED simulations. Finally the strain fields of the SCB-specimen are shown before pictures of the crack path of each specimen is presented.

5.1 Fracture Load

The fracture loads for the SCB-specimen where the crack initiated from the crack tip can be seen in Figure 38. Some SCB-specimen had crack initiation from the beginning of the notch tip, like specimen 55 and 56 Figure 51. These loads were excluded from Figure 38. In Figure 39 the fracture force for all SCB-specimen regardless of crack initiation location are included. A detailed list with fracture loads for every specimen can be seen in Appendix E.

In Figure 40 the fracture loads of the standing specimen are compared to the fracture loads of the laying specimen.

Figure 41 compares the fracture loads of bimaterial SCB-specimen with grey half lower to the specimen with red half lower, as explained in Section 4.3.3

Figure 38: Mean fracture load of SCB-specimen where crack initiated from the crack tip.

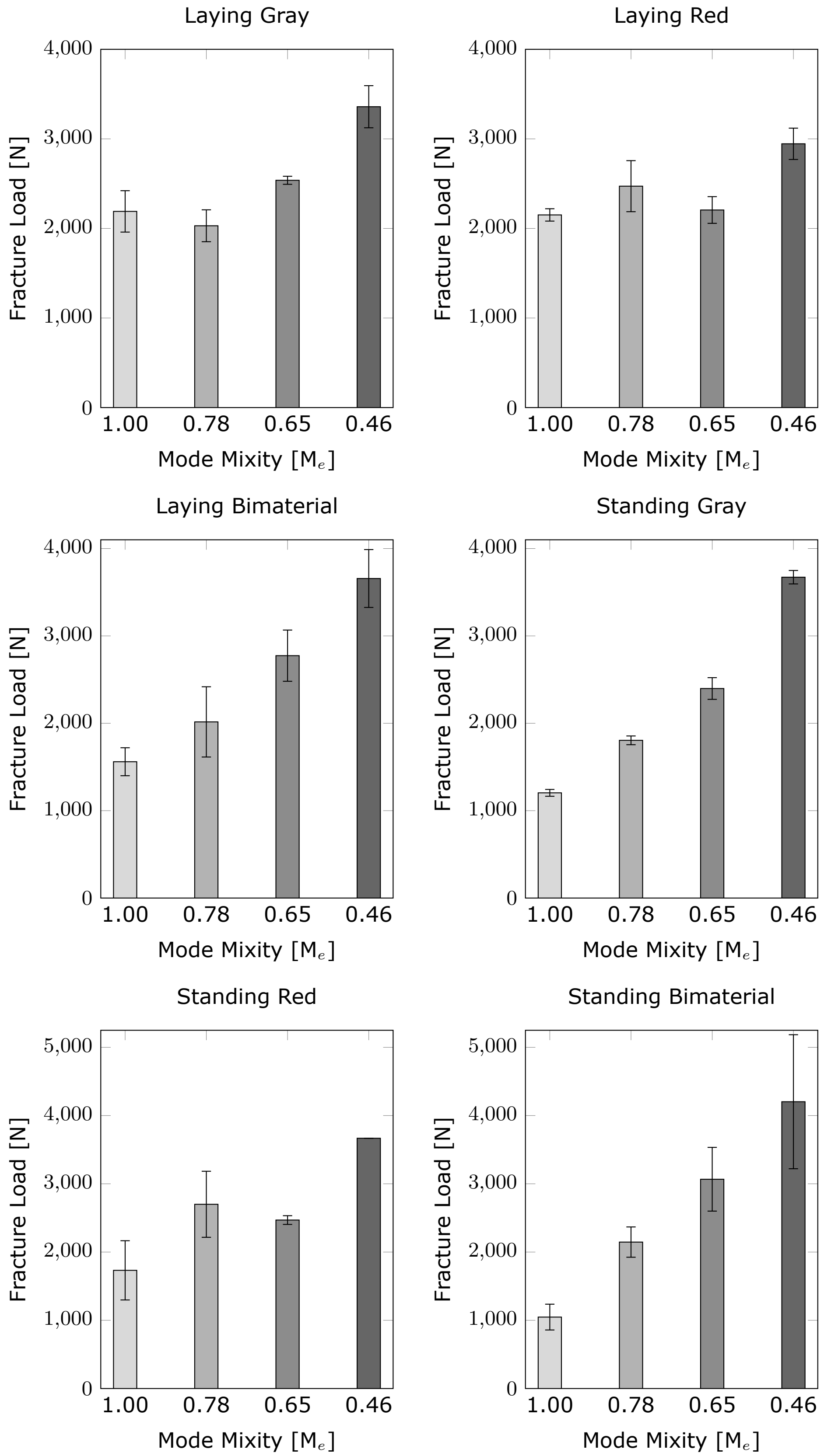

Figure 39: Mean fracture load for all SCB-specimen.

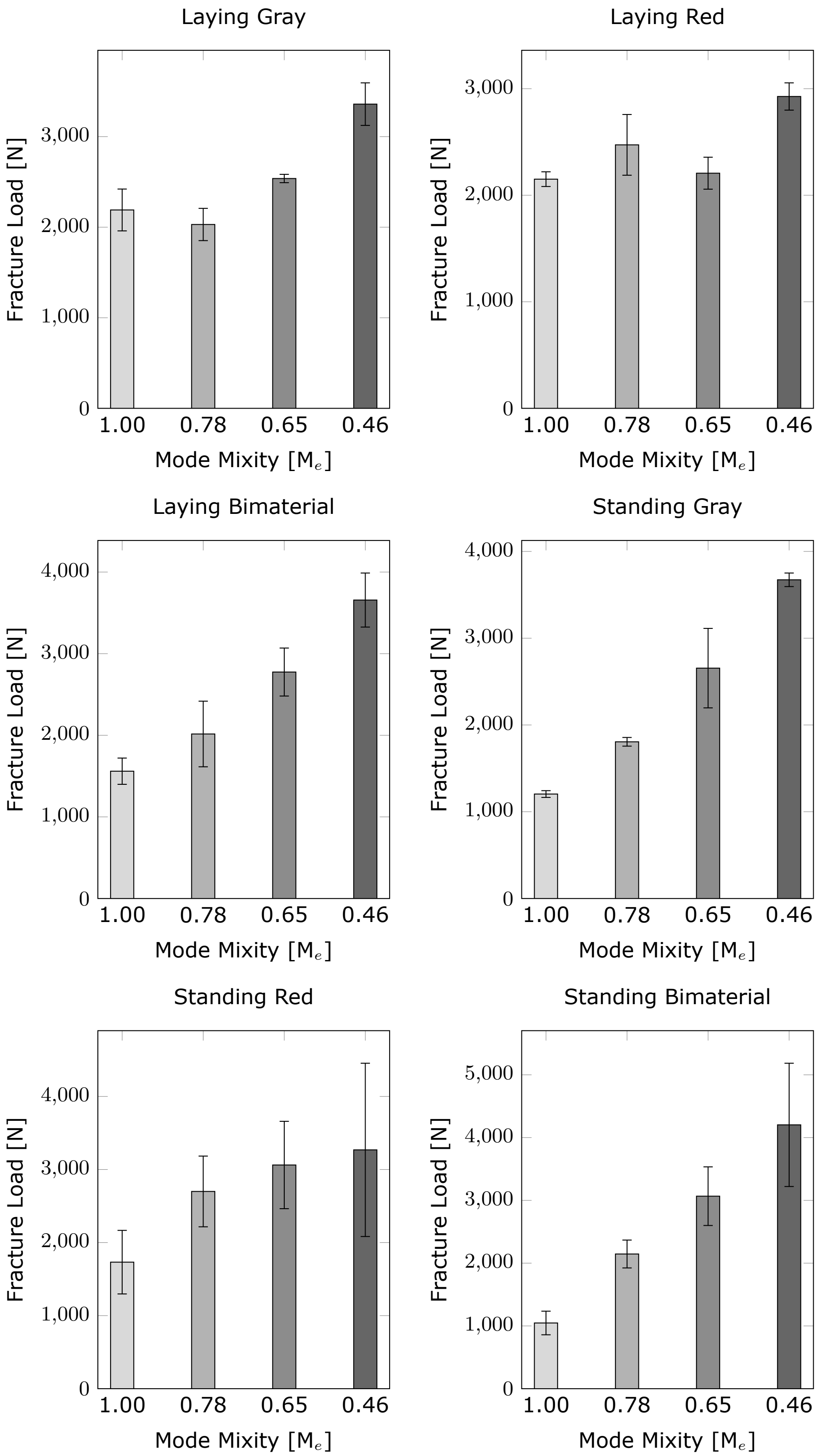

Figure 40: Fracture load of laying compared to standing specimen.

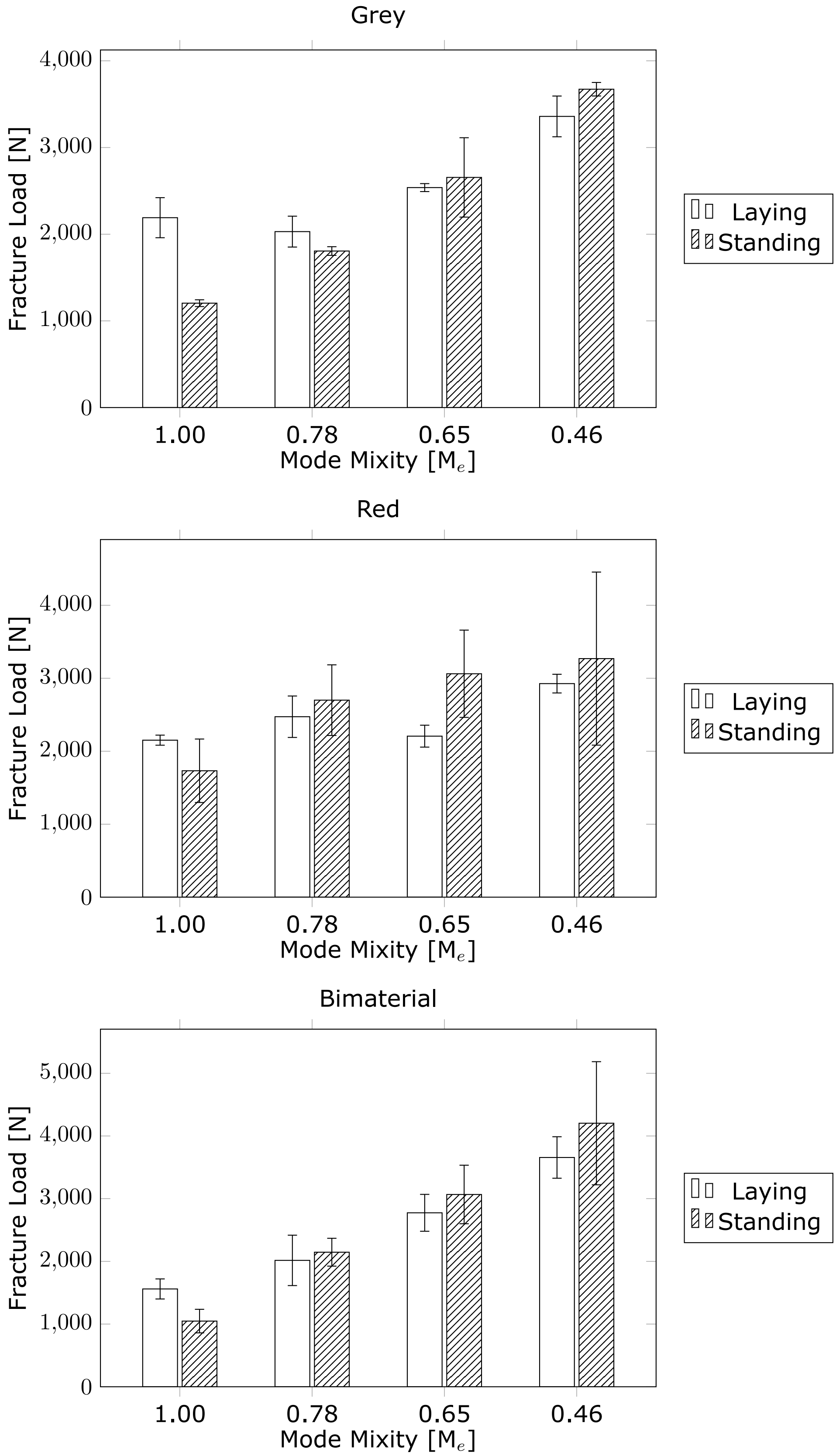

Figure 41: Mean fracture load for bimaterial specimen with "grey half lower" compared to "red half lower".

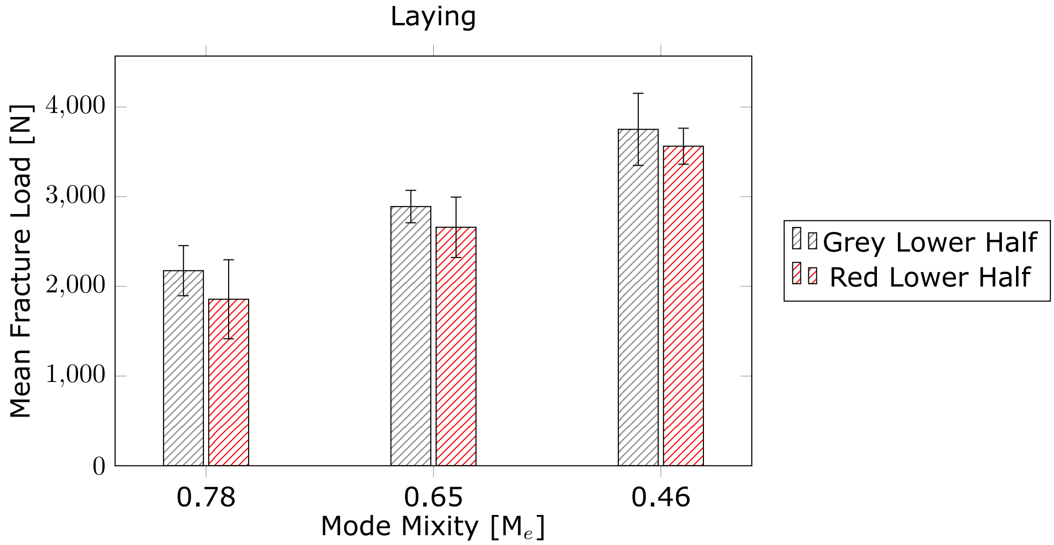

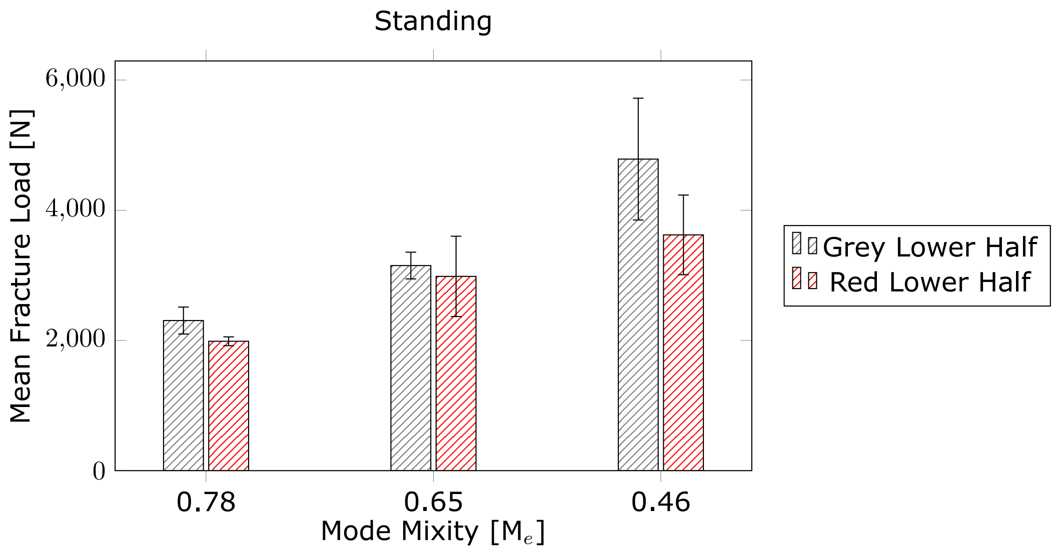

5.2 Stress Intensity Factor

The results from the simulations explained in Section 4.11 can be seen summarized in Table 6

Table 6: Stress intensity factor of SCB-specimen with different crack angles.

Crack angle [°]	Support span [mm]	K_I [MPa mm$^{0.5}$]	K_{II} [MPa mm$^{0.5}$]	M$_e$
0	25	7.55e-02	0	1.00
15	25	5.89e-02	2.10e-02	0.78
30	25	2.44e-02	2.77e-02	0.46
40	25	1.17e-03	2.58e-02	0.03
40	36	4.57e-02	2.78e-02	0.65

5.3 Fracture Toughness

The fracture tougness (K_{Ic}) for the bimaterial interface and control materials can be seen in Table 7.

Table 7: Fracture Toughness of the material in different conditions.

Material:	SIF[$\frac{\text{MPa m}^{0.5}}{N}$]:	Fracture Load[N]:	K_{Ic}[MPa m$^{0.5}$]:
Laying Grey	7.55e-02	2190	5.23
Laying Red	7.55e-02	2151	5.14
Laying Bi	7.55e-02	1560	3.72
Standing Grey	7.55e-02	1204	2.88
Standing Red	7.55e-02	1732	4.14
Standing Bi	7.55e-02	1047	2.50

5.4 Fracture Prediction

The simulated average strain energy density (ASED), predicted fracture loads (P_{th}) and its discrepancy to the actual fracture loads (P_{exp}) are shown in Table 8. The spreadsheet where the average strain energy density and fracture predictions were calculated can be seen in Appendix F.

5.5 Mesh Sensitivity Analysis

The data from the mesh sensitivity analysis can be found in Table 9.

Table 8: Fracture prediction using strain energy density.

Material	Orientation	Crack angle[°]	M_e	$\overline{W}$[mJ/mm^3]	P_{exp} [N]	P_{th} [N]	Discrepancy
Grey	Laying	0	1.00	6.53E-08	2190	2457	12.16 %
Grey	Laying	15	0.78	5.40E-08	2030	2702	33.11 %
Grey	Laying	30	0.46	3.63E-08	3359	3295	-1.90 %
Grey	Laying	40	0.65	5.87E-08	2538	2590	2.05 %
Red	Laying	0	1.00	9.62E-08	2151	2357	9.56 %
Red	Laying	15	0.78	7.97E-08	2473	2589	4.71 %
Red	Laying	30	0.46	5.20E-08	2945	3206	8.86 %
Red	Laying	40	0.65	8.49E-08	2207	2508	13.67 %
Bimaterial	Laying	0	1.00	1.26E-07	1560	1670	7.04 %
Bimaterial	Laying	15	0.78	1.05E-07	2016	1834	-9.03 %
Bimaterial	Laying	30	0.46	6.70E-08	3657	2291	-37.37 %
Bimaterial	Laying	40	0.65	1.09E-07	2775	1794	-35.34 %
Grey	Standing	0	1.00	1.38E-07	1204	1284	6.64 %
Grey	Standing	15	0.78	1.15E-07	1806	1410	-21.93 %
Grey	Standing	30	0.46	7.31E-08	3673	1767	-51.88 %
Grey	Standing	40	0.65	1.19E-07	2399	1384	-42.30 %
Red	Standing	0	1.00	6.93E-08	1732	1896	9.45 %
Red	Standing	15	0.78	5.76E-08	2700	2079	-22.99 %
Red	Standing	30	0.46	1.26E-07	3668	1404	-61.72 %
Red	Standing	40	0.65	2.08E-07	2469	1094	-55.69 %
Bimaterial	Standing	0	1.00	9.12E-08	1047	1161	10.88 %
Bimaterial	Standing	15	0.78	7.54E-08	2146	1277	-40.51 %
Bimaterial	Standing	30	0.46	4.96E-08	4203	1575	-62.53 %
Bimaterial	Standing	40	0.65	8.17E-08	3067	1227	-60.00 %

Table 9: Results from mesh sensitivity analysis for ELSE simulation of 0° SCB-specimen.

Element Size [mm]	ELSE [mJ]	Change from previous element size[%]
3	2.800e-05	-
2	2.800e-05	0.0
1.8	2.827e-05	1.0
1.6	2.970e-05	5.0
1.4	2.980e-05	0.3
1.2	2.988e-05	0.3
1	3.032e-05	1.5
0.8	3.037e-05	0.2
0.6	3.058e-05	0.7
0.4	3.079e-05	0.7
0.2	3.091e-05	0.4
0.1	3.098e-05	0.2
0.001	3.103e-05	0.2

5.6 Material Properties

In this section the results from the tensile testing and the material properties computed with DIC are listed.

5.6.1 Ultimate Tensile Strength

The ultimate tensile strength of the red, grey and bimaterial dogbones in standing and laying orientation can be seen in Figure 42.

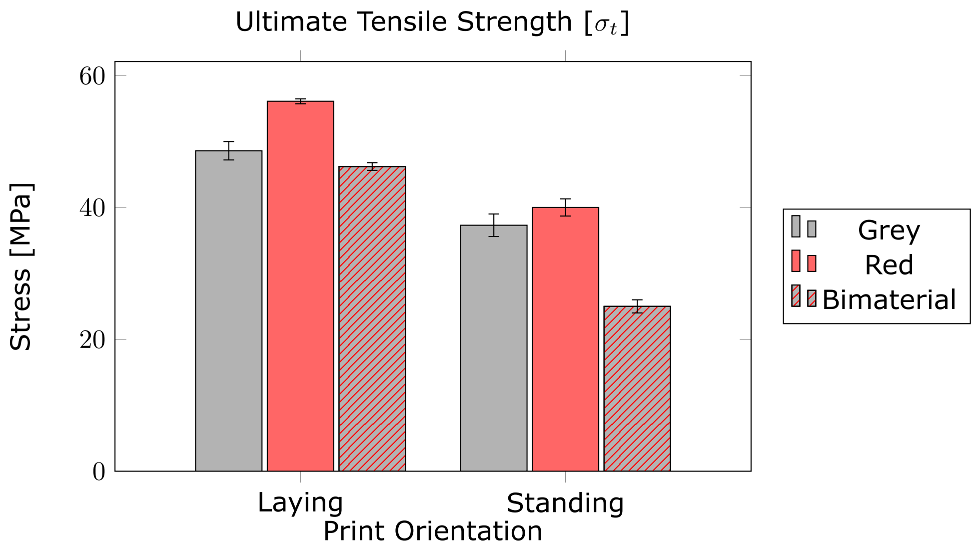

Figure 42: Ultimate tensile strength of red, grey and bimaterial dogbones printed in laying and standing orientation.

5.6.2 Young's Modulus

The Young's modulus of the red, grey and bimaterial dogbones in standing and laying orientation can be seen in Figure 43.

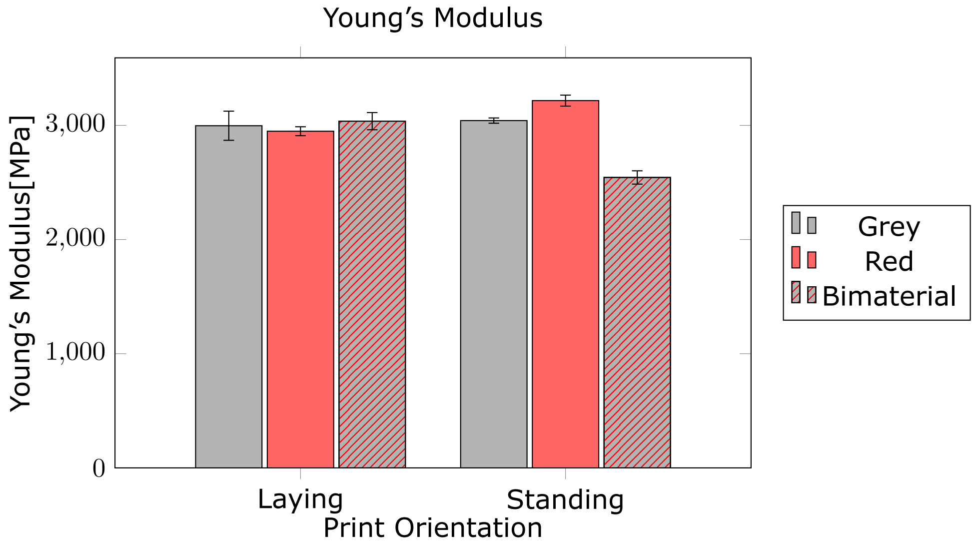

Figure 43: Young's modulus of red, grey and bimaterial dogbones printed in laying and standing orientation.

5.6.3 Poisson's Ratio

The Poisson's ratio of the red, grey and bimaterial dogbones in standing and laying orientation can be seen in Figure 44.

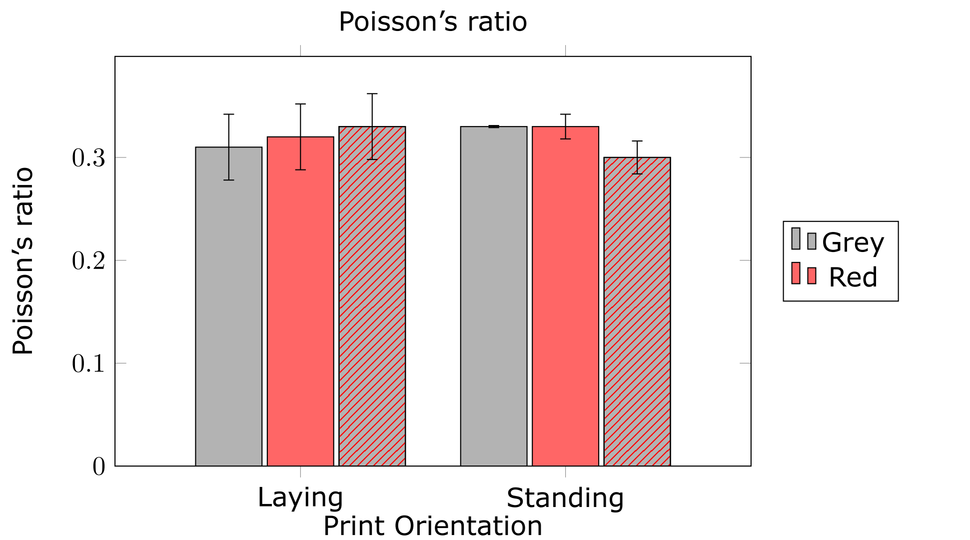

Figure 44: Poisson's ratio of red and grey dogbones printed in laying and standing orientation.

5.7 Strain Fields SCB-Specimen

The strain fields of the DIC-captured SCB-specimen during loading can be seen in Figure 45, 46, 47, 48 and 49.

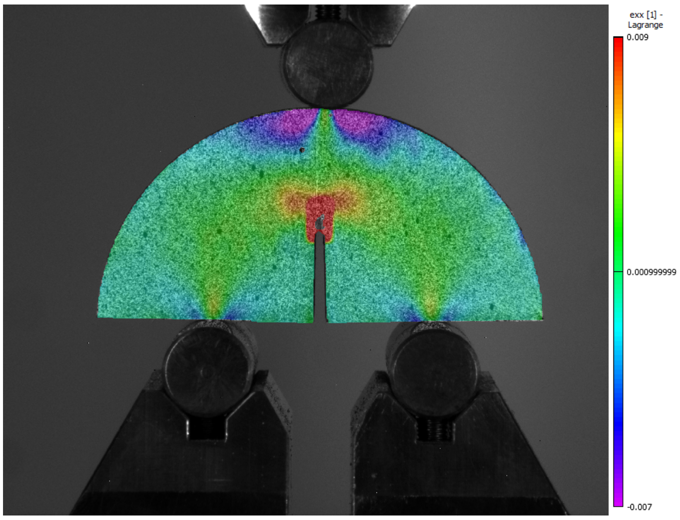

(a) Specimen 1: 0° laying bimaterial SCB-specimen.

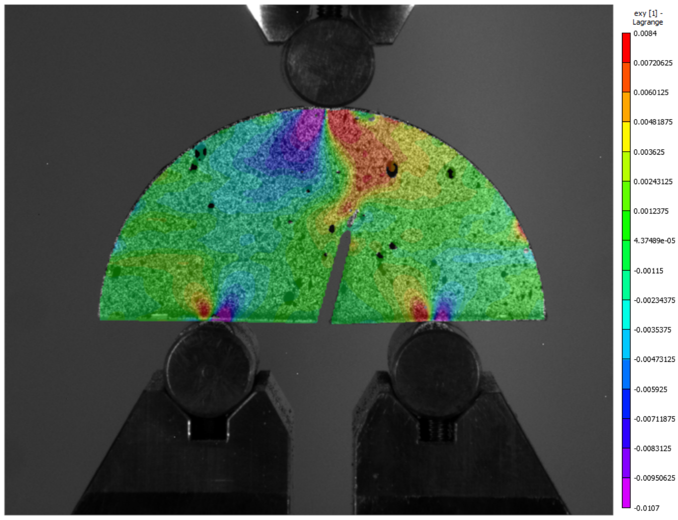

(b) Specimen 6: 15° laying bimaterial SCB-specimen with red half lower.

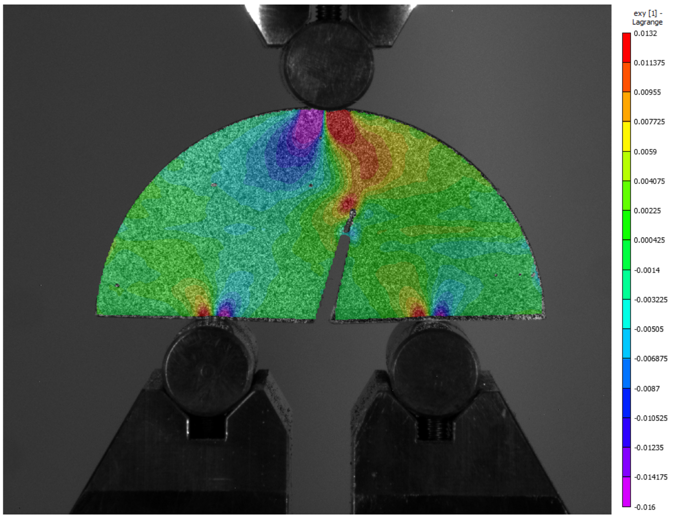

(c) Specimen 10: 15° laying bimaterial SCB-specimen with grey half lower.

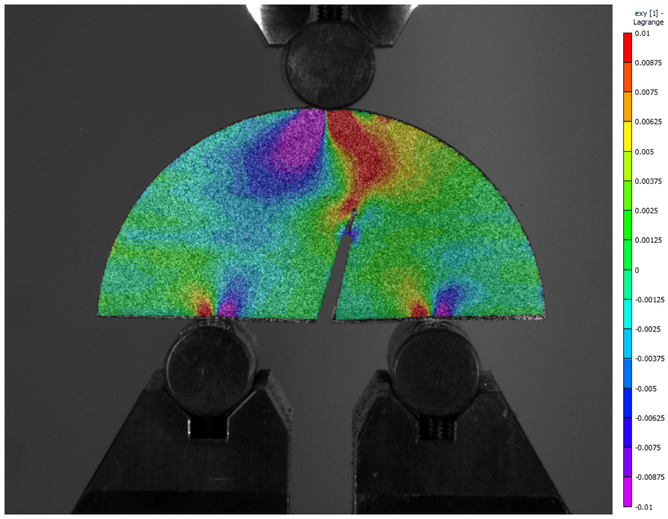

(d) Specimen 13: 30° laying bimaterial SCB-specimen with red half lower.

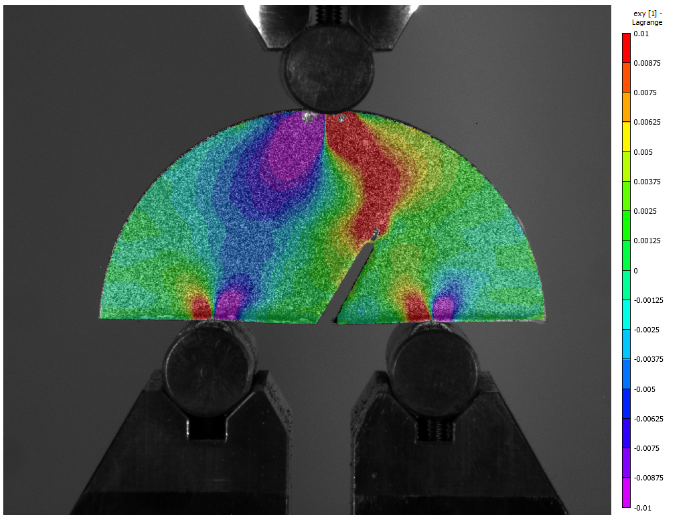

(e) Specimen 17: 30° laying bimaterial SCB-specimen with grey half lower.

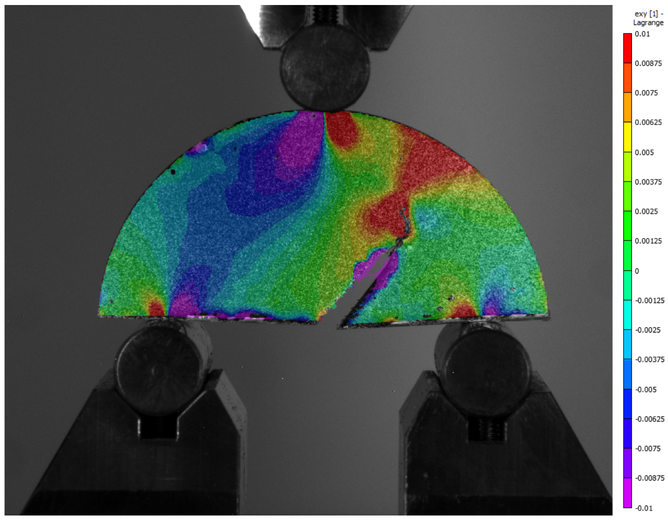

(f) Specimen 22: 40° laying bimaterial SCB-specimen with red half lower.

Figure 45: Strain field for SCB-specimen 1, 6, 10, 13, 17 and 22.

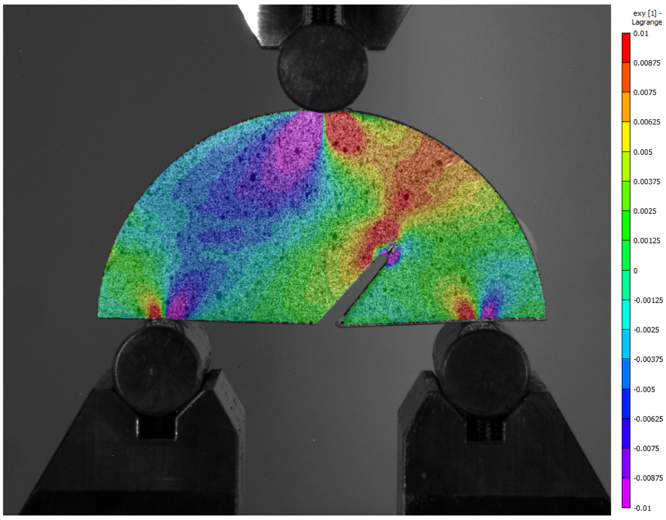

(a) Specimen 26: 40° laying bimaterial SCB-specimen with grey half lower.

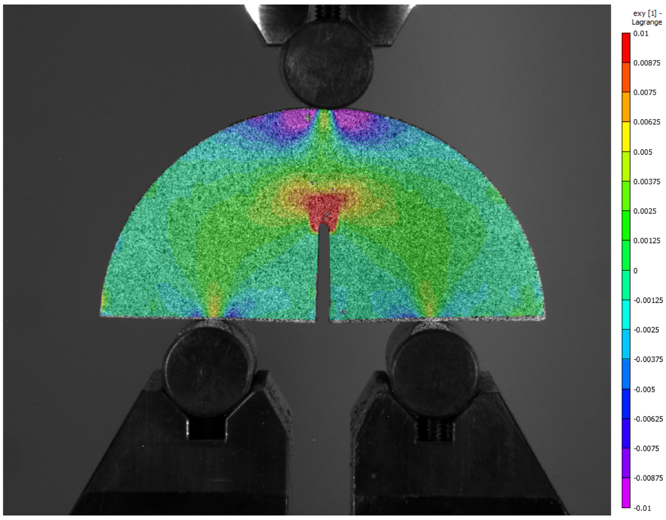

(b) Specimen 29: 0° laying grey single-material SCB-specimen.

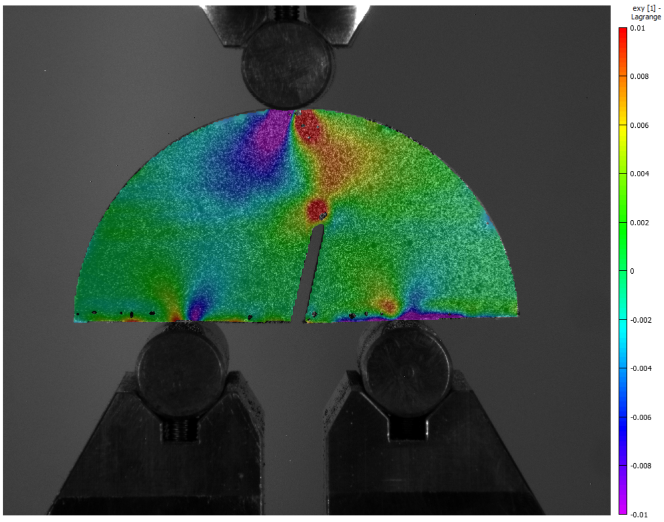

(c) Specimen 33: 15° laying grey single-material SCB-specimen.

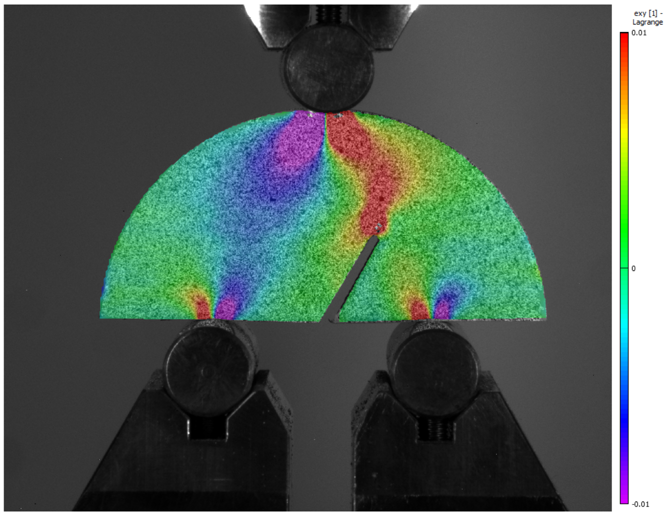

(d) Specimen 37: 30° laying grey single-material SCB-specimen.

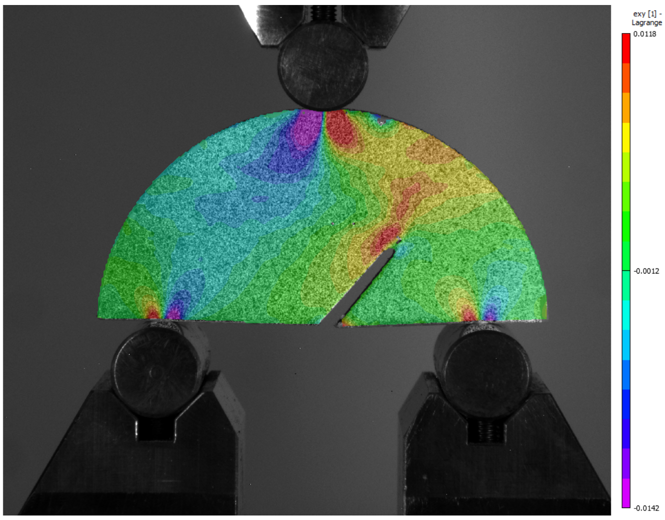

(e) Specimen 41: 40° laying grey single-material SCB-specimen.

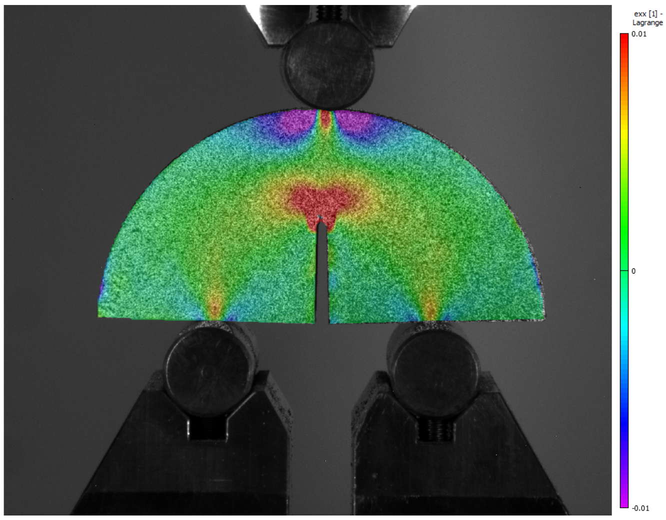

(f) Specimen 45: 0° laying red single-material SCB-specimen.

Figure 46: Strain field for SCB-specimen 26, 29, 33, 37, 41 and 45.

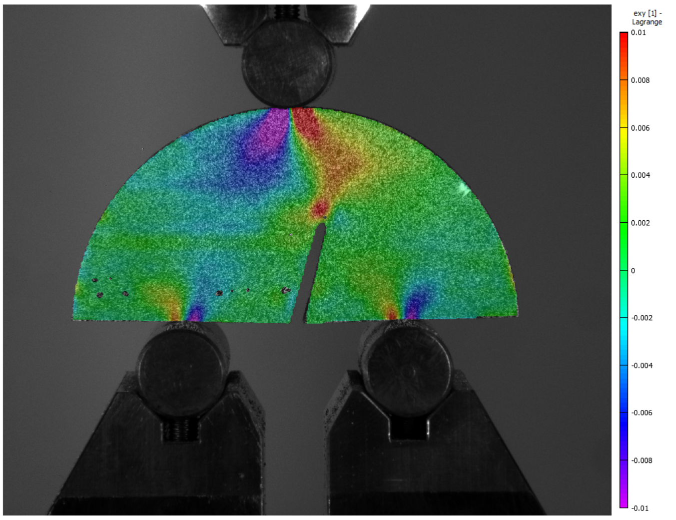

(a) Specimen 49: 15° laying red single-material SCB-specimen.

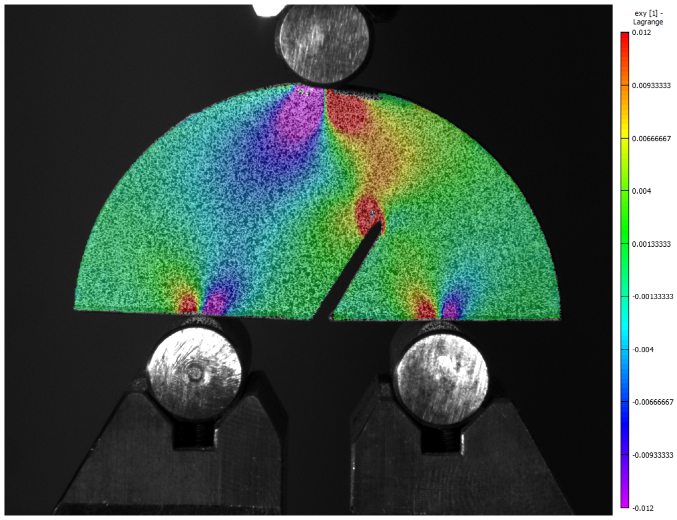

(b) Specimen 56: 30° laying red single-material SCB-specimen.

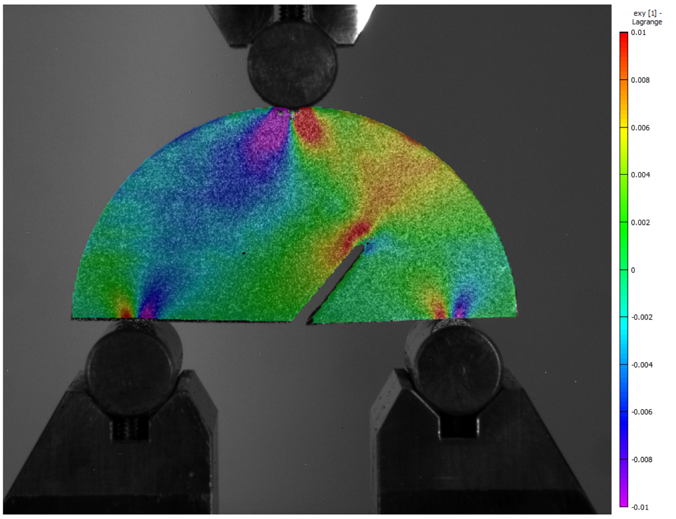

(c) Specimen 57: 40° laying red single-material SCB-specimen.

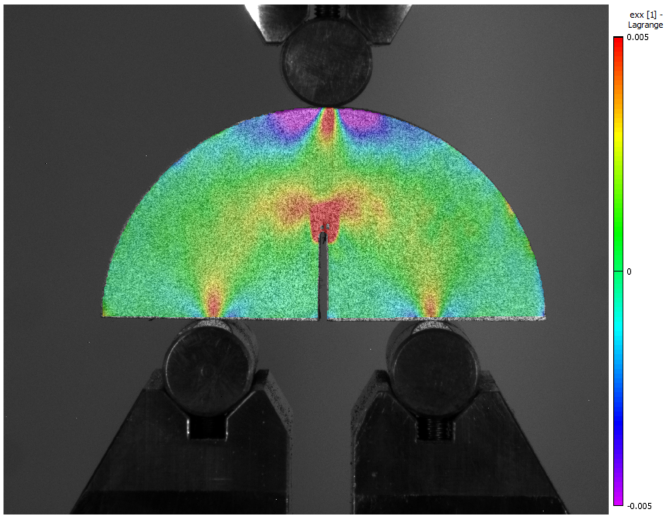

(d) Specimen 61: 0° standing bimaterial SCB-specimen.

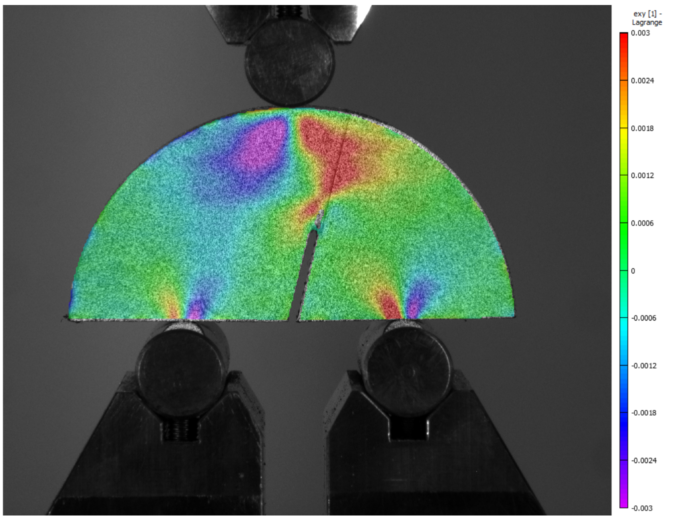

(e) Specimen 67: 15° standing bimaterial SCB-specimen with red half lower.

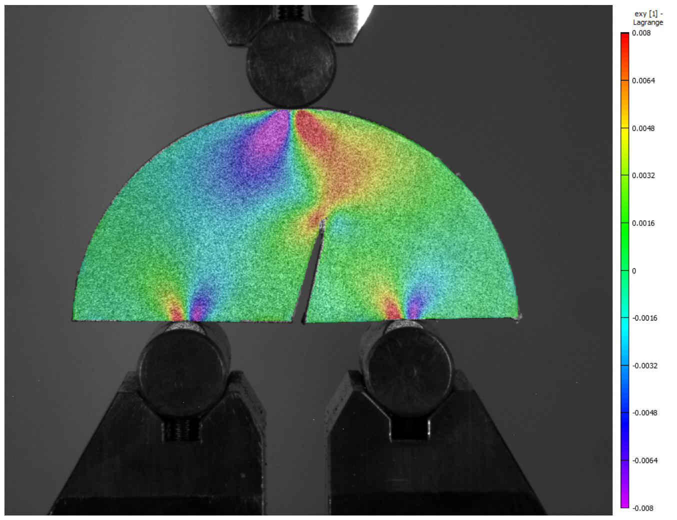

(f) Specimen 71: 15° standing bimaterial SCB-specimen with grey half lower.

Figure 47: Strain field for SCB-specimen 49, 56, 57, 61, 67 and 71.

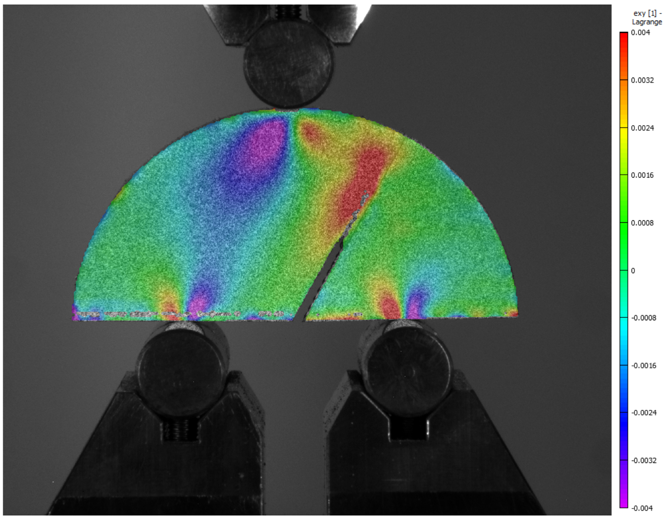

(a) Specimen 74: 30° standing bimaterial SCB-specimen with red half lower.

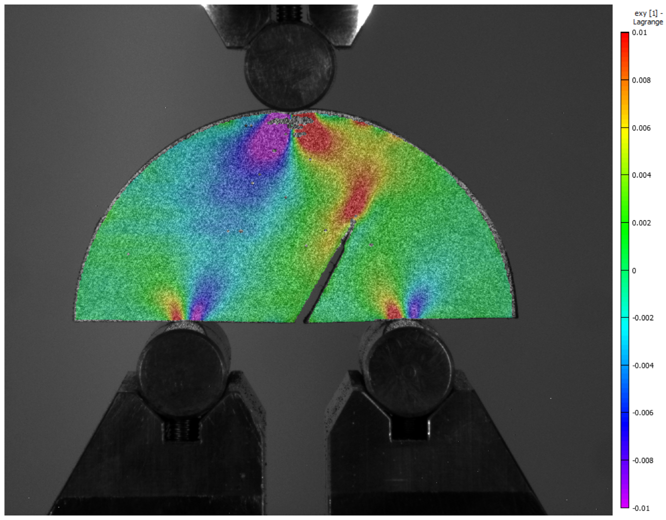

(b) Specimen 78: 30° standing bimaterial SCB-specimen with grey half lower.

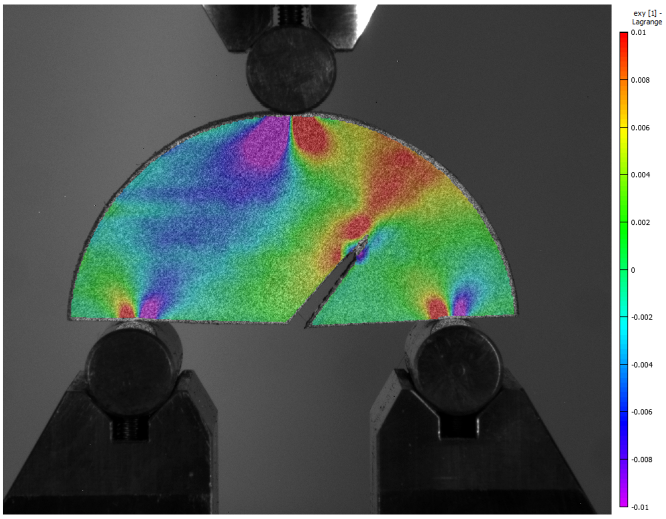

(c) Specimen 81: 40° standing bimaterial SCB-specimen with red half lower.

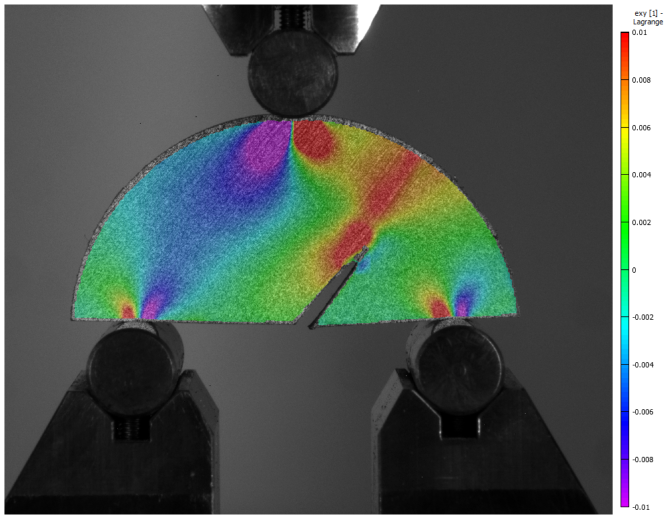

(d) Specimen 87: 40° standing bimaterial SCB-specimen with grey half lower.

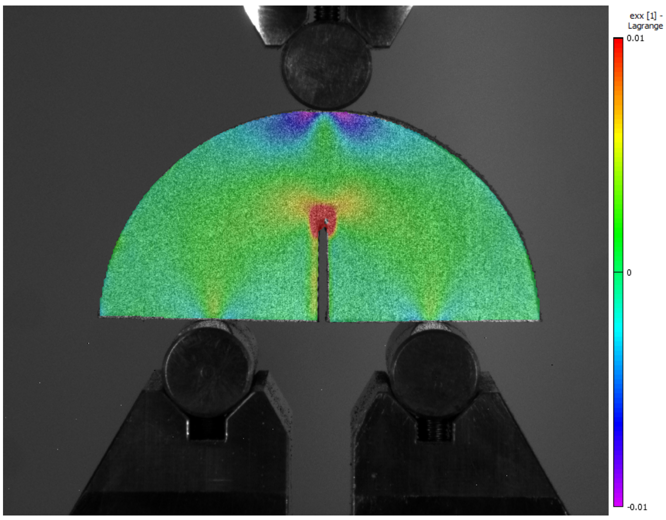

(e) Specimen 89: 0° standing grey single-material SCB-specimen.

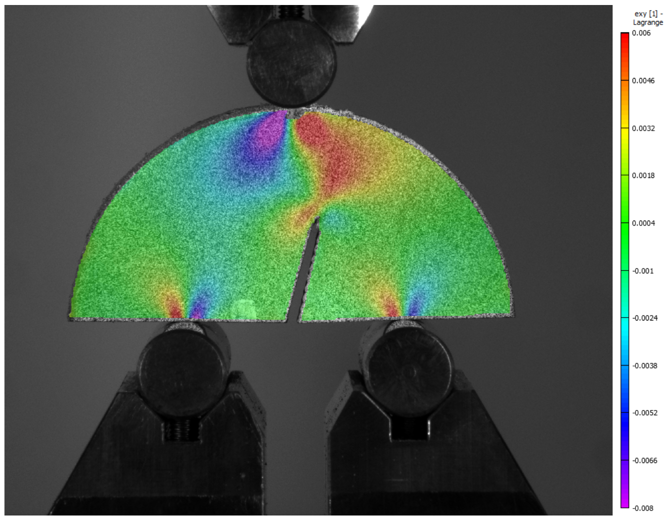

(f) Specimen 93: 15° standing grey single-material SCB-specimen.

Figure 48: Strain field for SCB-specimen 74, 78, 81, 87, 89 and 93.

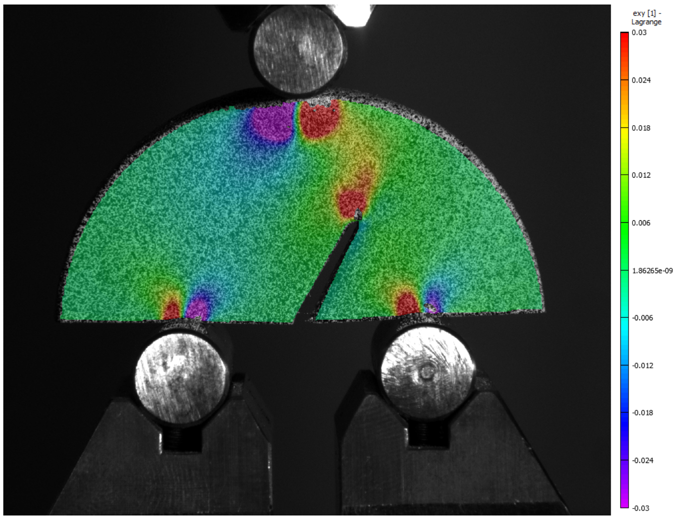

(a) Specimen 97: 30° standing grey single-material SCB-specimen.

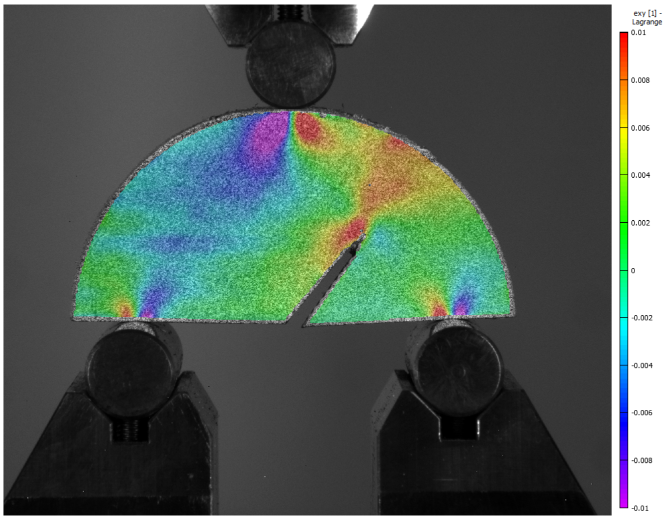

(b) Specimen 101: 40° standing grey single-material SCB-specimen.

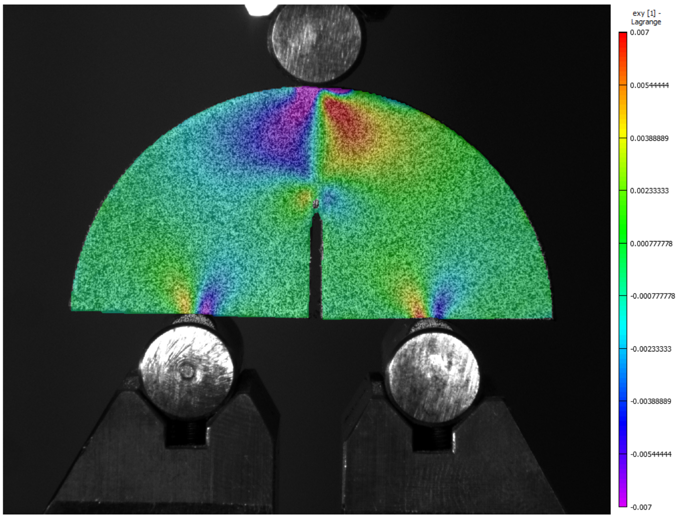

(c) Specimen 105: 0° standing red single-material SCB-specimen.

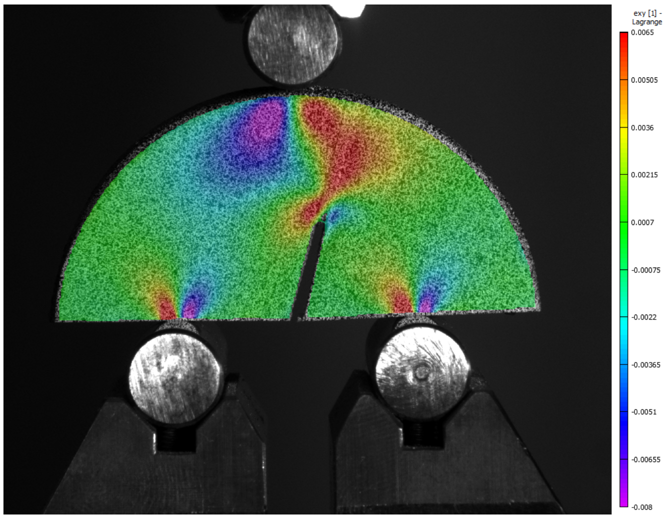

(d) Specimen 109: 15° standing red single-material SCB-specimen.

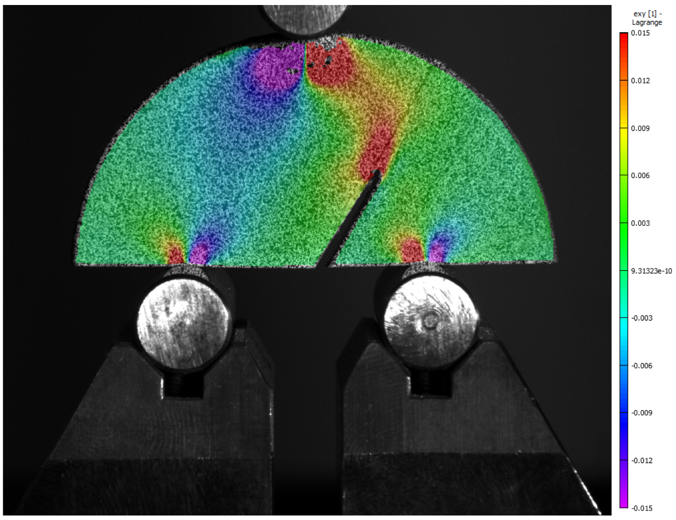

(e) Specimen 113: 30° standing red single-material SCB-specimen.

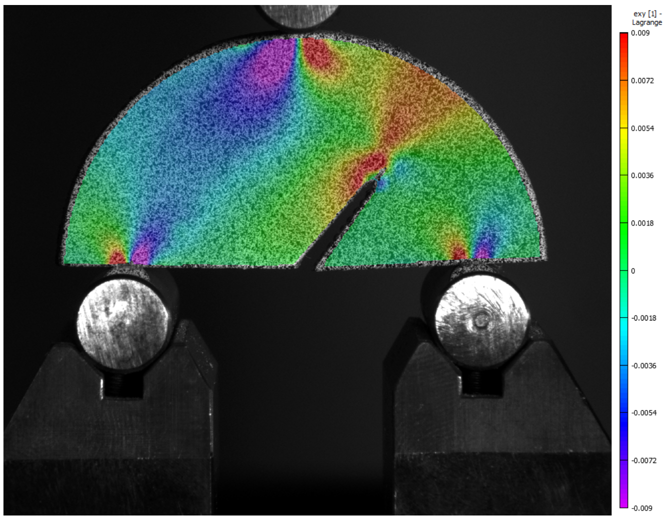

(f) Specimen 117: 40° standing red single-material SCB-specimen.

Figure 49: Strain field for SCB-specimen 97, 101, 105, 109, 113 and 117.

5.8 Fracture Path

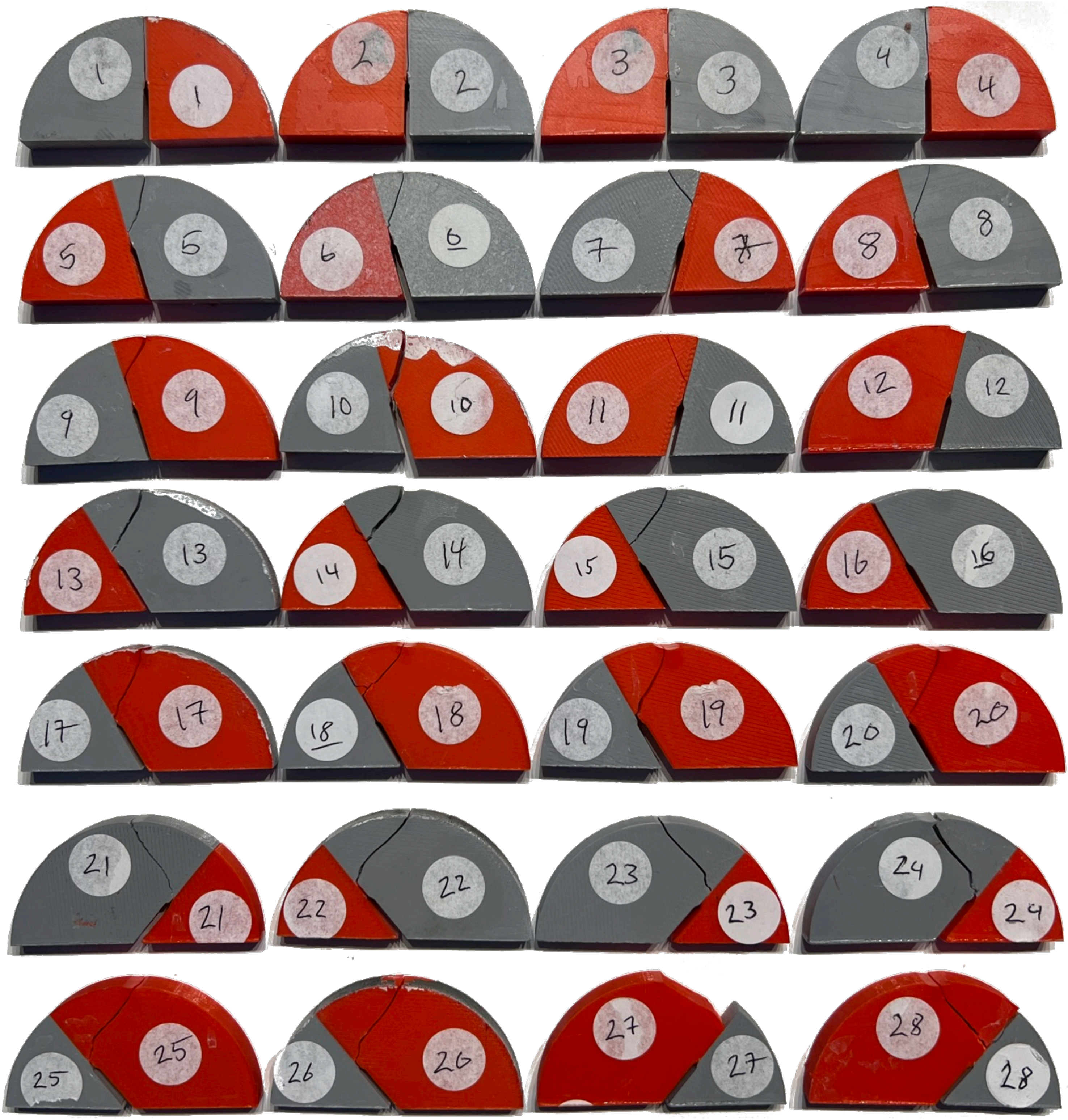

Figure 50: Crack path of laying bimaterial SCB-specimen.

Figure 51: Crack path of laying red and grey SCB-specimen.

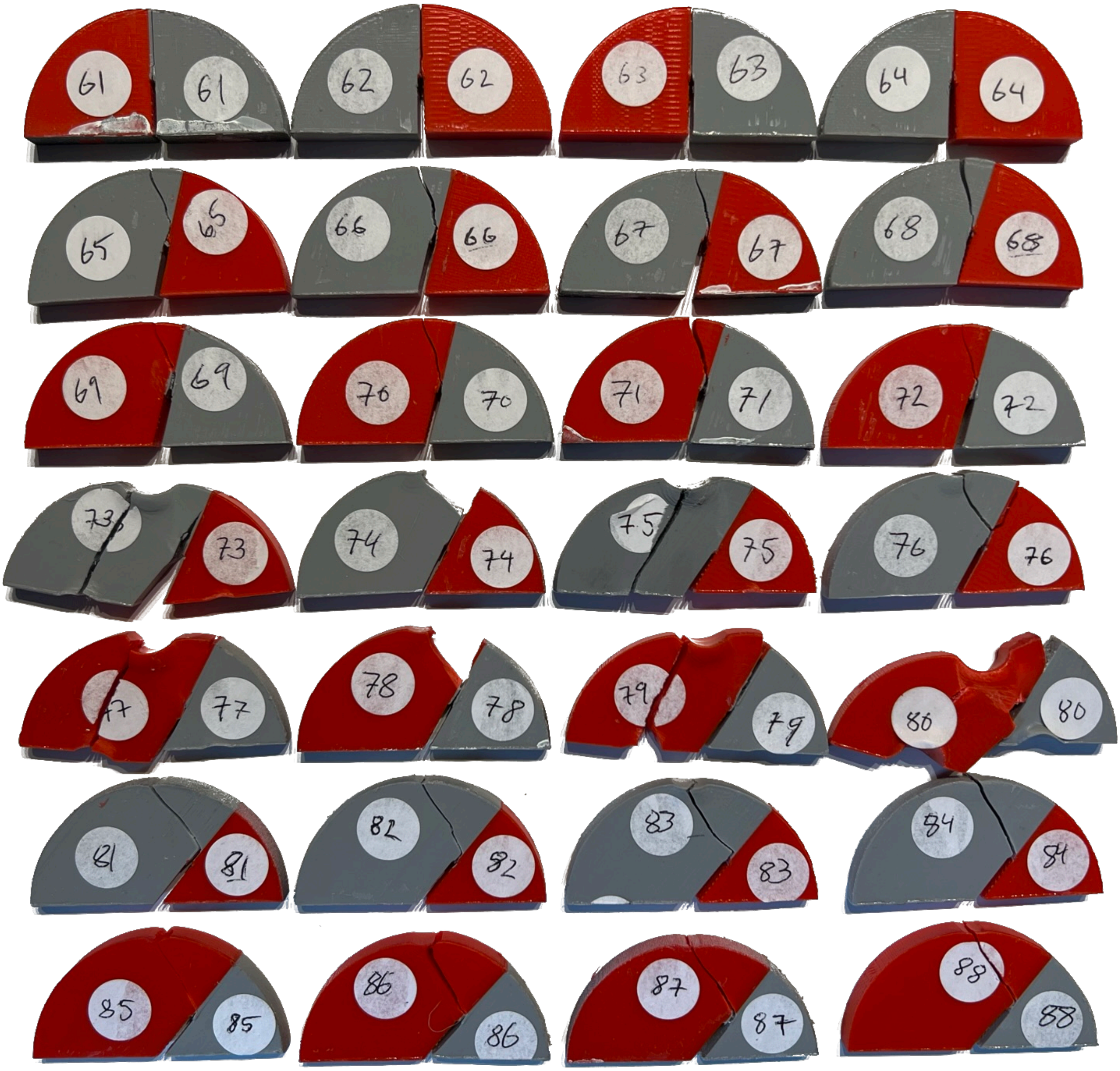

Figure 52: Crack path of standing bimaterial SCB-specimen.

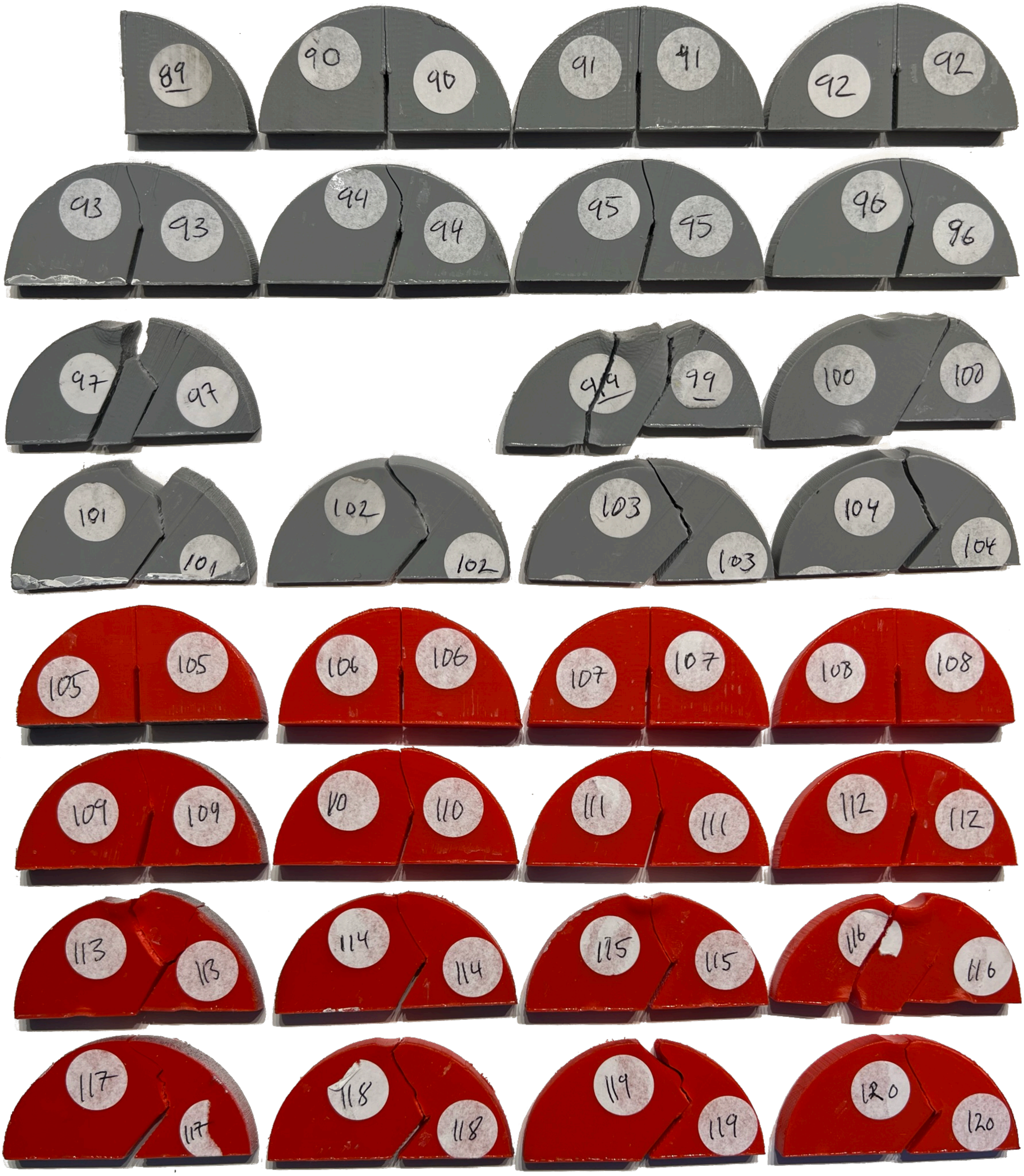

Figure 53: Crack path of standing red and grey SCB-specimen.

6 Discussion

In this section the results presented in Section 5 are evaluated and discussed.

6.1 Fracture Loads

The results in Figure 38 mostly follow the expected increase in fracture load as the mode mixity decreases, however some sample groups break the trend. Noticeably the laying grey with 0.78 M_e, laying red with 0.65 M_e and the standing red with 0.78 M_e.

When inspecting specimen 33-36 in Figure 51, it can be seen that the first section if the fracture path follows the raster angle, which is angled 45° relative to the notch direction. This is expected as the weakest part of the laying single material specimen will be along the lines of the rasters. When comparing to specimen 49-52 in Figure 51, which are the red specimen with same M_e, it follows the same path, however the fracture line is not as straight within the first section of the fracture, as compared to the grey. This indicates that the bonding in the grey rasters are weaker than the red. This is further confirmed when having a look at the fracture surface of a grey and red specimen. In the fracture surface of specimen 36 in Figure 54a it is possible to spot voids and porosity in the bottom half of the fracture surface, which is the first section if the crack. When comparing to the fracture surface of specimen 50 in Figure 54b, a denser and more even infill can be seen. The imperfections observed in the fracture surface of specimen 36 will reduce the strength of the specimen, which explains the low fracture force of the laying grey specimen with 0.78 M_e in Figure 38.

When inspecing the crack path and fracture surface of some of the specimen from the laying red with 0.65 M_e, there was no obvious indications as to what may have caused an early fracture. The fracture surfaces of specimen 58 and 60 can be seen in Figure 55. The fracture load of the laying red specimen with 0.65 M_e are similar to the fracture loads of the laying grey specimen with same mode mixity. Because of the low sample size and large spread in data for the laying red specimen with 0.78 M_e, it could be that the laying red chart would have a more linear trend had the tests been performed with a larger sample size.

Also for the standing specimen, the red specimen with 0.78 M_e is showing unexpectedly high fracture loads compared to the grey and bimaterial specimen with the same orientation and M_e.

The linear increase of fracture load as the M_e decreases is particularly obvious in the bimaterial charts. The bimaterial specimen had almost twice as many specimen tested, meaning the sample size is large. This makes any tests that stand out from the rest of the specimen have less influence in the mean fracture load.

When evaluating Figure 40 which visualises the fracture load difference between the laying and standing SCB-specimen, it can be seen that the laying specimen was stronger in a pure mode 1 load case, while the standing specimen performed

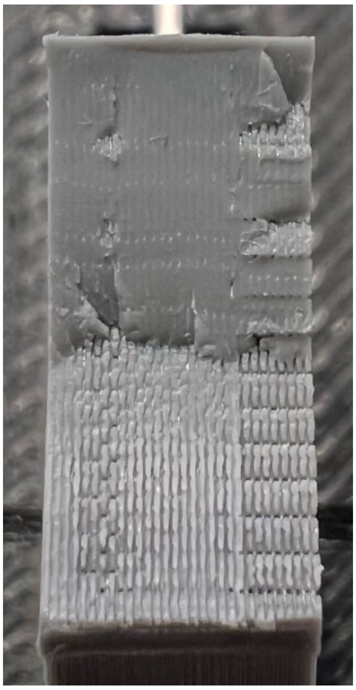

(a) Fracture surface of specimen 36.

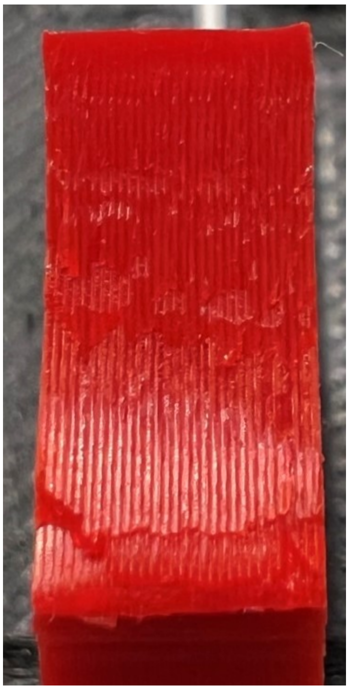

(b) Fracture surface of specimen 50.

Figure 54: Fracture surface of specimen 36 and 50.

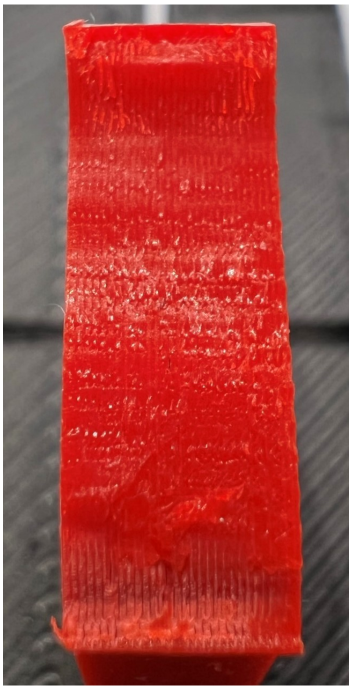

(a) Fracture surface of specimen 58.

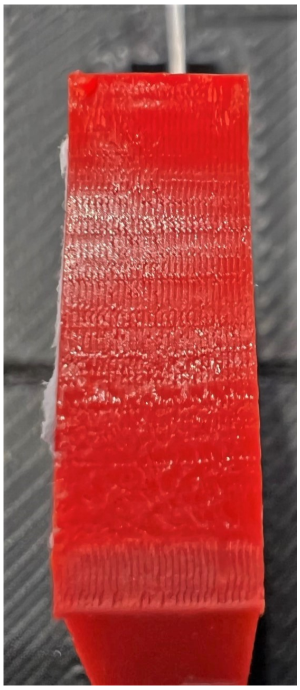

(b) Fracture surface of specimen 60.

Figure 55: Fracture surface of specimen 58 and 60.

better in almost every mixed mode loading case. As can be seen in the fracture paths in Figure 50, 51, 52 and 53, the crack almost always propagates towards the point of the top roller in cases with mixed mode loading. This means that the crack will move away from the bimaterial interface and through the infill of the specimen. As seen in the fracture surface of specimen 36 in Figure 54a, the infill of the laying samples contains defects in the rasters where the crack can propagate along, which can reduce the strength of the specimen. However for the standing specimen, the crack need to move across layers in order to move through the infill. As the crack moves normal to the printing direction, this creates obstacles for the crack which is harder to pass, making the material more fracture resistant. This is in line with results from a study by McLouth, Severino, Adams *et al.*, where the impact in fracture toughness was measured according to the direction of the layers [44]. It was shown that CT-specimen had a 53.9% increase in fracture toughness when a crack was placed perpendicular to the material layers, compared to when the crack was parallel to the material layers.

In Figure 41 it is shown that specimen with a grey lower half is consistently stronger that a equal specimen with a red lower half. As was explained in Section 4.3.3, a specimen with a ”red lower half” will have a majority of grey material, and vice versa. Since the fracture initiates at the crack tip and moves upwards towards the point where the force is applied to the specimen, the crack propagates through the grey material in a ”red half lower” specimen, and through the red material in a ”grey half lower” specimen. The results in Figure 41 could point towards the red material being the strongest. However the overview of the fracture toughness for the 6 different materials listed in Table 7 report the fracture toughness of the grey material being slighter higher than the red material. The fracture toughness values calculated in Table 7 are however determined from mode 1 fracture tests and is only off by 1.8%, which means there are unlikely to be any major difference between the two colours. On the other hand, the ultimate tensile strength of the red material was shown to be higher than the grey material in Figure 42. One aspect to also keep in mind is that the red half of the specimen was always printed as the top half of the SCB-disc. This could impact the mechanical properties of the specimen. Ultimately the small sample size of the experiment and the standard deviation of the data makes it difficult to determine if there is a consistent difference in strength between the two orientations.

6.2 Fracture Toughness

In Table 7 the experimental fracture toughness for each material can be seen. Since the geometry of all the 0° SCB-specimen were identical, the SIF remains constant for all the materials as it is geometrically defined. The discrepancy between the laying grey and red material was only 1.8%, which was expected as the print procedure and material polymer were the same. The laying bimaterial specimen were 28.3% lower than the mean single material fracture toughness. This was expected to be lower as the introduction of a bimaterial interface will weaken the structural integrity of the specimen. In Figure 56 the fracture surface of the laying bimaterial mode 1 specimen can be seen. there is residual material from the other half of the specimen on each surface, indicating good intermaterial adhesion. The premature failure is due to the parallel surfaces not being as strong as the intertwining infill of a single material specimen.

The standing grey and standing red specimen would be expected to be

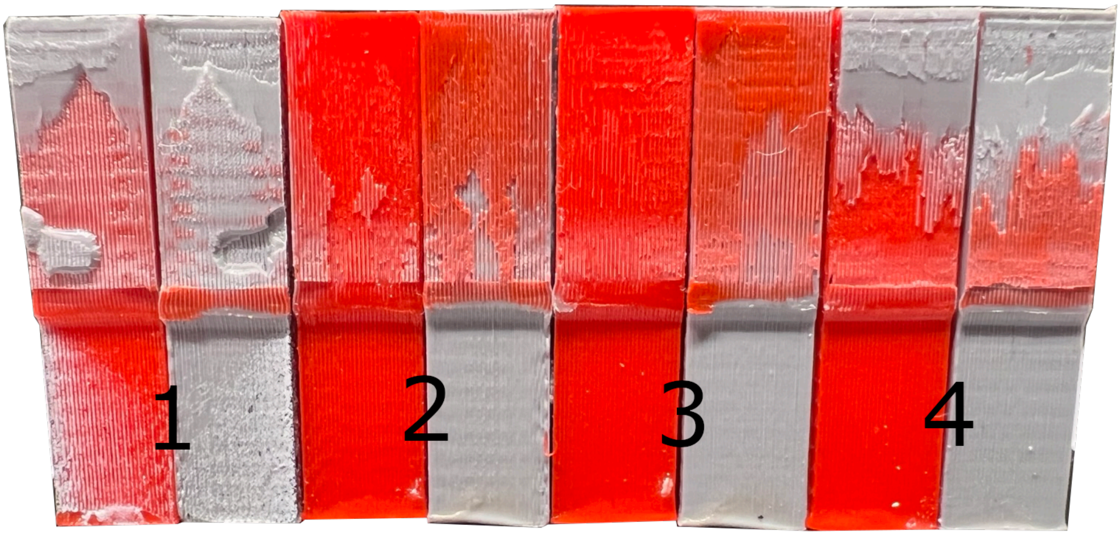

Figure 56: Fracture surface of specimen 1, 2, 3 and 4.

as close to each other as the laying single material were. However the standing grey material fractured at a 30.4% lower load than the standing grey specimen. In Figure 57 and Figure 58 the fracture surfaces of the standing grey and standing red specimen can be compared. Looking at the surfaces, there is no obvious indications as to which one would perform better. When looking at the fracture load for each specimen, which is located in the Appendix, it can be seen that two of the red specimen had significantly higher fracture load than the two other, which were closer to the grey. If the test were to be re-done with a larger sample size, this difference in fracture toughness would be lower.

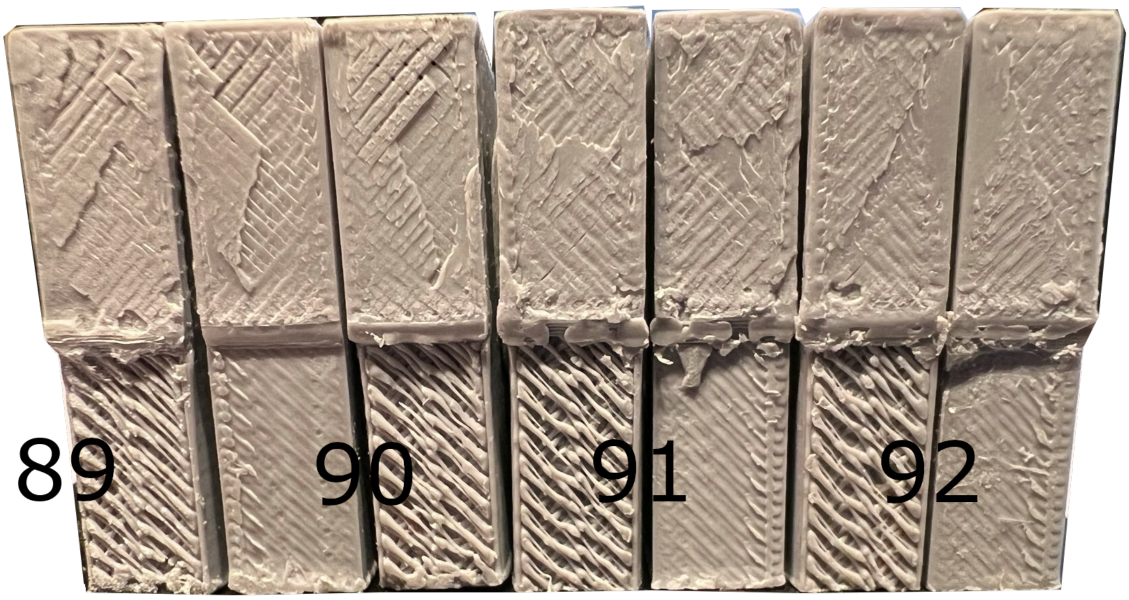

Figure 57: Fracture surface of specimen 89, 90, 91 and 92.

As there is no change in printing conditions between the standing single material and bimaterial specimen, the bi material is expected to perform about the

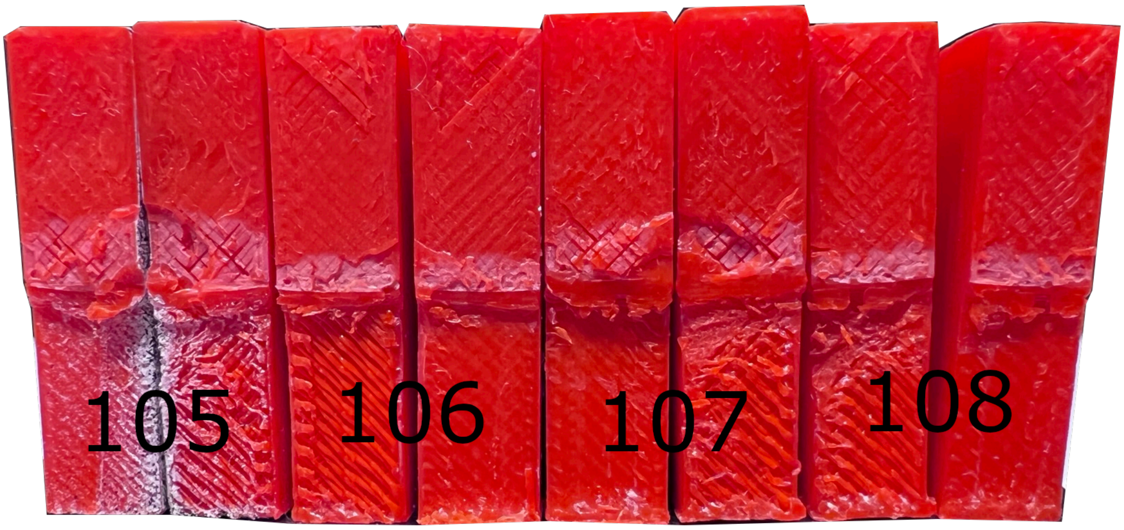

Figure 58: Fracture surface of specimen 105, 106, 107 and 108.

same as the single material specimen. Looking at the fracture surfaces in Figure 59, it can be seen that the fracture surface of the bimaterial has the same characteristics as the fracture surfaces of the single material specimen in Figure 57 and Figure 58. Specimen 61 and 63 fractured in the grey half of the specimen, indicating that the bimaterial interface was no weaker than the single material. Specimen 62 and 64 also has a good bit of residual material from the other side, indicating good cohesion. Looking at Table 7, it can be seen that although the bimaterial performed worst of the standing specimen, the bimaterial specimen were only 13.2% weaker than the standing grey specimen.

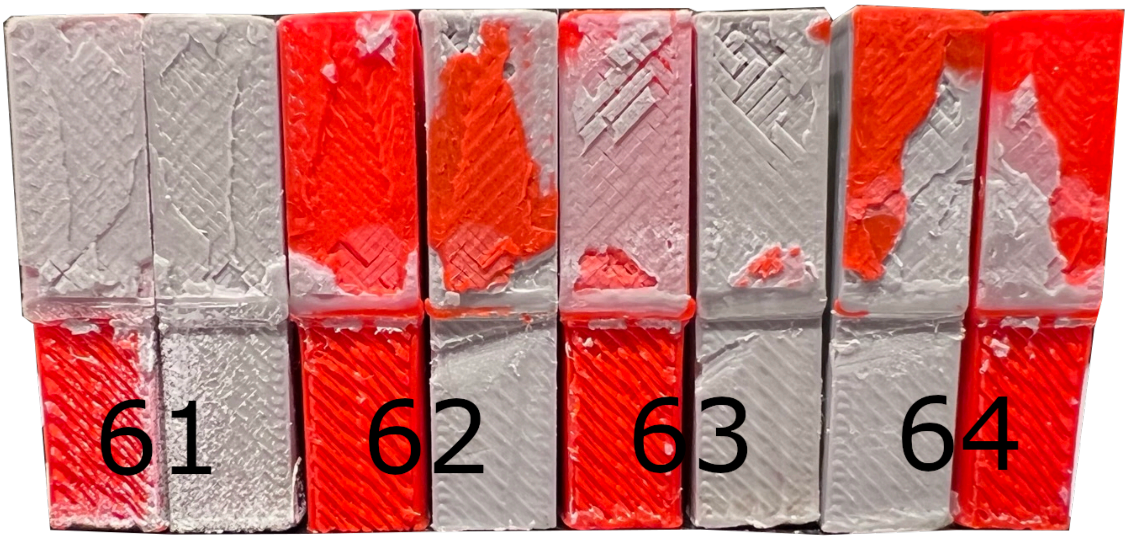

Figure 59: Fracture surface of specimen 61, 62, 63 and 64.

6.3 Fracture Prediction

In Table 8 the results from the fracture prediction are listed. Here the experimental fracture loads (P_{exp}) are the same as the results in Figure 38, which are the fracture loads of the specimen where the crack initiated at the crack tip.

The laying and standing grey and red specimen had mostly accurate predictions, except for the laying grey with 0.78 M_e. This is the same specimen which was discussed in Section 6.1, because of a lower than expected experimental fracture load due to porosity in the infill.

The ASED model is not very accurate at prediction the fracture loads of the standing specimen where M_e is lower than 1. This is partly due to the UTS was determined from tensile specimen where the quality of the specimen did not match those of the SCB-specimen. This makes the model underestimate the fracture loads of the SCB-specimen. The control radius was also calculated using a fracture toughness which was determined by specimen where the crack was placed parallel to the printed layers. As discussed in Section 6.1, the crack of the mixed mode standing specimen would have to pass through layers which were more perpendicular to the crack than in the specimen used to determine the fracture toughness.

There is room to get a more accurate fracture prediction model by getting the correct UTS from the material in the SCB-specimen and determining the fracture toughness for materials where the crack is placed perpendicular to the layers.

6.4 Mesh Sensitivity Analysis

The results of the mesh sensitivity analysis for the elastic strain energy simulations can be seen in Table 9. Here the gain in accuracy quickly flattens out with a relatively coarse mesh, leaving small gains to be made by further decreasing the mesh size. A mesh size of 0.2 was used in the simulations as it has a good accuracy without excessively long simulation times.

6.5 Material Properties

In this section the material properties gathered from the tensile tests are discussed.

6.5.1 Ultimate Tensile Strength

in Figure 42 the UTS of the different materials are displayed in both standing and laying configuration. As can be seen in the figure, the laying red have a higher UTS than the laying grey. An overview of the laying tensile specimen can be seen in Figure 60. Here, the single material specimen all fractured roughly at the same location, while the bimaterial specimen (T7, T8, T9) fractured near the material interface.

Figure 60: Overview of the laying tensile specimen after testing.

Having a look at the fracture surface of one of the laying red tensile specimen in Figure 61 it can be seen that the fracture initiated at some voids to the right side of the specimen, in the transition between the infill and the outer wall of the specimen. Otherwise the specimen has a dense cross-section. When looking at the fracture surface of a laying grey specimen in Figure 62, a severely flawed cross section can be seen with under-extrusion and voids, causing the specimen to fail at a lower load compared to the laying red specimen.

Figure 61: Fracture surface of laying red tensile specimen, T2.

The laying bimaterial specimen are expected to fail before the single material specimen, due to the abrupt transition from infill to wall, which is present in a

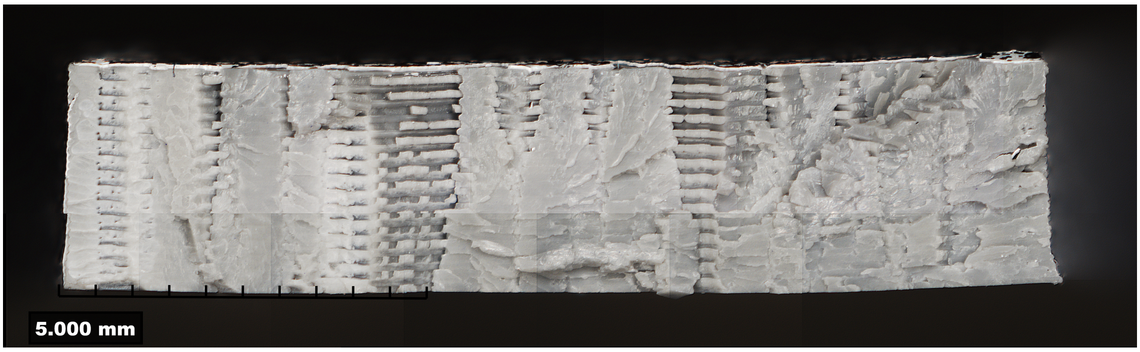

Figure 62: Fracture surface of laying grey tensile specimen, T5.

vertical material transition. The fracture surfaces of one of the bimaterial specimen can be seen in Figure 63. Here, residue from each material can be seen on each fracture surface, indicating good intermaterial adhesion. This is also reflected in the UTS of the laying bimaterial tensile specimen compared to the laying single material specimen.

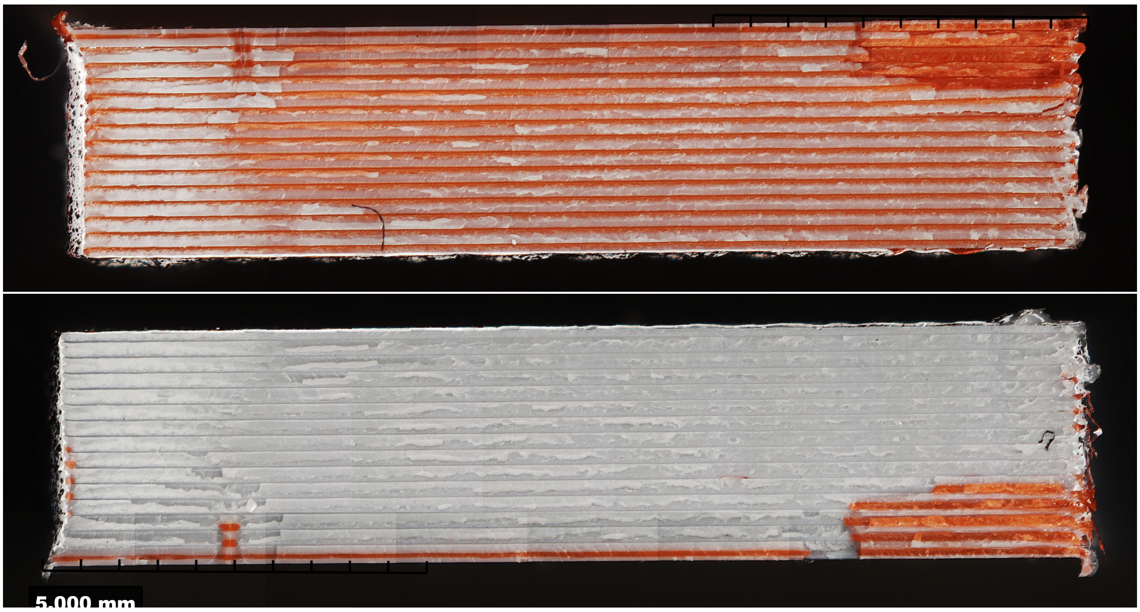

Figure 63: Fracture surfaces of laying bimaterial tensile specimen, T8.

An overview of the standing tensile specimen can be seen in Figure 64. Here, all the specimen fractured roughly at the same location, showing that the intermaterial interface is not necessarily the weakest point of a specimen.

For the standing specimen, it is the same scenario as for the laying specimen. The red material slightly outperformed the grey material. Looking at the fracture surface of a standing grey and standing red specimen in Figure 65 and Figure 66 it can be seen that the grey specimen is more under-extruded than the red specimen, causing the grey specimen to fail earlier than the red. In both of these images, the phenomenon explained in Section 4.5.5 can be seen. The printer is struggling to extrude enough material in the beginning of the printing of the infill. Since the standing specimen has a relatively low cross sectional area, this defect is extra visible. This

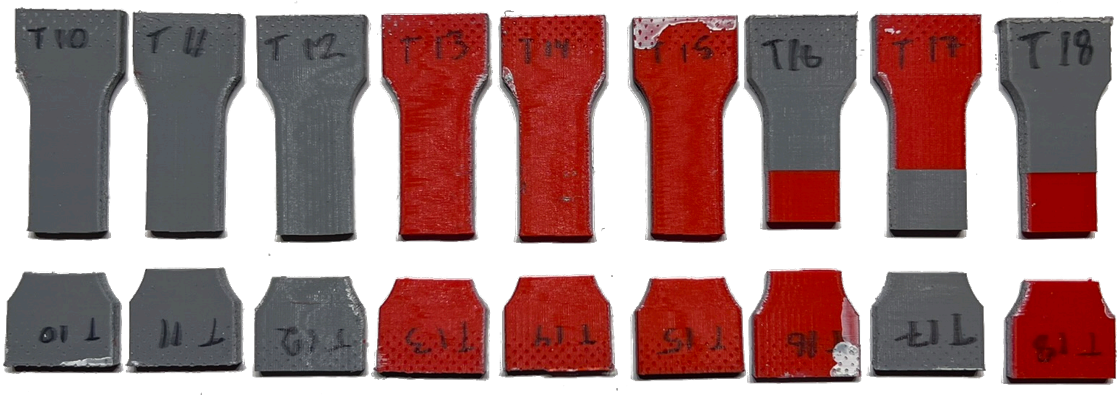

Figure 64: Overview of the standing tensile specimen after testing.

causes the specimen to fail at a lower load than expected.

Figure 65: Fracture surface of standing grey tensile specimen, T12.

Figure 66: Fracture surface of standing red tensile specimen, T14.

The specimen with the lowest UTS are the standing bimaterial tensile specimen. As showcased in Figure 67, the quality of the cross-section is the worst of all the specimen. Major under-extrusion can be seen, causing the specimen to fail at low loads. As was the case for the grey and red standing specimen, the printer is slowly building pressure, gradually increasing the material flow throughout the printing of the infill. Even tough the standing red specimen in Figure 66 and standing bimaterial specimen in Figure 67 were printed on the same day, with the same process parameters and filament, the quality of the bimaterial specimen is worse than the single material specimen. This is something that should be investigated further in future work.

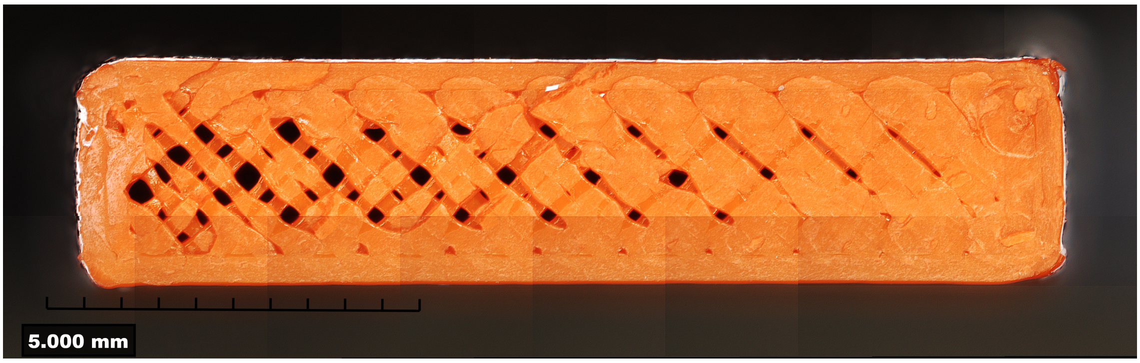

Figure 67: Fracture surface of standing bimaterial tensile specimen, T16.

6.5.2 Young's Modulus

The Young's modulus in Figure 43 for all the specimen is shown to be close to 3000MPa for all specimen except for the standing bimaterial specimen. This is because the actual cross section of the specimen is lower than expected, due to the underextrusion shown in Figure 67.

6.5.3 Poisson's Ratio

The Poisson's ratio in Figure 44 for all specimen are close to 0.3, which is expected for the material. The Poisson's ratio for the standing bimaterial specimen is again underestimated due to the under extrusion in the infill.

6.6 Strain Fields and Crack Path

The strain fields presented in Figure 45, Figure 46, Figure 47, Figure 48 and Figure 49 does a good job showcasing the surface displacement of the specimen making it possible to predict the fracture path of the crack.

7 Conclusion

In this thesis the structural integrity of additive manufactured bimaterial parts have been tested experimentally. Bimaterial semi Circular Bend specimen were tested in single and mixed mode conditions and compared to specimen made with a singular material. The specimen were printed in two orientations, laying and standing, to evaluate how the printing orientation effects the bimaterial interface. 120 SCB-specimen were manufactured and tested in total. Methods for manufacturing and preparing the SCB-specimen with high accuracy and repeatability were also developed. Finally the experimental results were compared with fracture predictions calculated using average strain energy density (ASED). The main takeaways from the thesis are summarised below:

- Bimaterial specimen applied mode I fracture load performs worse than single material specimen, while bimaterial specimen loaded with a mixed mode condition performs close to single material specimen.
- Standing mixed mode specimen are able to withstand a greater load compared to the laying specimen.
- The order which the material is printed in the standing SCB-specimen could influence the fracture toughness of the material.
- Average strain energy density has the potential of accurately predicting the fracture loads of bimaterial interfaces, given the calculations are done with material properties which accurately represents the material in use.
- Having too many specimen printed and tested at once introduces the risk of the printer losing calibration, reducing the quality of the specimen. The specimen quality has been gradually decreasing throughout the project, reducing the accuracy of the results.

7.1 Further work

In order to get more accurate data, the sample size of each specimen configuration should be increased. The maximum amount of specimen produced between printer calibration should also be reduced in order to ensure good quality of the specimen. Tensile test specimen should be manufactured at the beginning and end of the production period to evaluate the change in quality during the project.

The bimaterial standing specimen should be investigated further to see if printing order of the materials influence the material properties.

The issue with the printer struggling to extrude the correct amount of material at the beginning of an extrusion path should be investigated and fixed to increase the quality of the printed parts.

Reference list

[1] C. Vălean, L. Mar□avina, M. Mărghita□ *et al.*, 'The effect of crack insertion for FDM printed PLA materials on Mode I and Mode II fracture toughness', en, *Procedia Structural Integrity*, 1st Virtual European Conference on Fracture - VECF1, vol. 28, pp. 1134–1139, Jan. 2020, ISSN: 2452-3216. DOI: 10.1016/j.prostr.2020.11.128. [Online]. Available: https://www.sciencedirect.com/science/article/pii/S2452321620307976 (visited on 8th Jun. 2022).

[2] *The Free Beginner's Guide*, en-US. [Online]. Available: https://3dprintingindustry.com/3d-printing-basics-free-beginners-guide/ (visited on 27th Sep. 2021).

[3] S. S. Crump, 'Apparatus and method for creating three-dimensional objects', US5121329A, Jun. 1992. [Online]. Available: https://patents.google.com/patent/US5121329/en (visited on 23rd Sep. 2021).

[4] N. E. Dowling, K. Siva Prasad and R. Narayanasamy, *Mechanical behavior of materials: engineering methods for deformation, fracture, and fatigue*, eng, 4. ed., international ed. Boston, Mass.: Pearson, 2013, ISBN: 978-0-273-76455-7 978-0-13-139506-0.

[5] Twisp, *File:Fracture modes v2.svg - Wikipedia*, en. [Online]. Available: https://commons.wikimedia.org/wiki/File:Fracture_modes_v2.svg (visited on 7th Jun. 2022).

[6] *G-code - RepRap*. [Online]. Available: https://reprap.org/wiki/G-code (visited on 24th Sep. 2021).

[7] A. Dey and N. Yodo, 'A Systematic Survey of FDM Process Parameter Optimization and Their Influence on Part Characteristics', en, *Journal of Manufacturing and Materials Processing*, vol. 3, no. 3, p. 64, Sep. 2019, Number: 3 Publisher: Multidisciplinary Digital Publishing Institute. DOI: 10.3390/jmmp3030064. [Online]. Available: https://www.mdpi.com/2504-4494/3/3/64 (visited on 27th Sep. 2021).

[8] C. Ziemian, M. Sharma and S. Ziemian, 'Anisotropic Mechanical Properties of ABS Parts Fabricated by Fused Deposition Modelling', in vol. 2, Apr. 2012, ISBN: 978-953-51-0505-3. DOI: 10.5772/34233.

[9] R. J. Zaldivar, D. B. Witkin, T. McLouth, D. N. Patel, K. Schmitt and J. P. Nokes, 'Influence of processing and orientation print effects on the mechanical and thermal behavior of 3D-Printed ULTEM® 9085 Material', en, *Additive Manufacturing*, vol. 13, pp. 71–80, Jan. 2017, ISSN: 2214-8604. DOI: 10.1016/j.addma.2016.11.007. [Online]. Available: https://www.sciencedirect.com/science/article/pii/S2214860416301609 (visited on 28th Sep. 2021).

[10] D. Yadav, D. Chhabra, R. K. Gupta, A. Phogat and A. Ahlawat, 'Modeling and analysis of significant process parameters of FDM 3D printer using ANFIS', en, *Materials Today: Proceedings*, International Conference on Mechanical and Energy Technologies, vol. 21, pp. 1592–1604, Jan. 2020, ISSN: 2214-7853. DOI: 10.1016/j.matpr.2019.11.227. [Online]. Available: https://www.sciencedirect.com/science/article/pii/S2214785319339136 (visited on 28th Sep. 2021).

[11] W. Jo, O.-C. Kwon and M.-W. Moon, ‘Investigation of influence of heat treatment on mechanical strength of FDM printed 3D objects’, *Rapid Prototyping Journal*, vol. 24, no. 3, pp. 637–644, Jan. 2018, Publisher: Emerald Publishing Limited, ISSN: 1355-2546. DOI: 10.1108/RPJ-06-2017-0131. [Online]. Available: https://doi.org/10.1108/RPJ-06-2017-0131 (visited on 28th Sep. 2021).

[12] T.-M. Wang, J.-T. Xi and Y. Jin, ‘A model research for prototype warp deformation in the FDM process’, en, *The International Journal of Advanced Manufacturing Technology*, vol. 33, no. 11, pp. 1087–1096, Aug. 2007, ISSN: 1433-3015. DOI: 10.1007/s00170-006-0556-9. [Online]. Available: https://doi.org/10.1007/s00170-006-0556-9 (visited on 28th Sep. 2021).

[13] T. Alani, F. Othman and H. Ali, ‘Effect of infill Parameter on compression property in FDM Process’, *Int. Journal of Engineering Research and Application*, vol. 7, pp. 2248–962 216, Oct. 2017. DOI: 10.9790/9622-0710021619. [Online]. Available: https://www.researchgate.net/publication/320335445_Effect_of_infill_Parameter_on_compression_property_in_FDM_Process.

[14] A. Pandžić, D. Hodzic and A. Milovanović, ‘EFFECT OF INFILL TYPE AND DENSITY ON TENSILE PROPERTIES OF PLA MATERIAL FOR FDM PROCESS’, Oct. 2019. DOI: 10.2507/30th.daaam.proceedings.074.

[15] O. Luzanin, D. Movrin and M. Plancak, ‘Effect of layer thickness, deposition angle, and infill on maximum flexural force in FDM-built specimens’, *Journal for Technology of Plasticity*, vol. 39, Jan. 2014.

[16] W. Wu, P. Geng, G. Li, D. Zhao, H. Zhang and J. Zhao, ‘Influence of Layer Thickness and Raster Angle on the Mechanical Properties of 3D-Printed PEEK and a Comparative Mechanical Study between PEEK and ABS’, en, *Materials*, vol. 8, no. 9, pp. 5834–5846, Sep. 2015, Number: 9 Publisher: Multidisciplinary Digital Publishing Institute. DOI: 10.3390/ma8095271. [Online]. Available: https://www.mdpi.com/1996-1944/8/9/5271 (visited on 29th Sep. 2021).

[17] S. R. Rajpurohit and H. K. Dave, ‘Effect of process parameters on tensile strength of FDM printed PLA part’, *Rapid Prototyping Journal*, vol. 24, no. 8, pp. 1317–1324, Jan. 2018, Publisher: Emerald Publishing Limited, ISSN: 1355-2546. DOI: 10.1108/RPJ-06-2017-0134. [Online]. Available: https://doi.org/10.1108/RPJ-06-2017-0134 (visited on 29th Sep. 2021).

[18] R. Polák, F. Sedláček and K. Raz, ‘Determination of FDM Printer Settings with Regard to Geometrical Accuracy’, in Jan. 2017, pp. 0561–0566, ISBN: 978-3-902734-11-2. DOI: 10.2507/28th.daaam.proceedings.079.

[19] R. Hashemi Sanatgar, C. Campagne and V. Nierstrasz, ‘Investigation of the adhesion properties of direct 3D printing of polymers and nanocomposites on textiles: Effect of FDM printing process parameters’, en, *Applied Surface Science*, vol. 403, pp. 551–563, May 2017, ISSN: 0169-4332. DOI: 10.1016/j.apsusc.2017.01.112. [Online]. Available: https://www.sciencedirect.com/science/article/pii/S0169433217301137 (visited on 29th Sep. 2021).

[20] T.-C. Yang and C.-H. Yeh, 'Morphology and Mechanical Properties of 3D Printed Wood Fiber/Polylactic Acid Composite Parts Using Fused Deposition Modeling (FDM): The Effects of Printing Speed', en, *Polymers*, vol. 12, no. 6, p. 1334, Jun. 2020, Number: 6 Publisher: Multidisciplinary Digital Publishing Institute. DOI: 10.3390/polym12061334. [Online]. Available: https://www.mdpi.com/2073-4360/12/6/1334 (visited on 29th Sep. 2021).

[21] K. J. Christiyan, U. Chandrasekhar and K. Venkateswarlu, 'A study on the influence of process parameters on the Mechanical Properties of 3D printed ABS composite', en, *IOP Conference Series: Materials Science and Engineering*, vol. 114, p. 012 109, Feb. 2016, ISSN: 1757-8981, 1757-899X. DOI: 10.1088/1757-899X/114/1/012109. [Online]. Available: https://iopscience.iop.org/article/10.1088/1757-899X/114/1/012109 (visited on 30th Sep. 2021).

[22] I. Buj-Corral, A. Bagheri, A. Domínguez-Fernández and R. Casado-López, 'Influence of infill and nozzle diameter on porosity of FDM printed parts with rectilinear grid pattern', en, *Procedia Manufacturing*, 8th Manufacturing Engineering Society International Conference, MESIC 2019, 19-21 June 2019, Madrid, Spain, vol. 41, pp. 288–295, Jan. 2019, ISSN: 2351-9789. DOI: 10.1016/j.promfg.2019.09.011. [Online]. Available: https://www.sciencedirect.com/science/article/pii/S2351978919310984 (visited on 30th Sep. 2021).

[23] L. Yang, S. Li, Y. Li, M. Yang and Q. Yuan, 'Experimental Investigations for Optimizing the Extrusion Parameters on FDM PLA Printed Parts', en, *Journal of Materials Engineering and Performance*, vol. 28, no. 1, pp. 169–182, Jan. 2019, ISSN: 1059-9495, 1544-1024. DOI: 10.1007/s11665-018-3784-x. [Online]. Available: http://link.springer.com/10.1007/s11665-018-3784-x (visited on 30th Sep. 2021).

[24] *PLA Safety Sheet*, Sep. 2018. [Online]. Available: https://prusament.com/media/2018/09/PLA_safetysheet.pdf (visited on 30th Sep. 2021).

[25] *PEEK material: High-Performance 3D printing material*, en-US. [Online]. Available: https://tractus3d.com/materials/peek/ (visited on 30th Sep. 2021).

[26] H. Kim, E. Park, S. Kim, B. Park, N. Kim and S. Lee, 'Experimental Study on Mechanical Properties of Single- and Dual-material 3D Printed Products', en, *Procedia Manufacturing*, 45th SME North American Manufacturing Research Conference, NAMRC 45, LA, USA, vol. 10, pp. 887–897, Jan. 2017, ISSN: 2351-9789. DOI: 10.1016/j.promfg.2017.07.076. [Online]. Available: https://www.sciencedirect.com/science/article/pii/S2351978917302585 (visited on 14th Sep. 2021).

[27] F. Roger and P. Krawczak, '3D-printing of thermoplastic structures by FDM using heterogeneous infill and multi-materials: An integrated design-advanced manufacturing approach for factories of the future', Aug. 2015.

[28] K. Wang, Y.-H. Chang, Y. Chen, C. Zhang and B. Wang, 'Designable dual-material auxetic metamaterials using three-dimensional printing', en, *Materials & Design*, vol. 67, pp. 159–164, Feb. 2015, ISSN: 0261-3069. DOI: 10.1016/j.matdes.2014.11.033. [Online]. Available: https://www.sciencedirect.com/science/article/pii/S0261306914009546 (visited on 14th Sep. 2021).

[29] robin.materese@nist.gov, *What Are Imaging Phantoms?*, en, text, Last Modified: 2020-09-29T16:45-04:00, Apr. 2018. [Online]. Available: https://www.nist.gov/topics/physics/what-are-imaging-phantoms (visited on 16th Sep. 2021).

[30] K. Wang, C. Wu, Z. Qian, C. Zhang, B. Wang and M. A. Vannan, 'Dual-material 3D printed metamaterials with tunable mechanical properties for patient-specific tissue-mimicking phantoms', en, *Additive Manufacturing*, vol. 12, pp. 31–37, Oct. 2016, ISSN: 2214-8604. DOI: 10.1016/j.addma.2016.06.006. [Online]. Available: https://www.sciencedirect.com/science/article/pii/S221486041630118X (visited on 16th Sep. 2021).

[31] L. R. Lopes, A. F. Silva and O. S. Carneiro, 'Multi-material 3D printing: The relevance of materials affinity on the boundary interface performance', en, *Additive Manufacturing*, vol. 23, pp. 45–52, Oct. 2018, ISSN: 2214-8604. DOI: 10.1016/j.addma.2018.06.027. [Online]. Available: https://www.sciencedirect.com/science/article/pii/S2214860418301544 (visited on 17th Sep. 2021).

[32] M. J. Mirzaali, A. Herranz de la Nava, D. Gunashekar *et al.*, 'Mechanics of bioinspired functionally graded soft-hard composites made by multi-material 3D printing', en, *Composite Structures*, vol. 237, p. 111 867, Apr. 2020, ISSN: 0263-8223. DOI: 10.1016/j.compstruct.2020.111867. [Online]. Available: https://www.sciencedirect.com/science/article/pii/S0263822319309778 (visited on 21st Sep. 2021).

[33] *Creatbot F series 1.75mm Full Metal Hotend Heat Brake Tube*, en-US. [Online]. Available: https://3dprintingservices.co.nz/product/creatbot-f-series-1-75mm-full-metal-hotend-heat-brake-tube/ (visited on 16th Dec. 2021).

[34] 3DNet, *3DNet PLA 1.75*, nb. [Online]. Available: https://3dnet.no/products/3dnet-pla-1-75-ny (visited on 7th Dec. 2021).

[35] *Ultimate 3D Printing Material Properties Table*, en-US. [Online]. Available: https://www.simplify3d.com/support/materials-guide/properties-table/ (visited on 7th Dec. 2021).

[36] K. Hibbert, G. Warner, C. Brown, O. Ajide, G. Owolabi and A. Azimi, 'The Effects of Build Parameters and Strain Rate on the Mechanical Properties of FDM 3D-Printed Acrylonitrile Butadiene Styrene', *Open Journal of Organic Polymer Materials*, vol. 09, pp. 1–27, Jan. 2019. DOI: 10.4236/ojopm.2019.91001.

[37] *Dimafix – Specific Fixative For 3D Printing*, es. [Online]. Available: https://dimafix.com/ (visited on 15th Dec. 2021).

[38] 5axes, *Package - Ultimaker Cura Marketplace*. [Online]. Available: https://marketplace.ultimaker.com/app/cura/plugins/5axes/CalibrationShapes (visited on 7th Dec. 2021).

[39] C. Fox, *What Is Face Milling and Why Should You Bother?*, en. [Online]. Available: https://blog.tormach.com/face-milling-bother (visited on 20th May 2022).

[40] *Top 8 Milling Tools for CNC Cutting*, en, Jun. 2018. [Online]. Available: https://www.autodesk.com/products/fusion-360/blog/top-8-milling-tools-new-cnc-machinists/ (visited on 20th May 2022).

[41] *Reserveblad | Clas Ohlson*. [Online]. Available: https://www.clasohlson.com/no/Reserveblad/p/30-6850 (visited on 24th May 2022).

[42] S. Razavi, M. Aliha and F. Berto, ‘Application of an average strain energy density criterion to obtain the mixed mode fracture load of granite rock tested with the cracked asymmetric four-point bend specimens’, en, *Theoretical and Applied Fracture Mechanics*, vol. 97, pp. 419–425, Oct. 2018, ISSN: 01678442. DOI: 10.1016/j.tafmec.2017.07.004. [Online]. Available: https://linkinghub.elsevier.com/retrieve/pii/S0167844217302422 (visited on 26th May 2022).

[43] F. Berto and P. Lazzarin, ‘A review of the volume-based strain energy density approach applied to V-notches and welded structures’, en, *Theoretical and Applied Fracture Mechanics*, vol. 52, no. 3, pp. 183–194, Dec. 2009, ISSN: 01678442. DOI: 10.1016/j.tafmec.2009.10.001. [Online]. Available: https://linkinghub.elsevier.com/retrieve/pii/S0167844209001050 (visited on 1st Jun. 2022).

[44] T. D. McLouth, J. V. Severino, P. M. Adams, D. N. Patel and R. J. Zaldivar, ‘The impact of print orientation and raster pattern on fracture toughness in additively manufactured ABS’, en, *Additive Manufacturing*, vol. 18, pp. 103–109, Dec. 2017, ISSN: 22148604. DOI: 10.1016/j.addma.2017.09.003. [Online]. Available: https://linkinghub.elsevier.com/retrieve/pii/S2214860417301781 (visited on 9th Jun. 2022).

Appendix

A Cura Settings Nozzle 1

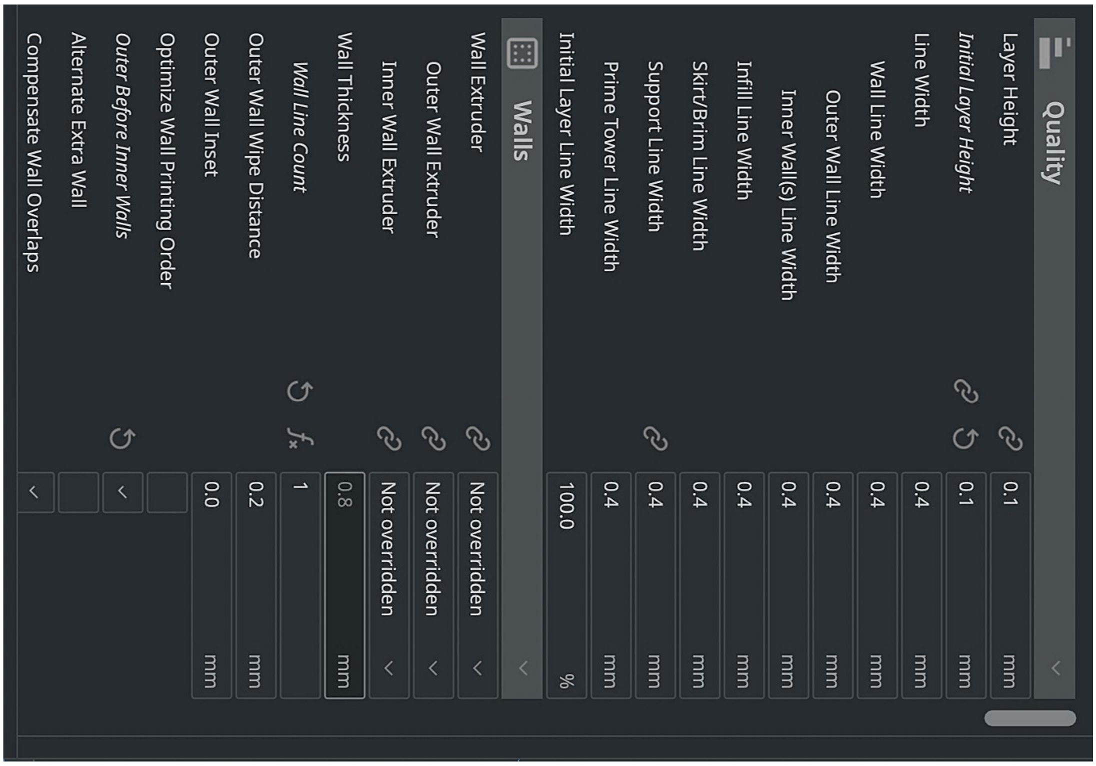

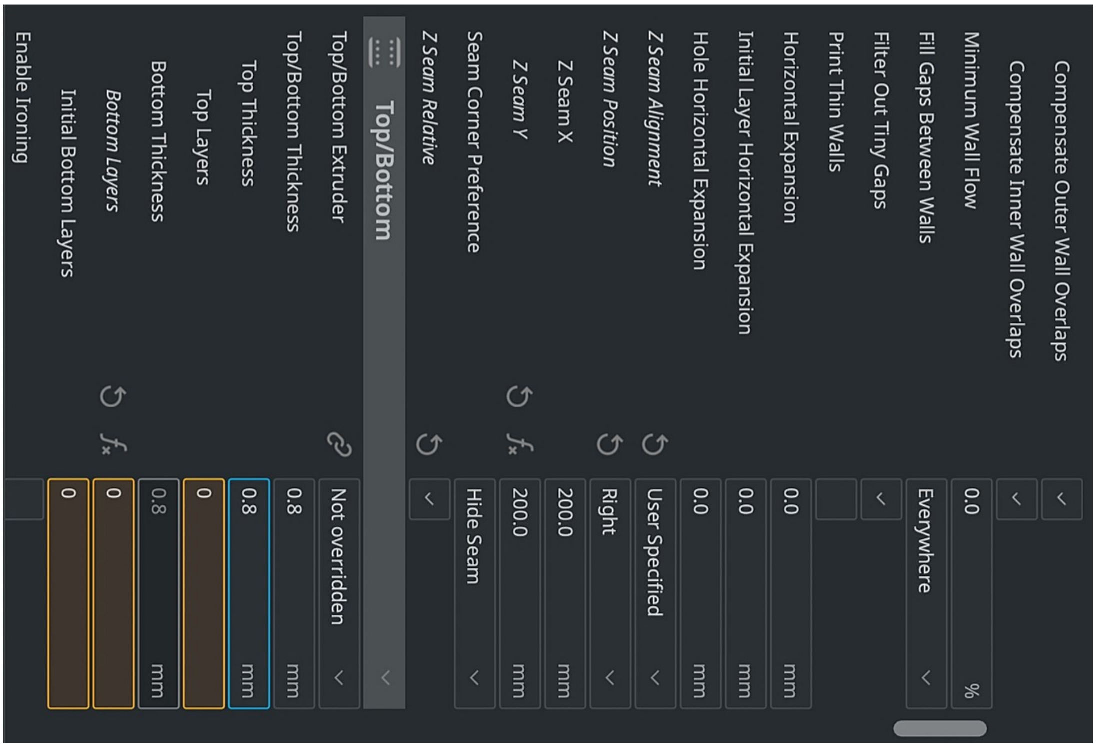

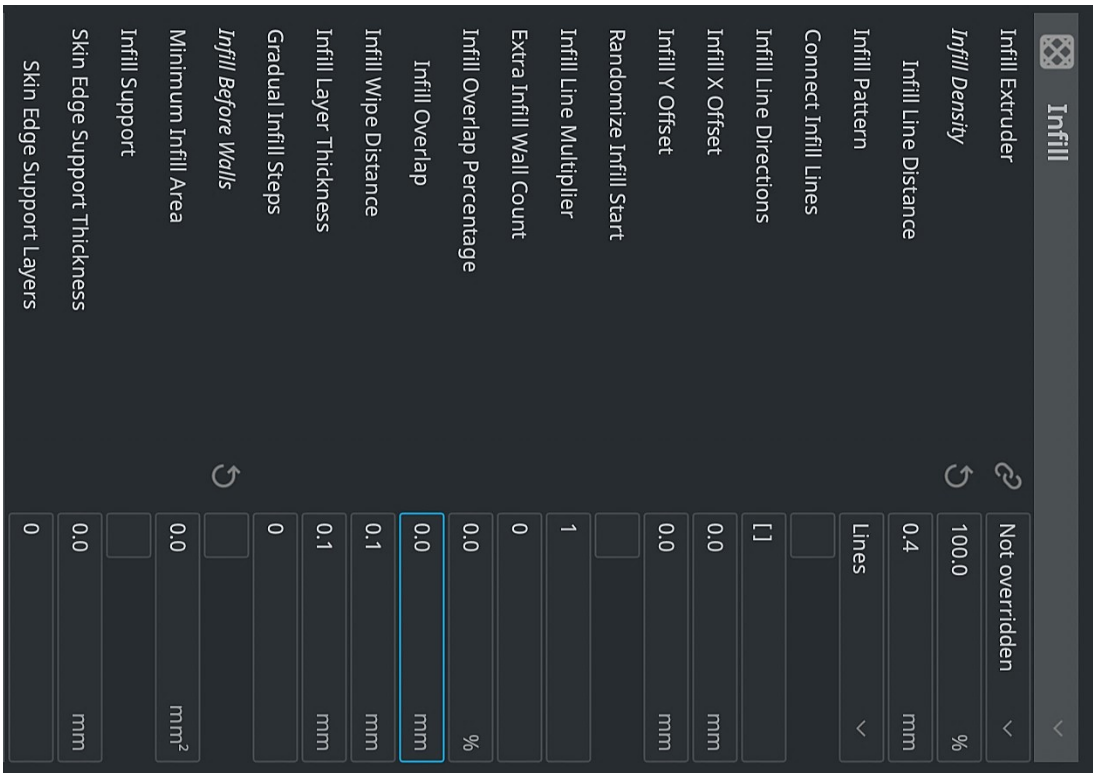
Infill
Infill Extruder
Not overridden
Infill Density
100.0 %
Infill Line Distance
0.4 mm
Infill Pattern
Lines
Connect Infill Lines
Infill Line Directions
[]
Infill X Offset
0.0 mm
Infill Y Offset
0.0 mm
Randomize Infill Start
Infill Line Multiplier
1
Extra Infill Wall Count
0
Infill Overlap Percentage
0.0 %
Infill Overlap
0.0 mm
Infill Wipe Distance
0.1 mm
Infill Layer Thickness
0.1 mm
Gradual Infill Steps
0
Infill Before Walls
Minimum Infill Area
0.0 mm²
Infill Support
Skin Edge Support Thickness
0.0 mm
Skin Edge Support Layers
0

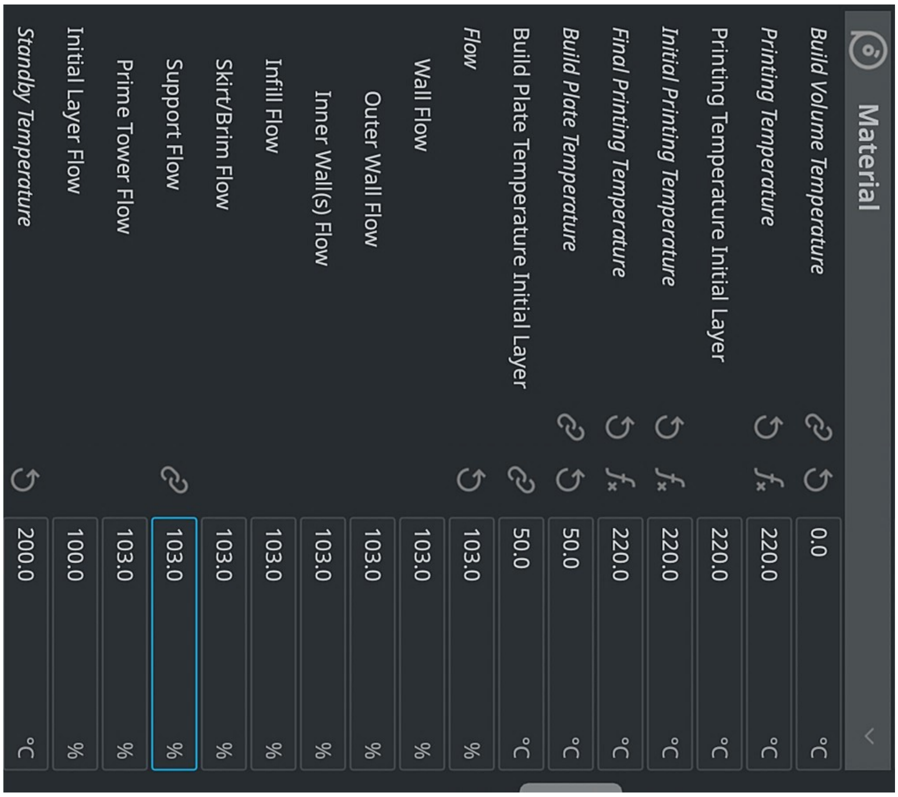
Material
Build Volume Temperature
0.0 °C
Printing Temperature
220.0 °C
Printing Temperature Initial Layer
220.0 °C
Initial Printing Temperature
220.0 °C
Final Printing Temperature
220.0 °C
Build Plate Temperature
50.0 °C
Build Plate Temperature Initial Layer
50.0 °C
Flow
103.0 %
Wall Flow
103.0 %
Outer Wall Flow
103.0 %
Inner Wall(s) Flow
103.0 %
Infill Flow
103.0 %
Skirt/Brim Flow
103.0 %
Support Flow
103.0 %
Prime Tower Flow
103.0 %
Initial Layer Flow
100.0 %
Standby Temperature
200.0 °C

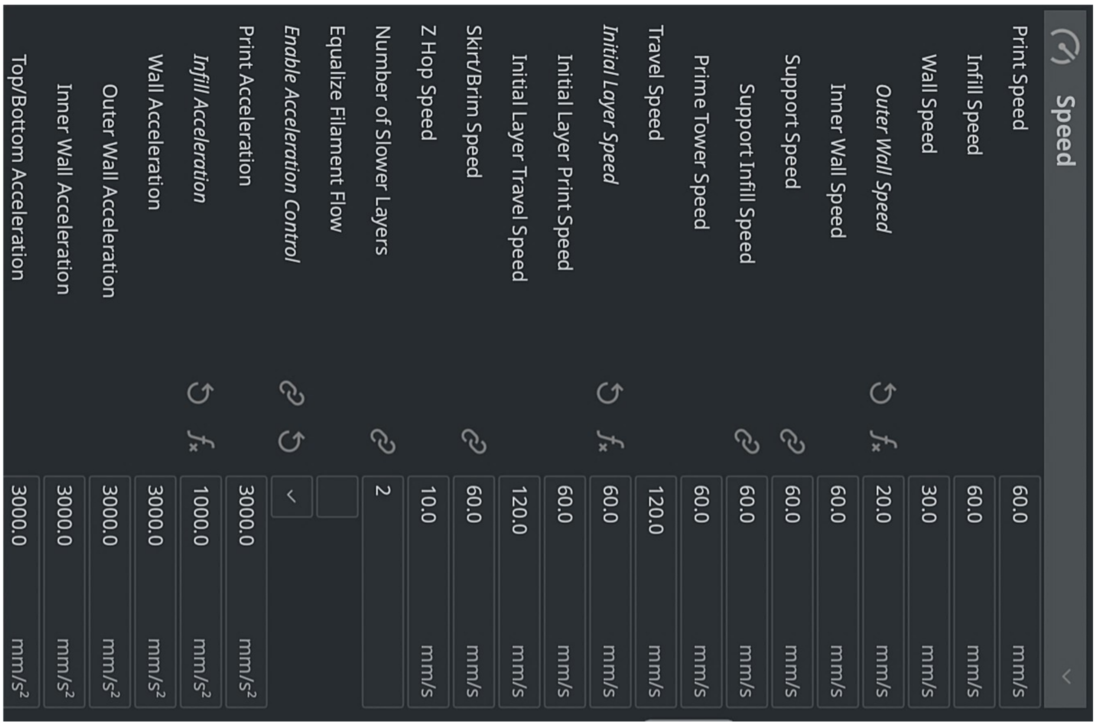
Speed
Print Speed 60.0 mm/s
Infill Speed 60.0 mm/s
Wall Speed 30.0 mm/s
Outer Wall Speed 20.0 mm/s
Inner Wall Speed 60.0 mm/s
Support Speed 60.0 mm/s
Support Infill Speed 60.0 mm/s
Prime Tower Speed 60.0 mm/s
Travel Speed 120.0 mm/s
Initial Layer Speed 60.0 mm/s
Initial Layer Print Speed 60.0 mm/s
Initial Layer Travel Speed 120.0 mm/s
Skirt/Brim Speed 60.0 mm/s
Z Hop Speed 10.0 mm/s
Number of Slower Layers 2
Equalize Filament Flow
Enable Acceleration Control
Print Acceleration 3000.0 mm/s²
Infill Acceleration 1000.0 mm/s²
Wall Acceleration 3000.0 mm/s²
Outer Wall Acceleration 3000.0 mm/s²
Inner Wall Acceleration 3000.0 mm/s²
Top/Bottom Acceleration 3000.0 mm/s²

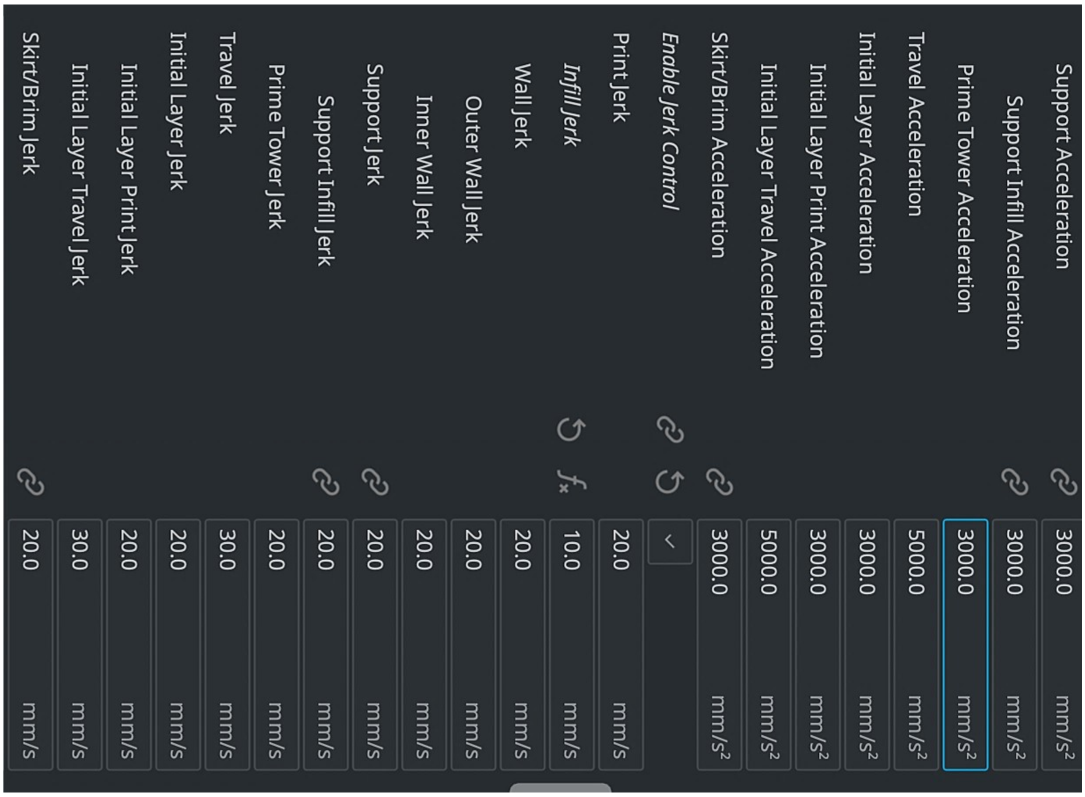
Support Acceleration 3000.0 mm/s²
Support Infill Acceleration 3000.0 mm/s²
Prime Tower Acceleration 3000.0 mm/s²
Travel Acceleration 5000.0 mm/s²
Initial Layer Acceleration 3000.0 mm/s²
Initial Layer Print Acceleration 3000.0 mm/s²
Initial Layer Travel Acceleration 5000.0 mm/s²
Skirt/Brim Acceleration 3000.0 mm/s²
Enable Jerk Control
Print Jerk 20.0 mm/s
Infill Jerk 10.0 mm/s
Wall Jerk 20.0 mm/s
Outer Wall Jerk 20.0 mm/s
Inner Wall Jerk 20.0 mm/s
Support Jerk 20.0 mm/s
Support Infill Jerk 20.0 mm/s
Prime Tower Jerk 20.0 mm/s
Travel Jerk 30.0 mm/s
Initial Layer Jerk 20.0 mm/s
Initial Layer Print Jerk 20.0 mm/s
Initial Layer Travel Jerk 30.0 mm/s
Skirt/Brim Jerk 20.0 mm/s

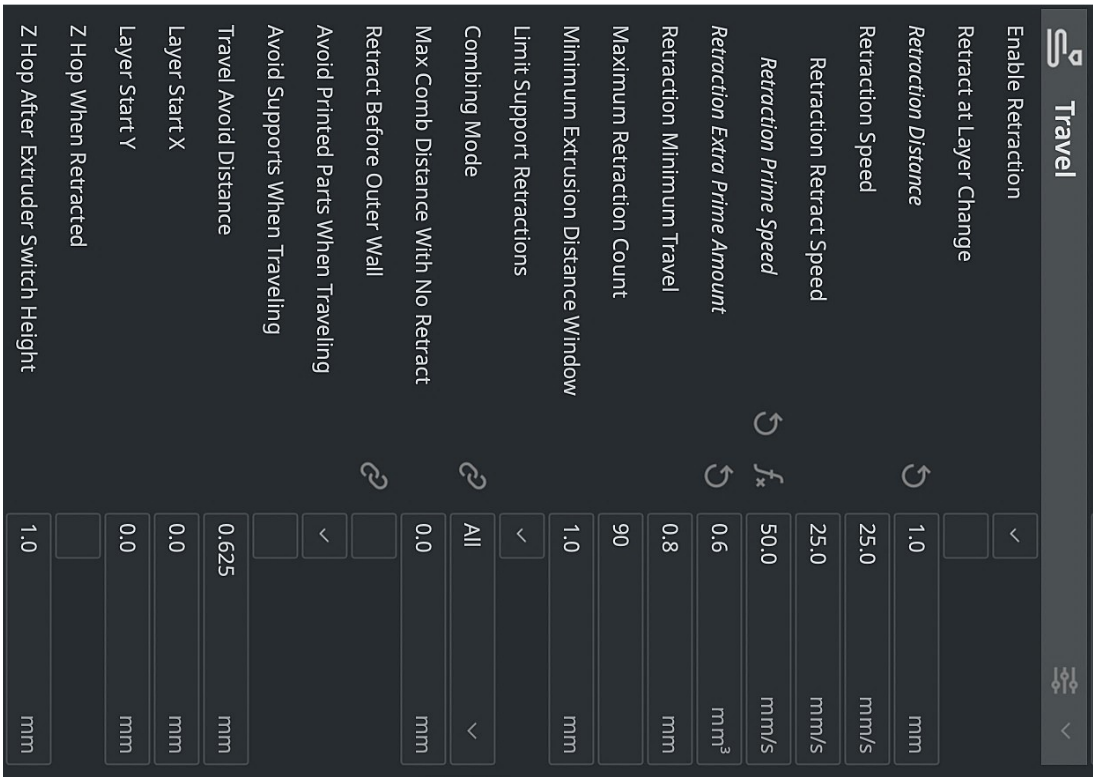
Travel
Enable Retraction
Retract at Layer Change
Retraction Distance 1.0 mm
Retraction Speed 25.0 mm/s
Retraction Retract Speed 25.0 mm/s
Retraction Prime Speed 50.0 mm/s
Retraction Extra Prime Amount 0.6 mm³
Retraction Minimum Travel 0.8 mm
Maximum Retraction Count 90
Minimum Extrusion Distance Window 1.0 mm
Limit Support Retractions
Combing Mode All
Max Comb Distance With No Retract 0.0 mm
Retract Before Outer Wall
Avoid Printed Parts When Traveling
Avoid Supports When Traveling
Travel Avoid Distance 0.625 mm
Layer Start X 0.0 mm
Layer Start Y 0.0 mm
Z Hop When Retracted
Z Hop After Extruder Switch Height 1.0 mm

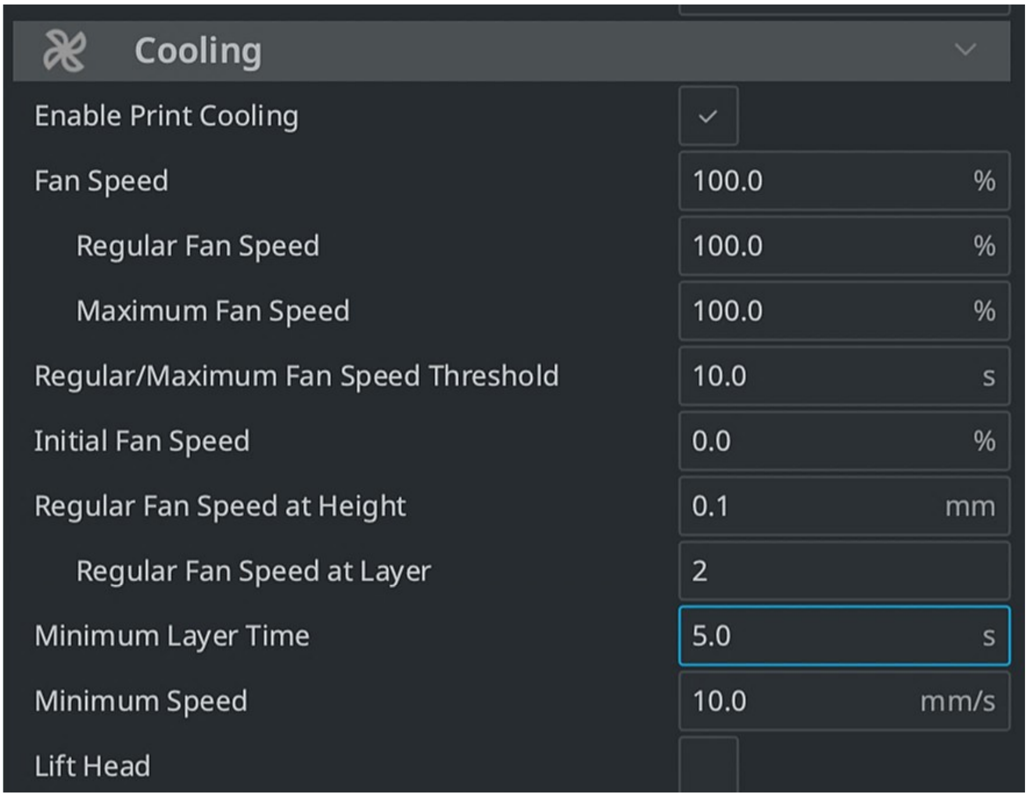
Cooling
Enable Print Cooling
Fan Speed 100.0 %
Regular Fan Speed 100.0 %
Maximum Fan Speed 100.0 %
Regular/Maximum Fan Speed Threshold 10.0 s
Initial Fan Speed 0.0 %
Regular Fan Speed at Height 0.1 mm
Regular Fan Speed at Layer 2
Minimum Layer Time 5.0 s
Minimum Speed 10.0 mm/s
Lift Head

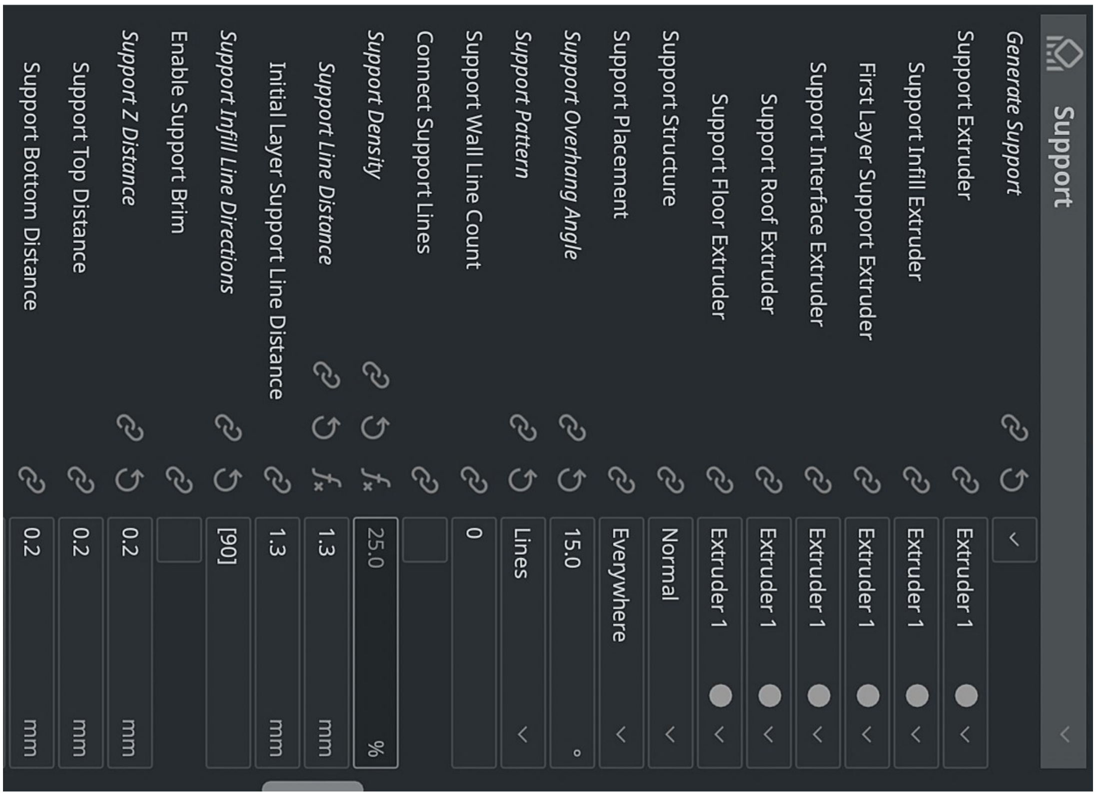
Support
Generate Support
Support Extruder
Extruder 1
Support Infill Extruder
Extruder 1
First Layer Support Extruder
Extruder 1
Support Interface Extruder
Extruder 1
Support Roof Extruder
Extruder 1
Support Floor Extruder
Extruder 1
Support Structure
Normal
Support Placement
Everywhere
Support Overhang Angle
15.0 °
Support Pattern
Lines
Support Wall Line Count
0
Connect Support Lines
Support Density
25.0 %
Support Line Distance
1.3 mm
Initial Layer Support Line Distance
1.3 mm
Support Infill Line Directions
[90]
Enable Support Brim
Support Z Distance
0.2 mm
Support Top Distance
0.2 mm
Support Bottom Distance
0.2 mm

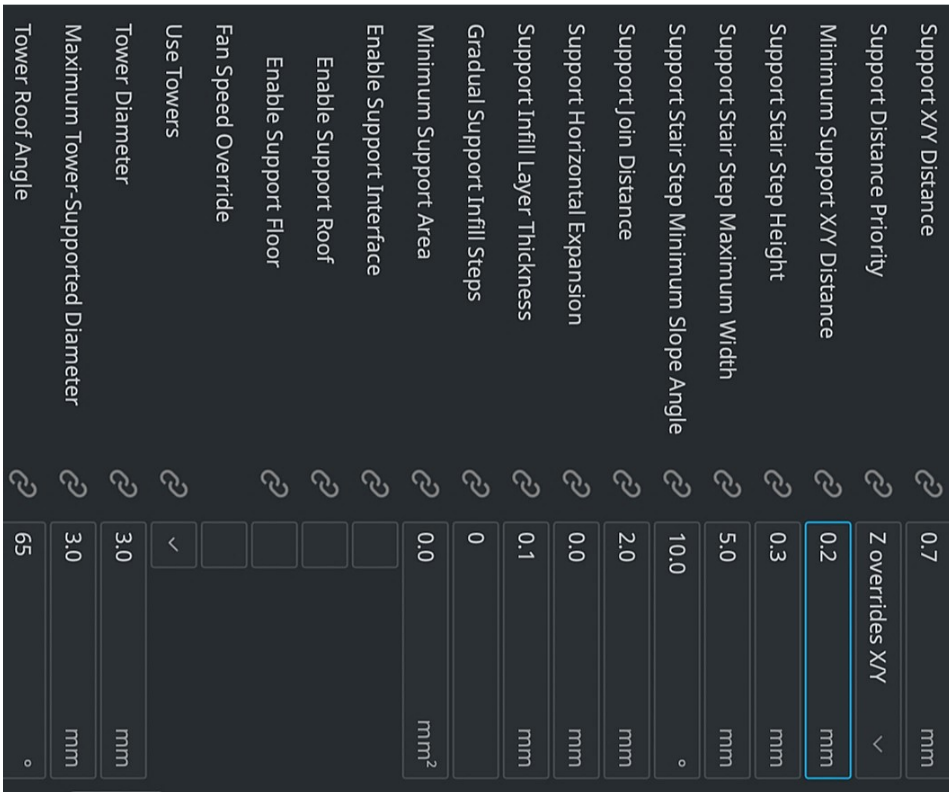
Support X/Y Distance
0.7 mm
Support Distance Priority
Z overrides X/Y
Minimum Support X/Y Distance
0.2 mm
Support Stair Step Height
0.3 mm
Support Stair Step Maximum Width
5.0 mm
Support Stair Step Minimum Slope Angle
10.0 °
Support Join Distance
2.0 mm
Support Horizontal Expansion
0.0 mm
Support Infill Layer Thickness
0.1 mm
Gradual Support Infill Steps
0
Minimum Support Area
0.0 mm²
Enable Support Interface
Enable Support Roof
Enable Support Floor
Fan Speed Override
Use Towers
Tower Diameter
3.0 mm
Maximum Tower-Supported Diameter
3.0 mm
Tower Roof Angle
65 °

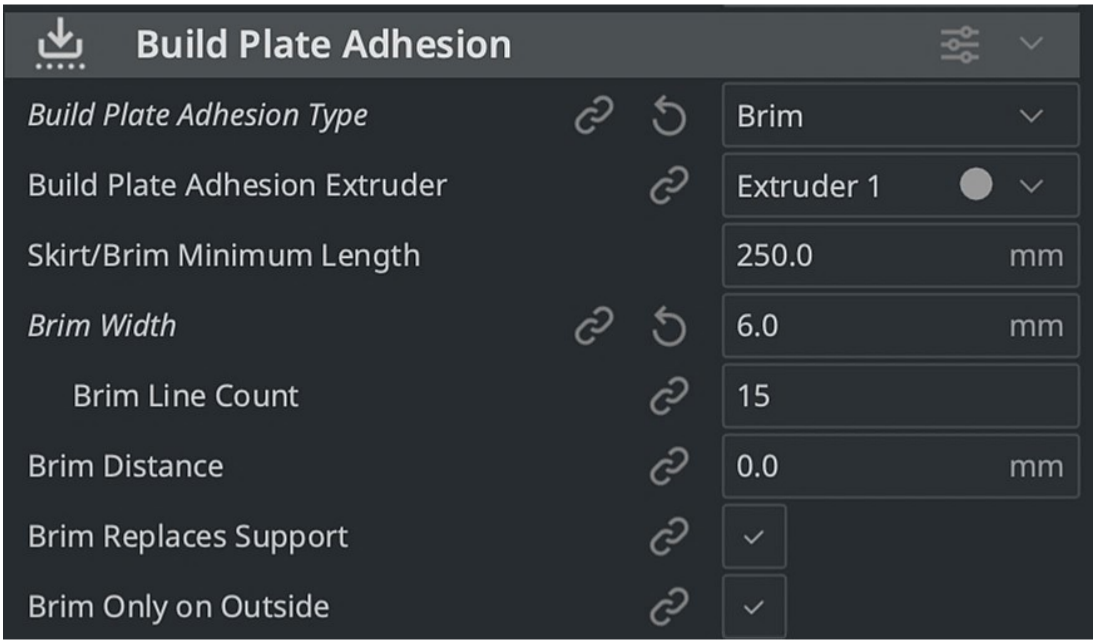
Build Plate Adhesion
Build Plate Adhesion Type
Brim
Build Plate Adhesion Extruder
Extruder 1
Skirt/Brim Minimum Length
250.0 mm
Brim Width
6.0 mm
Brim Line Count
15
Brim Distance
0.0 mm
Brim Replaces Support
Brim Only on Outside

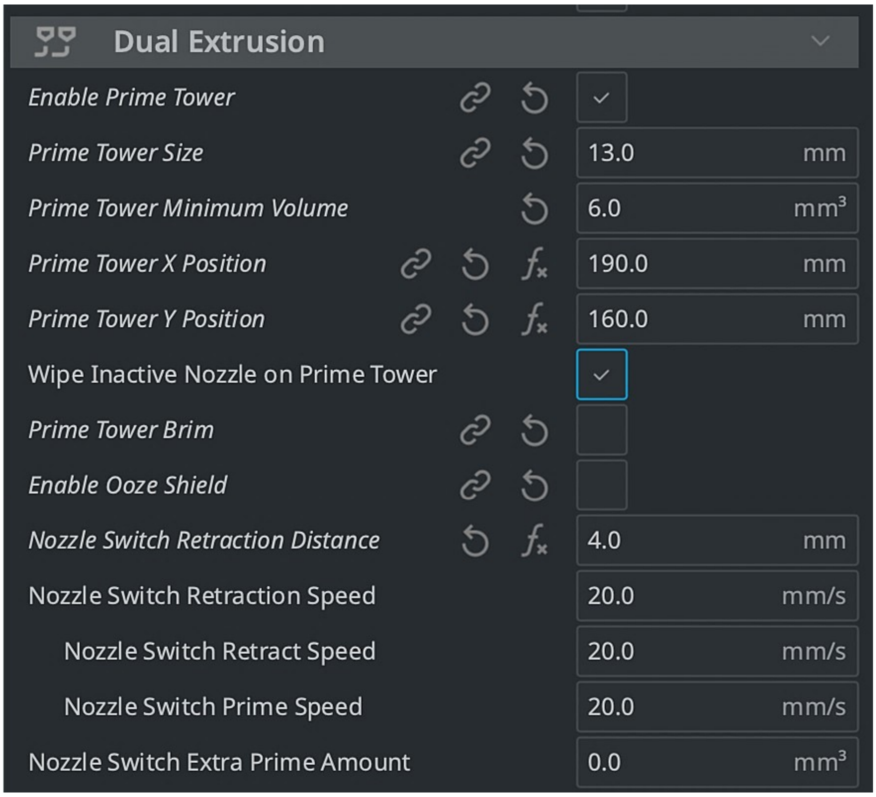
Dual Extrusion
Enable Prime Tower
Prime Tower Size
13.0 mm
Prime Tower Minimum Volume
6.0 mm³
Prime Tower X Position
190.0 mm
Prime Tower Y Position
160.0 mm
Wipe Inactive Nozzle on Prime Tower
Prime Tower Brim
Enable Ooze Shield
Nozzle Switch Retraction Distance
4.0 mm
Nozzle Switch Retraction Speed
20.0 mm/s
Nozzle Switch Retract Speed
20.0 mm/s
Nozzle Switch Prime Speed
20.0 mm/s
Nozzle Switch Extra Prime Amount
0.0 mm³

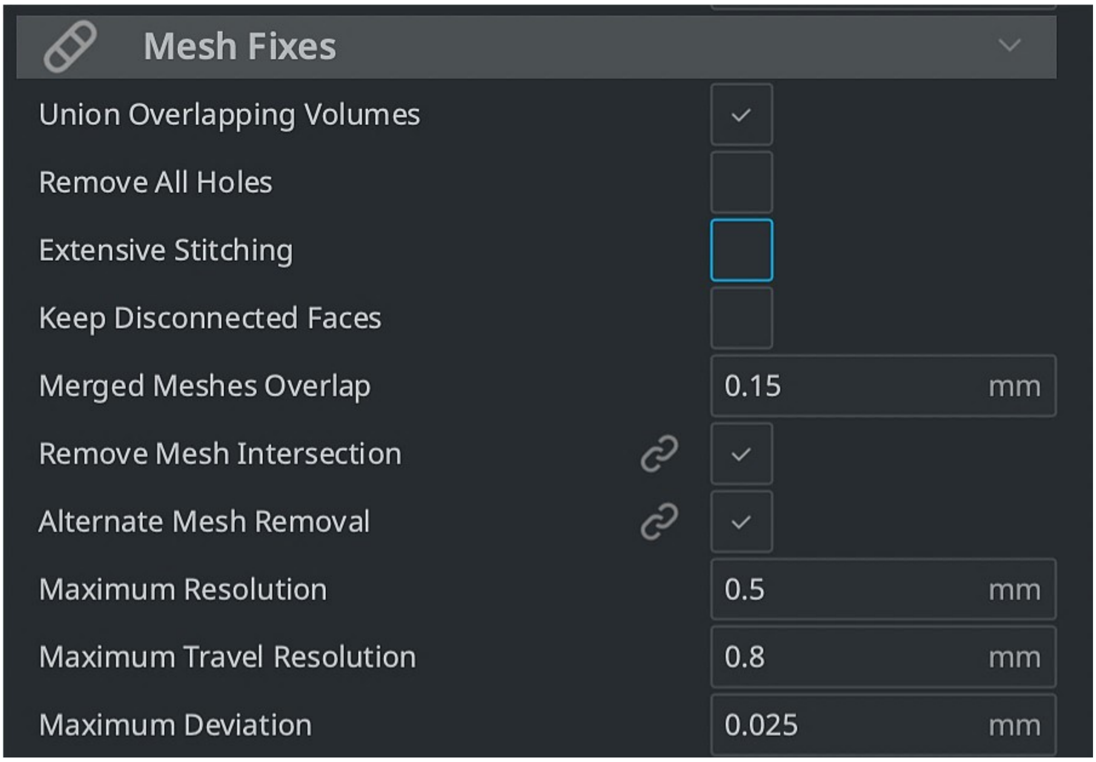
Mesh Fixes
Union Overlapping Volumes
Remove All Holes
Extensive Stitching
Keep Disconnected Faces
Merged Meshes Overlap
0.15 mm
Remove Mesh Intersection
Alternate Mesh Removal
Maximum Resolution
0.5 mm
Maximum Travel Resolution
0.8 mm
Maximum Deviation
0.025 mm

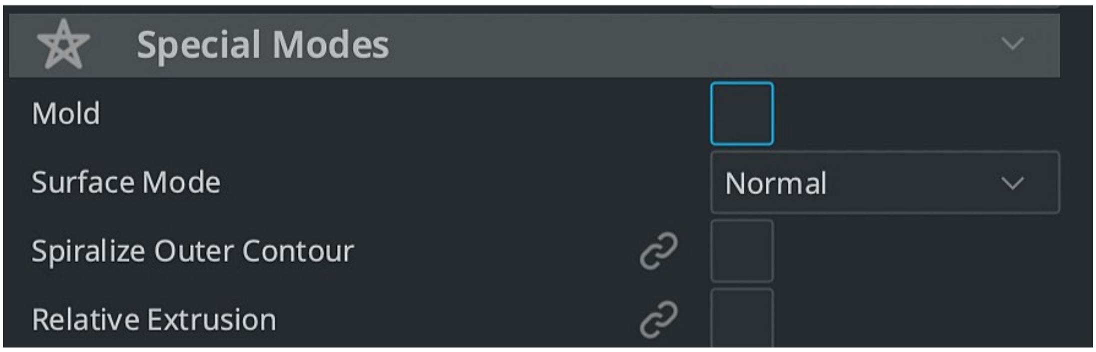
Special Modes
Mold
Surface Mode
Normal
Spiralize Outer Contour
Relative Extrusion


Experimental
Slicing Tolerance
Middle
Infill Travel Optimization
Minimum Polygon Circumference
1.0 mm
Enable Draft Shield
Make Overhang Printable
Enable Coasting
Coasting Volume
0.064 mm^3
Minimum Volume Before Coasting
0.8 mm^3
Coasting Speed
90.0 %
Enable Conical Support
Fuzzy Skin
Flow Rate Compensat...ax Extrusion Offset
0.0 mm
Flow Rate Compensation Factor
100.0 %
Wire Printing
Use Adaptive Layers
Overhanging Wall Angle
90.0 °
Overhanging Wall Speed
100.0 %
Enable Bridge Settings
Wipe Nozzle Between Layers
Small Hole Max Size
0.0 mm
Small Feature Max Length
0.0 mm
Small Feature Speed
50.0 %

B Cura Settings Nozzle 2

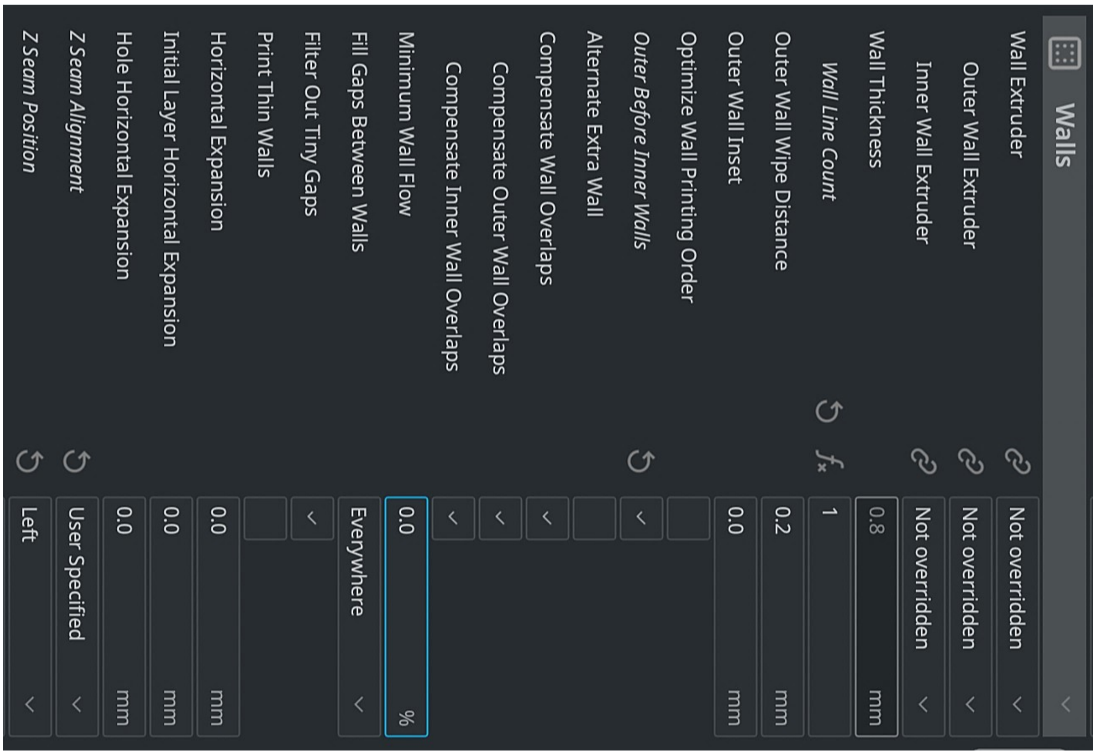

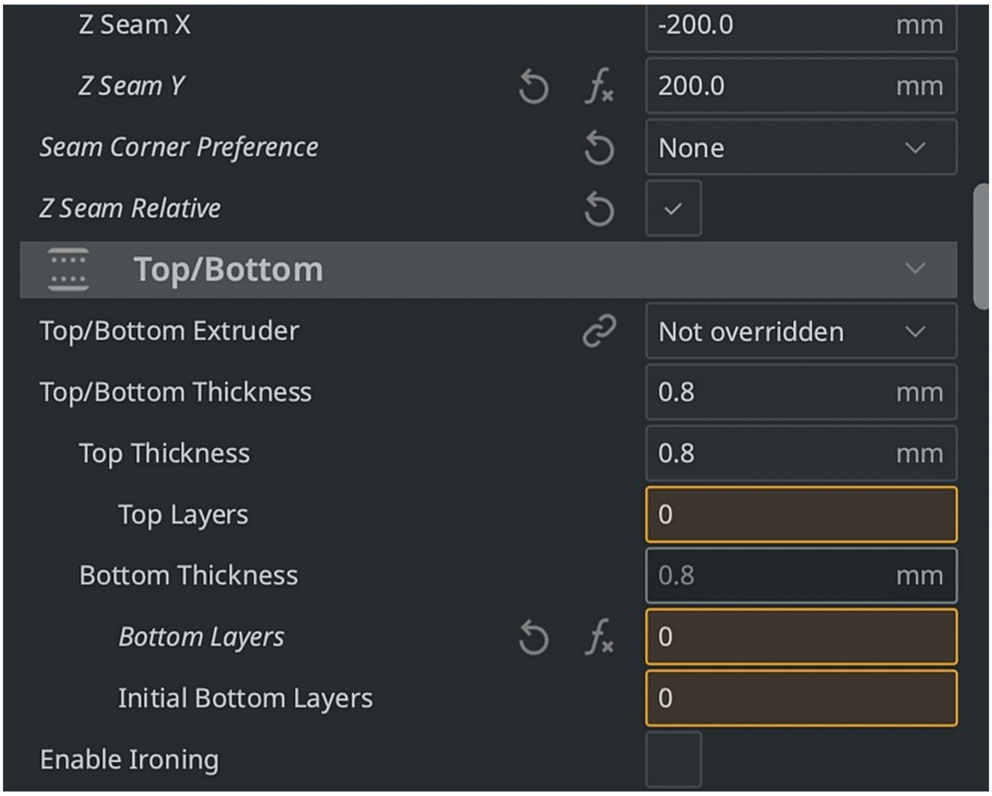
Z Seam X
-200.0 mm
Z Seam Y
200.0 mm
Seam Corner Preference
None
Z Seam Relative
Top/Bottom
Top/Bottom Extruder
Not overridden
Top/Bottom Thickness
0.8 mm
Top Thickness
0.8 mm
Top Layers
0
Bottom Thickness
0.8 mm
Bottom Layers
0
Initial Bottom Layers
0
Enable Ironing

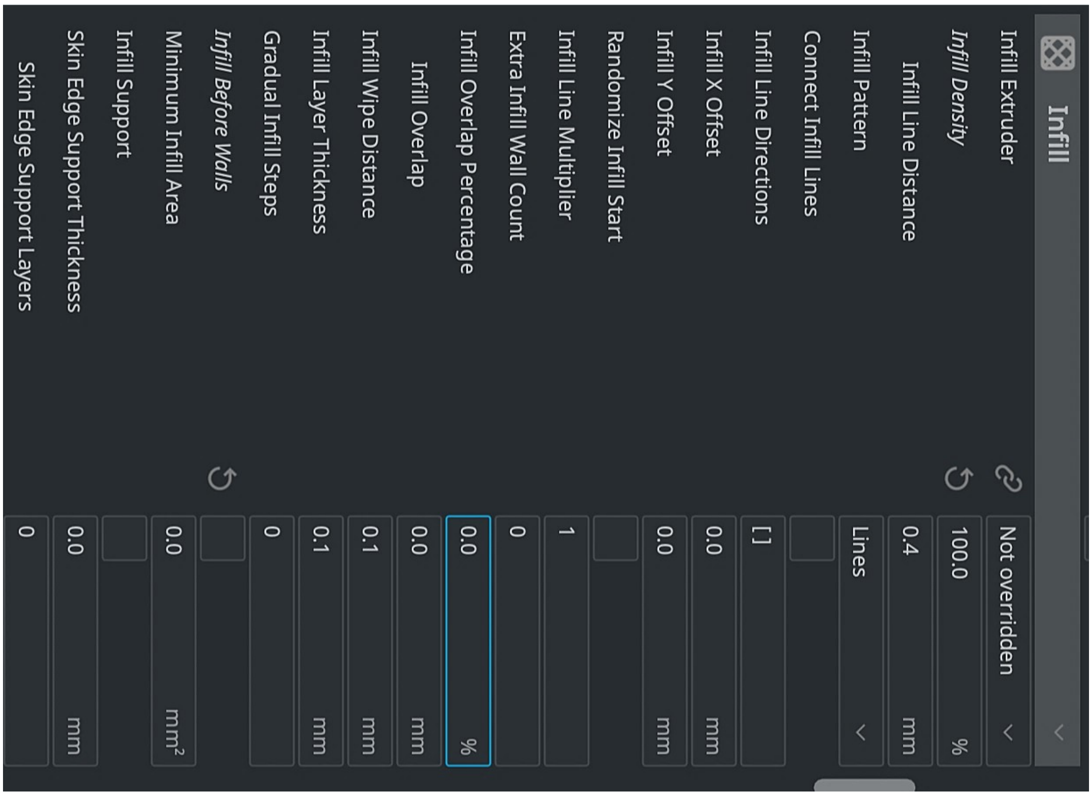
Infill
Infill Extruder
Not overridden
Infill Density
100.0 %
Infill Line Distance
0.4 mm
Infill Pattern
Lines
Connect Infill Lines
Infill Line Directions
[]
Infill X Offset
0.0 mm
Infill Y Offset
0.0 mm
Randomize Infill Start
Infill Line Multiplier
1
Extra Infill Wall Count
0
Infill Overlap Percentage
0.0 %
Infill Overlap
0.0 mm
Infill Wipe Distance
0.1 mm
Infill Layer Thickness
0.1 mm
Gradual Infill Steps
0
Infill Before Walls
Minimum Infill Area
0.0 mm²
Infill Support
Skin Edge Support Thickness
0.0 mm
Skin Edge Support Layers
0

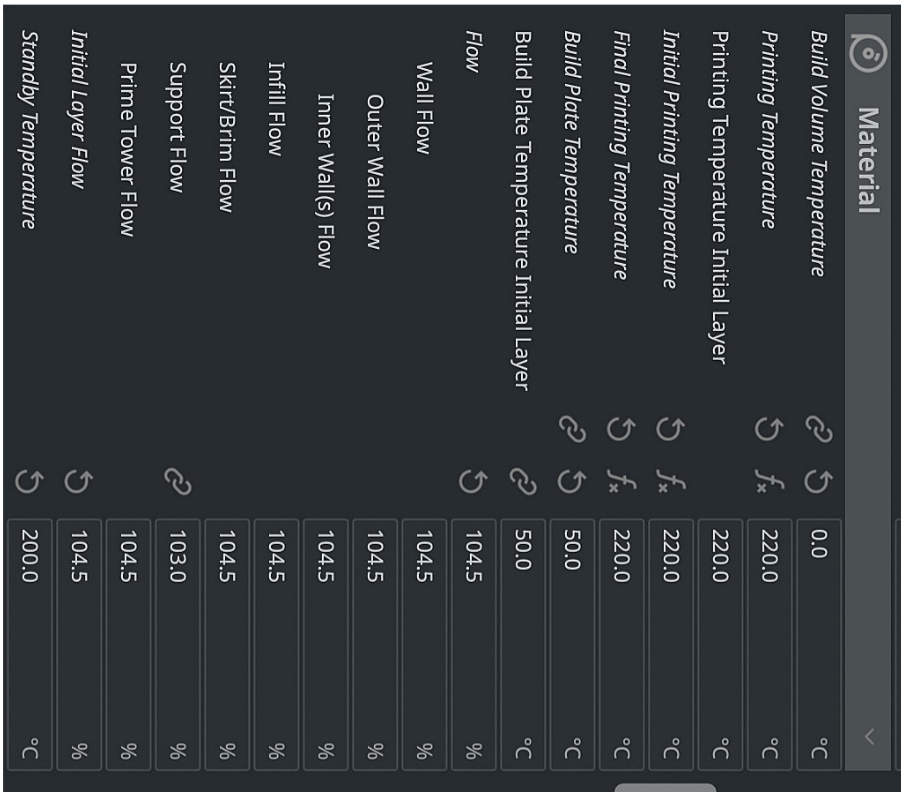
Material
Build Volume Temperature 0.0 °C
Printing Temperature 220.0 °C
Printing Temperature Initial Layer 220.0 °C
Initial Printing Temperature 220.0 °C
Final Printing Temperature 220.0 °C
Build Plate Temperature 50.0 °C
Build Plate Temperature Initial Layer 50.0 °C
Flow 104.5 %
Wall Flow 104.5 %
Outer Wall Flow 104.5 %
Inner Wall(s) Flow 104.5 %
Infill Flow 104.5 %
Skirt/Brim Flow 104.5 %
Support Flow 103.0 %
Prime Tower Flow 104.5 %
Initial Layer Flow 104.5 %
Standby Temperature 200.0 °C

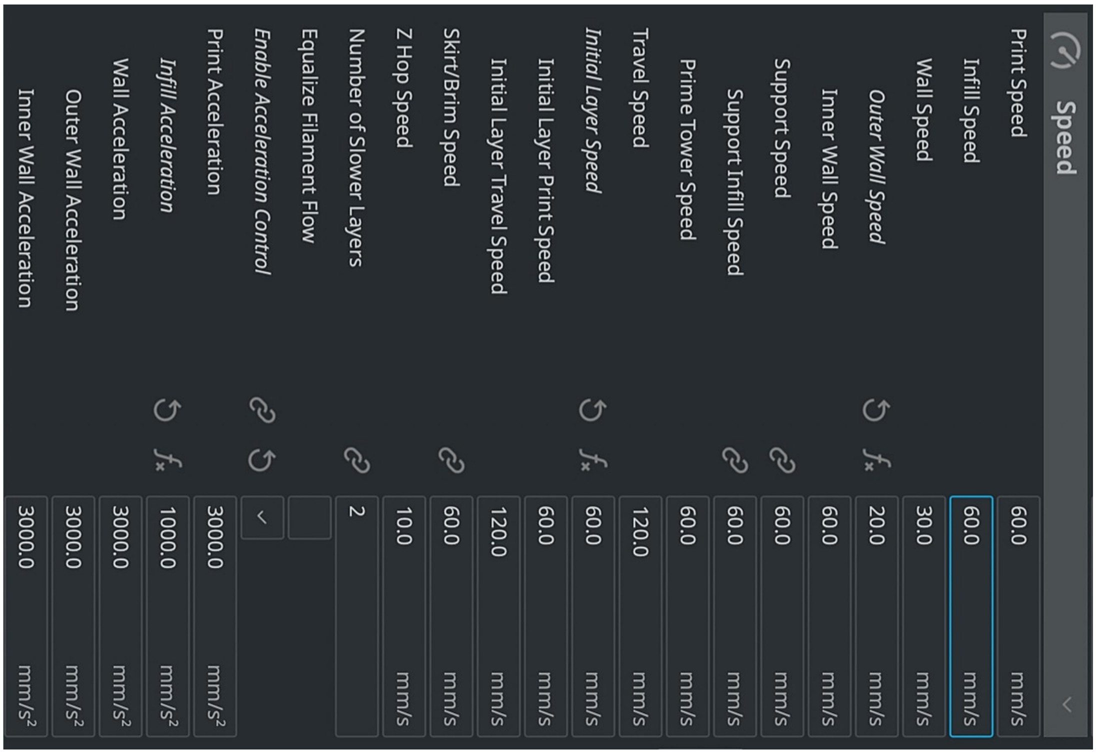
Speed
Print Speed 60.0 mm/s
Infill Speed 60.0 mm/s
Wall Speed 30.0 mm/s
Outer Wall Speed 20.0 mm/s
Inner Wall Speed 60.0 mm/s
Support Speed 60.0 mm/s
Support Infill Speed 60.0 mm/s
Prime Tower Speed 60.0 mm/s
Travel Speed 120.0 mm/s
Initial Layer Speed 60.0 mm/s
Initial Layer Print Speed 60.0 mm/s
Initial Layer Travel Speed 120.0 mm/s
Skirt/Brim Speed 60.0 mm/s
Z Hop Speed 10.0 mm/s
Number of Slower Layers 2
Equalize Filament Flow
Enable Acceleration Control
Print Acceleration 3000.0 mm/s^2
Infill Acceleration 1000.0 mm/s^2
Wall Acceleration 3000.0 mm/s^2
Outer Wall Acceleration 3000.0 mm/s^2
Inner Wall Acceleration 3000.0 mm/s^2

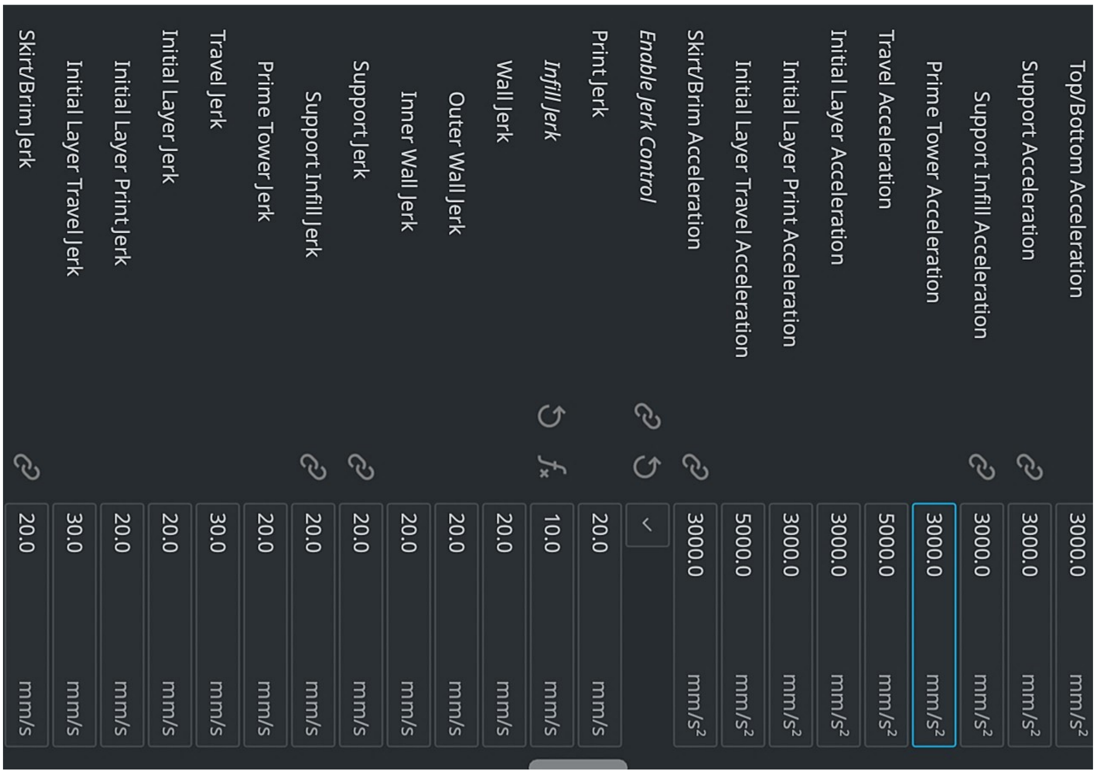

Top/Bottom Acceleration 3000.0 mm/s^2
Support Acceleration 3000.0 mm/s^2
Support Infill Acceleration 3000.0 mm/s^2
Prime Tower Acceleration 3000.0 mm/s^2
Travel Acceleration 5000.0 mm/s^2
Initial Layer Acceleration 3000.0 mm/s^2
Initial Layer Print Acceleration 3000.0 mm/s^2
Initial Layer Travel Acceleration 5000.0 mm/s^2
Skirt/Brim Acceleration 3000.0 mm/s^2
Enable Jerk Control
Print Jerk 20.0 mm/s
Infill Jerk 10.0 mm/s
Wall Jerk 20.0 mm/s
Outer Wall Jerk 20.0 mm/s
Inner Wall Jerk 20.0 mm/s
Support Jerk 20.0 mm/s
Support Infill Jerk 20.0 mm/s
Prime Tower Jerk 20.0 mm/s
Travel Jerk 30.0 mm/s
Initial Layer Jerk 20.0 mm/s
Initial Layer Print Jerk 20.0 mm/s
Initial Layer Travel Jerk 30.0 mm/s
Skirt/Brim Jerk 20.0 mm/s

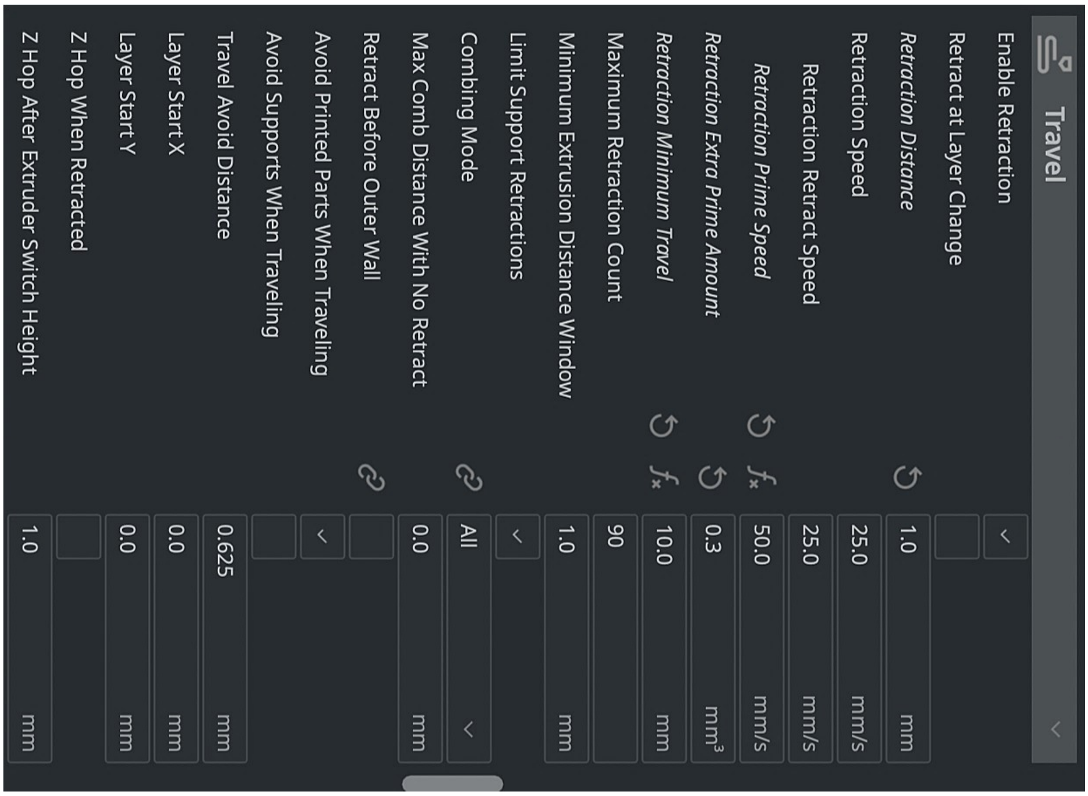

Travel
Enable Retraction
Retract at Layer Change
Retraction Distance 1.0 mm
Retraction Speed 25.0 mm/s
Retraction Retract Speed 25.0 mm/s
Retraction Prime Speed 50.0 mm/s
Retraction Extra Prime Amount 0.3 mm^3
Retraction Minimum Travel 10.0 mm
Maximum Retraction Count 90
Minimum Extrusion Distance Window 1.0 mm
Limit Support Retractions
Combing Mode All
Max Comb Distance With No Retract 0.0 mm
Retract Before Outer Wall
Avoid Printed Parts When Traveling
Avoid Supports When Traveling
Travel Avoid Distance 0.625 mm
Layer Start X 0.0 mm
Layer Start Y 0.0 mm
Z Hop When Retracted
Z Hop After Extruder Switch Height 1.0 mm

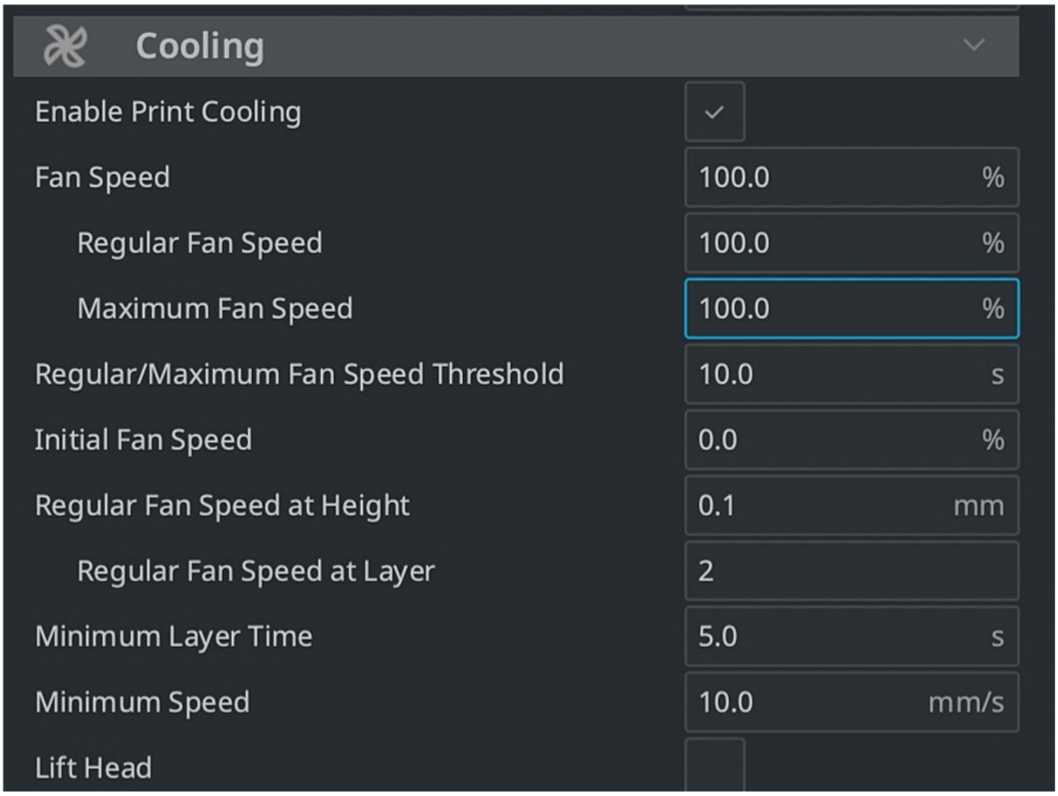
Cooling
Enable Print Cooling
Fan Speed 100.0 %
Regular Fan Speed 100.0 %
Maximum Fan Speed 100.0 %
Regular/Maximum Fan Speed Threshold 10.0 s
Initial Fan Speed 0.0 %
Regular Fan Speed at Height 0.1 mm
Regular Fan Speed at Layer 2
Minimum Layer Time 5.0 s
Minimum Speed 10.0 mm/s
Lift Head

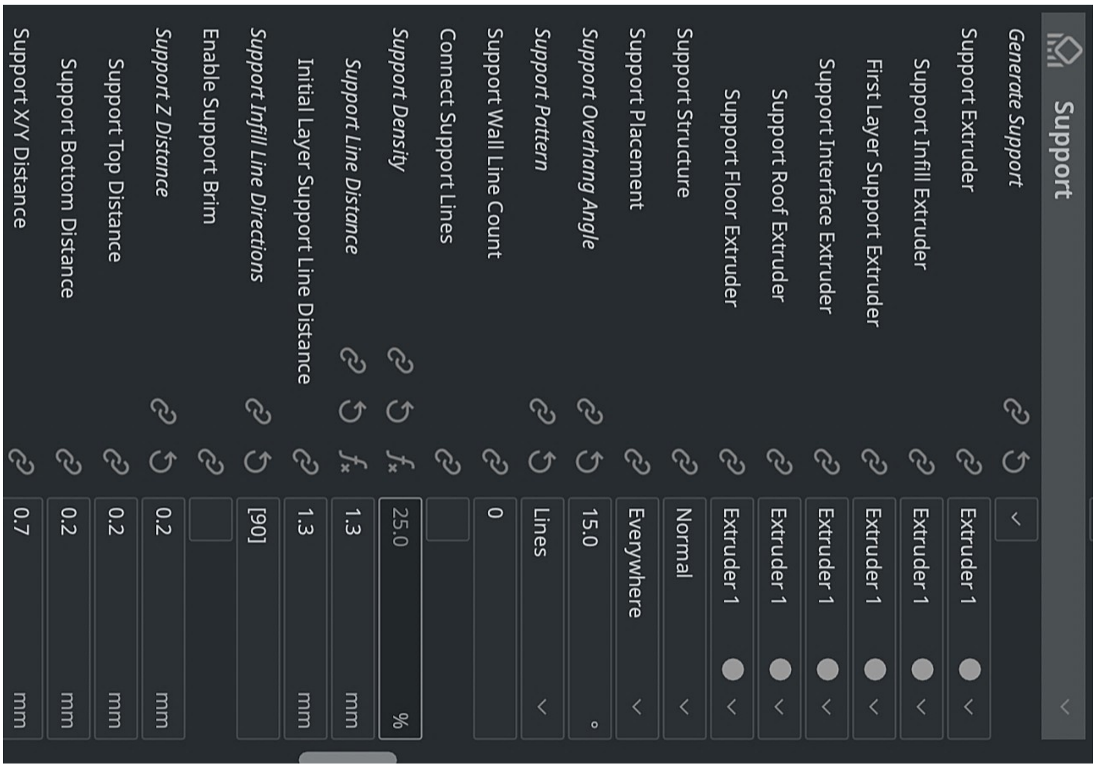
Support
Generate Support
Support Extruder Extruder 1
Support Infill Extruder Extruder 1
First Layer Support Extruder Extruder 1
Support Interface Extruder Extruder 1
Support Roof Extruder Extruder 1
Support Floor Extruder Extruder 1
Support Structure Normal
Support Placement Everywhere
Support Overhang Angle 15.0 °
Support Pattern Lines
Support Wall Line Count 0
Connect Support Lines
Support Density 25.0 %
Support Line Distance 1.3 mm
Initial Layer Support Line Distance 1.3 mm
Support Infill Line Directions [90]
Enable Support Brim
Support Z Distance 0.2 mm
Support Top Distance 0.2 mm
Support Bottom Distance 0.2 mm
Support X/Y Distance 0.7 mm

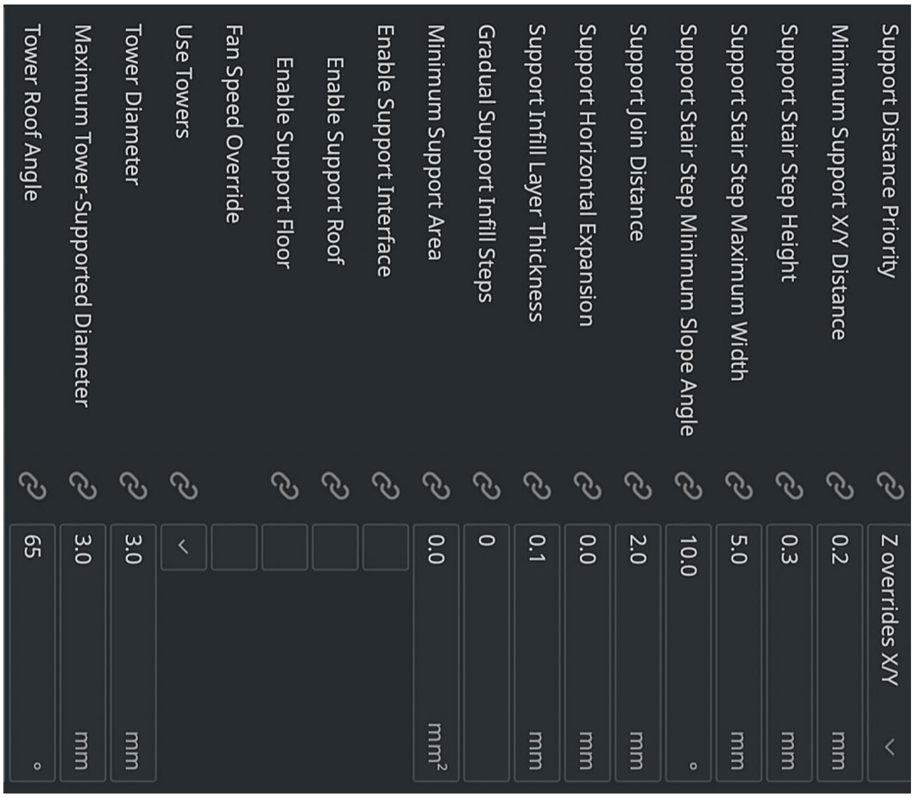

Support Distance Priority
Z overrides X/Y
Minimum Support X/Y Distance
0.2 mm
Support Stair Step Height
0.3 mm
Support Stair Step Maximum Width
5.0 mm
Support Stair Step Minimum Slope Angle
10.0 °
Support Join Distance
2.0 mm
Support Horizontal Expansion
0.0 mm
Support Infill Layer Thickness
0.1 mm
Gradual Support Infill Steps
0
Minimum Support Area
0.0 mm²
Enable Support Interface
Enable Support Roof
Enable Support Floor
Fan Speed Override
Use Towers
Tower Diameter
3.0 mm
Maximum Tower-Supported Diameter
3.0 mm
Tower Roof Angle
65 °

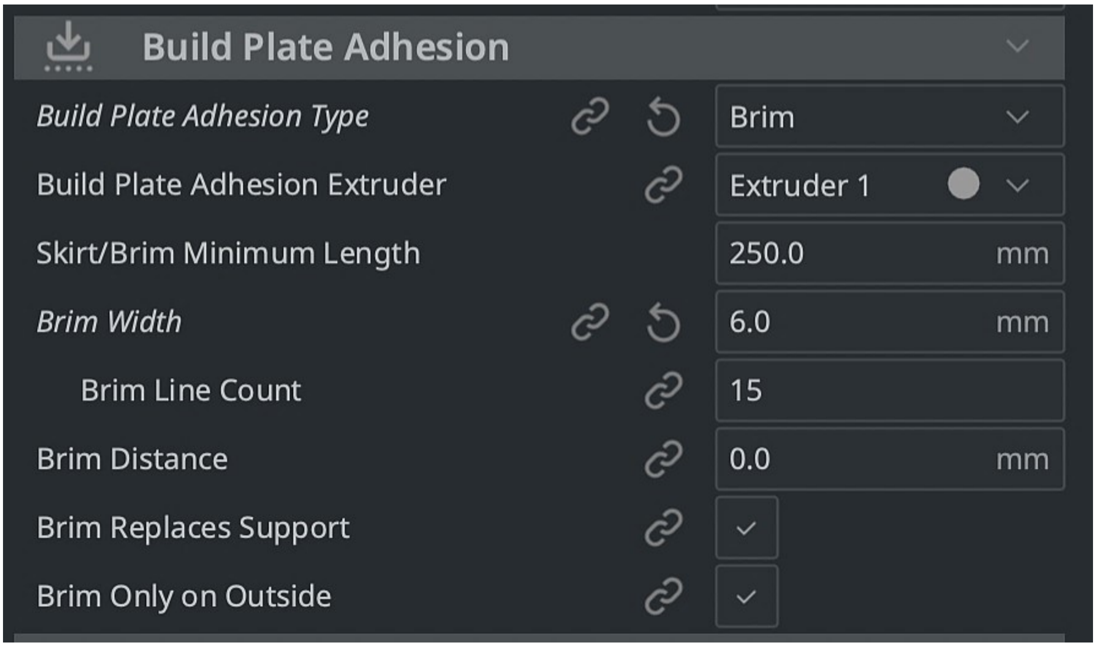

Build Plate Adhesion
Build Plate Adhesion Type
Brim
Build Plate Adhesion Extruder
Extruder 1
Skirt/Brim Minimum Length
250.0 mm
Brim Width
6.0 mm
Brim Line Count
15
Brim Distance
0.0 mm
Brim Replaces Support
Brim Only on Outside

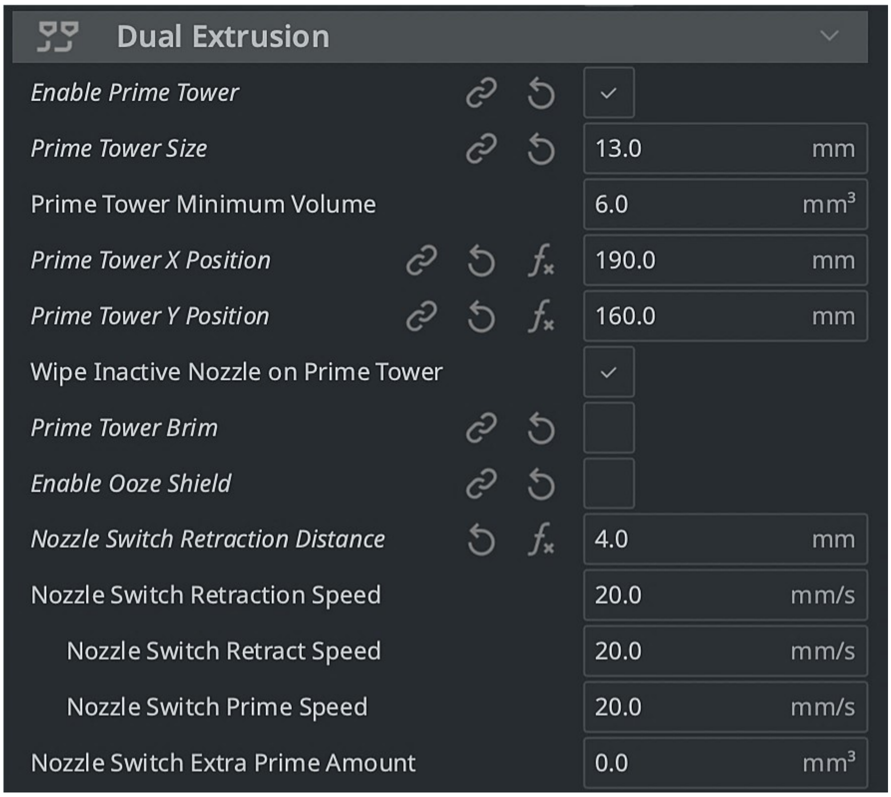
Dual Extrusion
Enable Prime Tower
Prime Tower Size
13.0 mm
Prime Tower Minimum Volume
6.0 mm³
Prime Tower X Position
190.0 mm
Prime Tower Y Position
160.0 mm
Wipe Inactive Nozzle on Prime Tower
Prime Tower Brim
Enable Ooze Shield
Nozzle Switch Retraction Distance
4.0 mm
Nozzle Switch Retraction Speed
20.0 mm/s
Nozzle Switch Retract Speed
20.0 mm/s
Nozzle Switch Prime Speed
20.0 mm/s
Nozzle Switch Extra Prime Amount
0.0 mm³

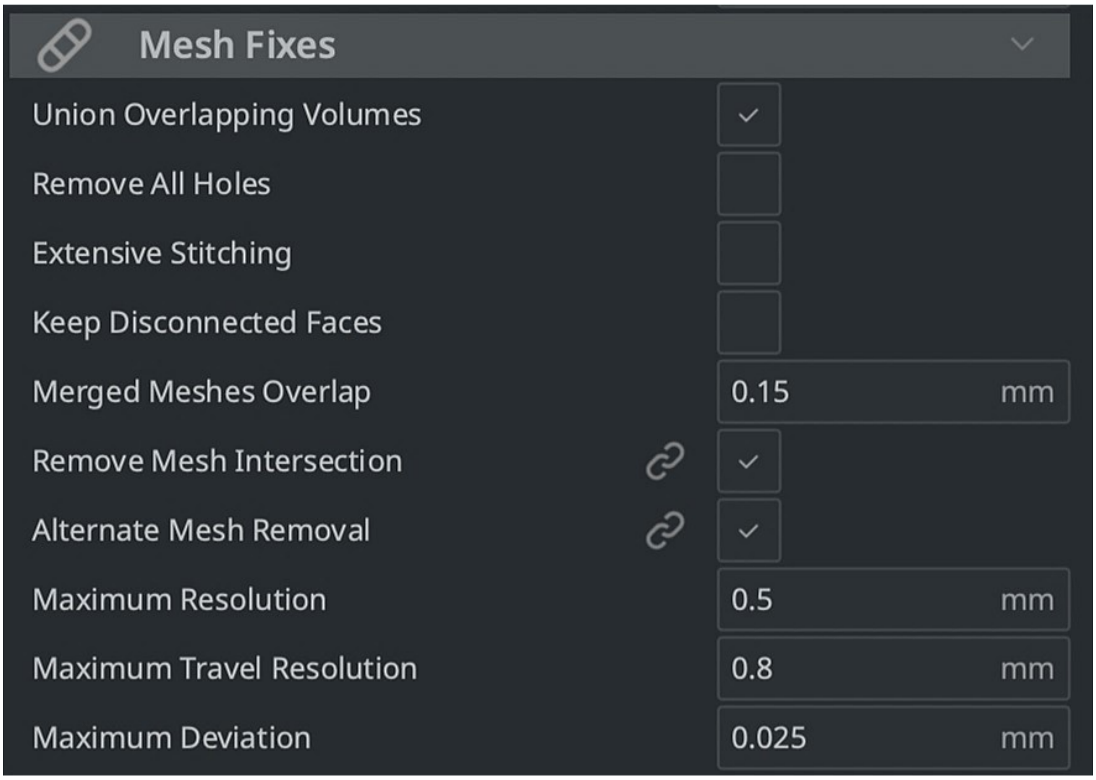
Mesh Fixes
Union Overlapping Volumes
Remove All Holes
Extensive Stitching
Keep Disconnected Faces
Merged Meshes Overlap
0.15 mm
Remove Mesh Intersection
Alternate Mesh Removal
Maximum Resolution
0.5 mm
Maximum Travel Resolution
0.8 mm
Maximum Deviation
0.025 mm

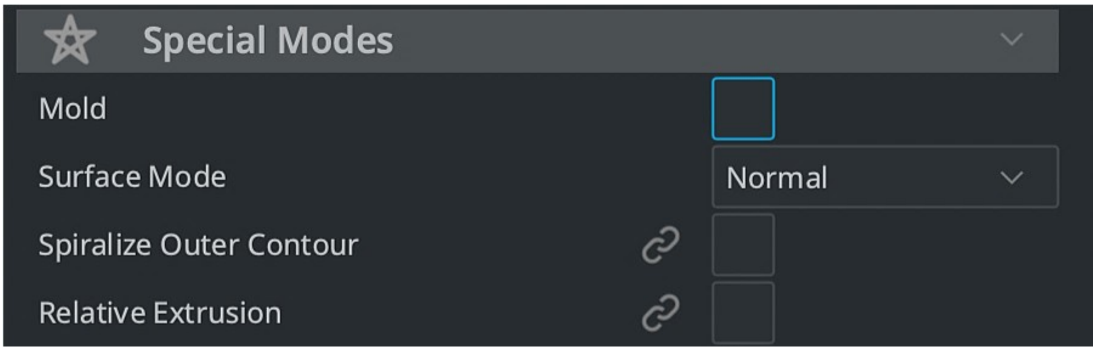
Special Modes
Mold
Surface Mode
Normal
Spiralize Outer Contour
Relative Extrusion


Experimental
Slicing Tolerance
Middle
Infill Travel Optimization
Minimum Polygon Circumference
1.0 mm
Enable Draft Shield
Make Overhang Printable
Enable Coasting
Coasting Volume
0.064 mm³
Minimum Volume Before Coasting
0.8 mm³
Coasting Speed
90.0 %
Enable Conical Support
Fuzzy Skin
Flow Rate Compensat...ax Extrusion Offset
0.0 mm
Flow Rate Compensation Factor
100.0 %
Wire Printing
Use Adaptive Layers
Overhanging Wall Angle
90.0 °
Overhanging Wall Speed
100.0 %
Enable Bridge Settings
Wipe Nozzle Between Layers

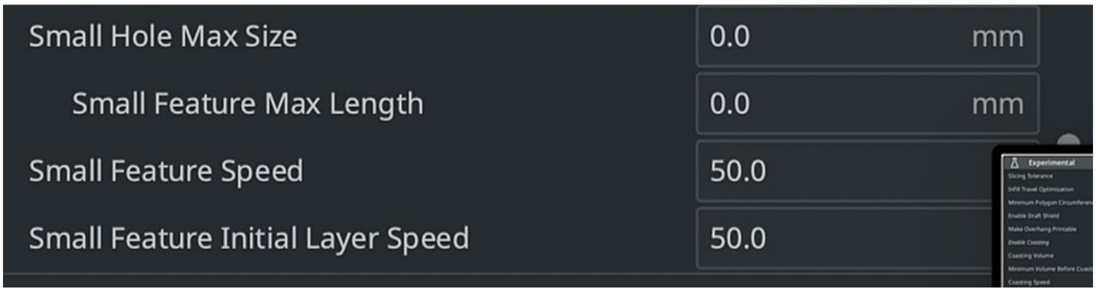
Small Hole Max Size
0.0 mm
Small Feature Max Length
0.0 mm
Small Feature Speed
50.0
Small Feature Initial Layer Speed
50.0

C Fracture Specimen Manufacturing Data

Disc number	SCB number	Date printed:	Location	Angle	Date cut:	Tested:	Type	Material	DIC	Additinoal comment
1	1	14.2.2022	1	0	4.3.2022	4.5.2022	Bi-material	PLA/PLA	Yes	
1	2	14.2.2022	1	0	4.3.2022	19.04.2022	Bi-material	PLA/PLA		
2	3	14.2.2022	2	0	4.3.2022	19.04.2022	Bi-material	PLA/PLA		
2	4	14.2.2022	2	0	4.3.2022	22.05.2022	Bi-material	PLA/PLA		
3	5	14.2.2022	3	15	4.3.2022	19.04.2022	Bi-material	PLA/PLA		Red half lower
4	6	15.2.2022	1	15	4.3.2022	4.5.2022	Bi-material	PLA/PLA	Yes	Red half lower
5	7	18.3.2022	3	15	5.4.2022	19.04.2022	Bi-material	PLA/PLA		Red half lower
6	8	16.2.2022	1	15	4.3.2022	22.05.2022	Bi-material	PLA/PLA		Red half lower
3	9	14.2.2022	3	15	4.3.2022	19.04.2022	Bi-material	PLA/PLA		Grey half lower
4	10	15.2.2022	1	15	4.3.2022	4.5.2022	Bi-material	PLA/PLA	Yes	Grey half lower
5	11	18.3.2022	2	15	5.4.2022	19.04.2022	Bi-material	PLA/PLA		Grey half lower
ED10	12	6.5.2022	2	15	21.5.2022	22.05.2022	Bi-material	PLA/PLA		Grey half lower
7	13	16.2.2022	2	30	4.3.2022	4.5.2022	Bi-material	PLA/PLA	Yes	Red half lower
8	14	17.2.2022	1	30	4.3.2022	19.04.2022	Bi-material	PLA/PLA		Red half lower
9	15	17.2.2022	2	30	4.3.2022	19.04.2022	Bi-material	PLA/PLA		Red half lower
10	16	17.2.2022	3	30	4.3.2022	22.05.2022	Bi-material	PLA/PLA		Red half lower
7	17	16.2.2022	2	30	4.3.2022	4.5.2022	Bi-material	PLA/PLA	Yes	Grey half lower
8	18	17.2.2022	1	30	4.3.2022	19.04.2022	Bi-material	PLA/PLA		Grey half lower
9	19	17.2.2022	2	30	4.3.2022	19.04.2022	Bi-material	PLA/PLA		Grey half lower
10	20	17.2.2022	3	30	4.3.2022	22.05.2022	Bi-material	PLA/PLA		Grey half lower
ED11	21	6.5.2022	3	40	21.5.2022	22.05.2022	Bi-material	PLA/PLA		Red half lower
12	22	18.2.2022	1	40	4.3.2022	4.5.2022	Bi-material	PLA/PLA	Yes	Red half lower
13	23	18.3.2022	2	40	5.4.2022	22.05.2022	Bi-material	PLA/PLA		Red half lower
ED12	24	6.5.2022	4	40	21.5.2022	22.05.2022	Bi-material	PLA/PLA		Red half lower
11	25	17.2.2022	4	40	4.3.2022	22.05.2022	Bi-material	PLA/PLA		Grey half lower
12	26	18.2.2022	1	40	4.3.2022	4.5.2022	Bi-material	PLA/PLA	Yes	Grey half lower
ED11	27	6.5.2022	3	40	21.5.2022	22.05.2022	Bi-material	PLA/PLA		Grey half lower
ED12	28	6.5.2022	4	40	21.5.2022	22.05.2022	Bi-material	PLA/PLA		Grey half lower
15	29	21.2.2022	1	0	4.3.2022	4.5.2022	Single-material	GREY PLA	Yes	
15	30	21.2.2022	1	0	4.3.2022	19.04.2022	Single-material	GREY PLA		
16	31	21.2.2022	2	0	4.3.2022	19.04.2022	Single-material	GREY PLA		
16	32	21.2.2022	2	0	4.3.2022	22.05.2022	Single-material	GREY PLA		
17	33	21.2.2022	3	15	4.3.2022	4.5.2022	Single-material	GREY PLA	Yes	
17	34	21.2.2022	3	15	4.3.2022	19.04.2022	Single-material	GREY PLA		
18	35	21.2.2022	4	15	4.3.2022	19.04.2022	Single-material	GREY PLA		
18	36	21.2.2022	4	15	4.3.2022	22.05.2022	Single-material	GREY PLA		
19	37	22.2.2022	1	30	4.3.2022	4.5.2022	Single-material	GREY PLA	Yes	
19	38	22.2.2022	1	30	4.3.2022	19.04.2022	Single-material	GREY PLA		
20	39	22.2.2022	2	30	4.3.2022	19.04.2022	Single-material	GREY PLA		
20	40	22.2.2022	2	30	4.3.2022	22.05.2022	Single-material	GREY PLA		
21	41	22.2.2022	3	40	4.3.2022	4.5.2022	Single-material	GREY PLA	Yes	
21	42	20.5.2022	1	40	21.5.2022	22.05.2022	Single-material	GREY PLA		
22	43	20.5.2022	1	40	21.5.2022	22.05.2022	Single-material	GREY PLA		
22	44	22.2.2022	4	40	4.3.2022	22.05.2022	Single-material	GREY PLA		
23	45	28.2.2022	1	0	4.3.2022	4.5.2022	Single-material	RED PLA	Yes	
23	46	28.2.2022	1	0	4.3.2022	19.04.2022	Single-material	RED PLA		
24	47	23.2.2022	2	0	4.3.2022	19.04.2022	Single-material	RED PLA		
24	48	23.2.2022	2	0	4.3.2022	22.05.2022	Single-material	RED PLA		
25	49	23.2.2022	3	15	4.3.2022	4.5.2022	Single-material	RED PLA	Yes	
25	50	23.2.2022	3	15	4.3.2022	19.04.2022	Single-material	RED PLA		
ED5	51	25.4.2022	1	15	2.5.2022	22.05.2022	Single-material	RED PLA		
ED5	52	25.4.2022	1	15	2.5.2022	22.05.2022	Single-material	RED PLA		
ED14	53	20.5.2022	1	30	21.5.2022	22.05.2022	Single-material	RED PLA		
27	54	25.2.2022	1	30	4.3.2022	19.04.2022	Single-material	RED PLA		
28	55	25.2.2022	2	30	4.3.2022	19.04.2022	Single-material	RED PLA		
28	56	25.2.2022	2	30	4.3.2022	22.05.2022	Single-material	RED PLA	Yes	
29	57	25.2.2022	3	40	4.3.2022	4.5.2022	Single-material	RED PLA	Yes	
ED15	58	20.5.2022	2	40	21.5.2022	22.05.2022	Single-material	RED PLA		
ED15	59	20.5.2022	2	40	21.5.2022	22.05.2022	Single-material	RED PLA		
30	60	25.2.2022	4	40	4.3.2022	22.05.2022	Single-material	RED PLA		

Filament changes:

Date:	Color:	Notes:
8.3.2022	Grey	Morning
16.3.2022	Red	Morning
26.4.2022	Grey	Rest of large roll found in 3D-printing lab. Used while waiting for new roll
6.5.2022	Grey	Before ED9
12.5.2022	Red	Morning

SCB number	Label	Date printed:	Location	Angle	Date cut:	Tested:	Type	Material	DIC:	Additinoal comment
61	SD1	31.3.2022	1	0	5.4.2022	4.5.2022	Bi-material	PLA/PLA	Yes	
62	SD1	31.3.2022	1	0	5.4.2022	19.04.2022	Bi-material	PLA/PLA		
63	SD31	20.4.2022	1	0	2.5.2022	22.5.2022	Bi-material	PLA/PLA		
64	SD2	31.3.2022	2	0	5.4.2022	19.04.2022	Bi-material	PLA/PLA		
65	SD32	20.4.2022	2	15	2.5.2022	22.5.2022	Bi-material	PLA/PLA		Red half lower
66	SD4	31.3.2022	4	15	5.4.2022	19.04.2022	Bi-material	PLA/PLA		Red half lower
67	SD5	1.4.2022	1	15	5.4.2022	4.5.2022	Bi-material	PLA/PLA	Yes	Red half lower
68	SD6	1.4.2022	2	15	5.4.2022	19.04.2022	Bi-material	PLA/PLA		Red half lower
69	SD32	20.4.2022	2	15	2.5.2022	22.5.2022	Bi-material	PLA/PLA		Grey half lower
70	SD4	31.3.2022	4	15	5.4.2022	19.04.2022	Bi-material	PLA/PLA		Grey half lower
71	SD5	1.4.2022	1	15	5.4.2022	4.5.2022	Bi-material	PLA/PLA	Yes	Grey half lower
72	SD6	1.4.2022	2	15	5.4.2022	19.04.2022	Bi-material	PLA/PLA		Grey half lower
73	SD43	6.5.2022	1	30	21.5.2022	22.5.2022	Bi-material	PLA/PLA		Red half lower
74	SD8	2.4.2022	1	30	5.4.2022	4.5.2022	Bi-material	PLA/PLA	Yes	Red half lower
75	SD46	9.5.2022	1	30	21.5.2022	22.5.2022	Bi-material	PLA/PLA		Red half lower
76	SD10	3.4.2022	1	30	5.4.2022	22.5.2022	Bi-material	PLA/PLA		Red half lower
77	SD7	1.4.2022	4	30	5.4.2022	19.04.2022	Bi-material	PLA/PLA		Grey half lower
78	SD8	2.4.2022	1	30	5.4.2022	4.5.2022	Bi-material	PLA/PLA	Yes	Grey half lower
79	SD9	2.4.2022	2	30	5.4.2022	19.04.2022	Bi-material	PLA/PLA		Grey half lower
80	SD10	3.4.2022	1	30	5.4.2022	22.5.2022	Bi-material	PLA/PLA		Grey half lower
81	SD11	3.4.2022	2	40	5.4.2022	4.5.2022	Bi-material	PLA/PLA	Yes	Red half lower
82	SD33	20.4.2022	3	40	2.5.2022	22.5.2022	Bi-material	PLA/PLA		Red half lower
83	SD44	6.5.2022	2	40	21.5.2022	22.5.2022	Bi-material	PLA/PLA		Red half lower
84	SD45	6.5.2022	3	40	21.5.2022	22.5.2022	Bi-material	PLA/PLA		Red half lower
85	SD11	3.4.2022	2	40	21.5.2022	22.5.2022	Bi-material	PLA/PLA		Grey half lower
86	SD44	6.5.2022	2	40	21.5.2022	22.5.2022	Bi-material	PLA/PLA		Grey half lower
87	SD33	20.4.2022	3	40	2.5.2022	4.5.2022	Bi-material	PLA/PLA	Yes	Grey half lower
88	SD45	6.5.2022	3	40	21.5.2022	22.5.2022	Bi-material	PLA/PLA		Grey half lower
89	SD35	21.4.2022	1	0	2.5.2022	4.5.2022	Single-material	GREY PLA	Yes	
90	SD35	21.4.2022	1	0	2.5.2022	22.5.2022	Single-material	GREY PLA		
91	SD36	21.4.2022	2	0	2.5.2022	22.5.2022	Single-material	GREY PLA		
92	SD36	21.4.2022	2	0	2.5.2022	22.5.2022	Single-material	GREY PLA		
93	SD37	21.4.2022	3	15	2.5.2022	4.5.2022	Single-material	GREY PLA	Yes	
94	SD37	21.4.2022	3	15	2.5.2022	22.5.2022	Single-material	GREY PLA		
95	SD38	21.4.2022	4	15	2.5.2022	22.5.2022	Single-material	GREY PLA		
96	SD38	21.4.2022	4	15	2.5.2022	22.5.2022	Single-material	GREY PLA		
97	SD60	19.5.2022	1	30	21.5.2022	22.5.2022	Single-material	GREY PLA		
98	SD39	26.4.2022	1	30	2.5.2022	22.5.2022	Single-material	GREY PLA	Yes	
99	SD40	26.4.2022	2	30	2.5.2022	22.5.2022	Single-material	GREY PLA		
100	SD40	26.4.2022	2	30	2.5.2022	22.5.2022	Single-material	GREY PLA		
101	SD41	26.4.2022	3	40	2.5.2022	4.5.2022	Single-material	GREY PLA	Yes	
102	SD41	26.4.2022	3	40	2.5.2022	22.5.2022	Single-material	GREY PLA		
103	SD42	26.4.2022	4	40	2.5.2022	22.5.2022	Single-material	GREY PLA		
104	SD42	26.4.2022	4	40	2.5.2022	22.5.2022	Single-material	GREY PLA		
105	SD50	11.5.2022	1	0	21.5.2022	22.5.2022	Single-material	RED PLA	Yes	
106	SD50	11.5.2022	1	0	21.5.2022	22.5.2022	Single-material	RED PLA		
107	SD51	11.5.2022	2	0	21.5.2022	22.5.2022	Single-material	RED PLA		
108	SD51	11.5.2022	2	0	21.5.2022	22.5.2022	Single-material	RED PLA		
109	SD52	11.5.2022	3	15	21.5.2022	22.5.2022	Single-material	RED PLA	Yes	
110	SD52	11.5.2022	3	15	21.5.2022	22.5.2022	Single-material	RED PLA		
111	SD53	11.5.2022	4	15	21.5.2022	22.5.2022	Single-material	RED PLA		
112	SD53	11.5.2022	4	15	21.5.2022	22.5.2022	Single-material	RED PLA		
113	SD54	12.5.2022	1	30	21.5.2022	22.5.2022	Single-material	RED PLA	Yes	
114	SD54	12.5.2022	1	30	21.5.2022	22.5.2022	Single-material	RED PLA		
115	SD55	12.5.2022	2	30	21.5.2022	22.5.2022	Single-material	RED PLA		
116	SD55	12.5.2022	2	30	21.5.2022	22.5.2022	Single-material	RED PLA		
117	SD56	12.5.2022	1	40	21.5.2022	22.5.2022	Single-material	RED PLA	Yes	
118	SD56	12.5.2022	1	40	21.5.2022	22.5.2022	Single-material	RED PLA		
119	SD57	12.5.2022	2	40	21.5.2022	22.5.2022	Single-material	RED PLA		
120	SD57	12.5.2022	2	40	21.5.2022	22.5.2022	Single-material	RED PLA		

D Code

File - C:\Users\stein\OneDrive - NTNU\Master Thesis\Python\Plotter\getListOfFolders.py

```python
import os

path = r"C:\Users\stein\OneDrive - NTNU\Master Thesis\Python\Plotter\Data" #Path of files with data

def getListOfFolders():# returns a list of foldes in path
    listOfFolders = os.listdir(path) #gets folders in path
    listOfFolders.sort(key=float) #sort folders in ascending order

    return listOfFolders


def getNameOfCSV(specimenNumber):

    subpath = path+"/"+str(specimenNumber) #makes a path with the specimen which the program is looking for

    filesInSubPath = os.listdir(subpath) #Creates a list with all files in subpath

    for i in filesInSubPath:
        if "Stop" in i: #find .CSV file with "Stop" in filename
            return i #Returns name of .CSV file

```

Page 1 of 1

```python
import numpy as np
import pandas as pd
import matplotlib.pyplot as plt
import getListOfFolders as glof
import matplotlib.pyplot as plt
from varname import nameof

layingBi = [i for i in range(1,29)]         #Make list from 1 to 28
layingGray = [i for i in range(29,45)]      #Make list from 29 to 44
layingRed = [i for i in range(45,61)]       #Make list from 45 to 60
standingBi = [i for i in range(61,89)]      #Make list from 61 to 88
standingGray = [i for i in range(89,105)]   #Make list from 89 to 104
standingRed = [i for i in range(105,121)]   #Make list from 105 to 120
DIC = [1,6,10,13,17,22,26,29,33,37,41,45,49,53,57,61,67,71,74,78,81,87,89,93,97,101,105,109,113,117]
allSpecimen = [i for i in range(1,121)]     #Make list from 1 to 120





Load = "Load(Linear:Load) (N)"
Displacement = "Displacement(Linear:Digital Position) (mm)"



"""Get angle for specimen"""

def getSpecimenAngle(specimen):

    angleDataFrame = pd.read_csv("SpecimenAngles.csv",sep=";")

    return angleDataFrame[str(specimen)][0]


def getFractureForce(specimen):

    df = pd.read_csv("C:/Users/stein/OneDrive - NTNU/Master Thesis/Python/Plotter/Data/" + str(specimen) + "/" + str(glof.getNameOfCSV(specimen)), sep=";", decimal=",") #Open file

    df.drop(["Total Time (s)", "Cycle Elapsed Time (s)", "Total Cycles", "Elapsed Cycles", "Step", "Total Cycle Count(Linear Waveform)"], axis=1, inplace=True) #remove data which is not used

    df[Load] = df[Load] * -1 #Inverting values
    df[Displacement] = (df[Displacement] - df.iloc[0,2] ) * -1 #Inverting values

    for c in range(150, len(df.index)):  # Loop to interate through data and find fracture point
        if df.iloc[c, 1] < 100:
            # fracturePoint = c

            return df.iloc[c-2,1] #Returns fracture load

    return df.iloc[-1,1] #return final value if no fracture point was
```

```python
found


def plot(listName,nameOfPlot):
    listFractureForce = []
    listSpecimenAngle = []
    specimenLabels = []

    for i in listName:
        if str(i) in glof.getListOfFolders():
            listFractureForce.append(getFractureForce(i))
            listSpecimenAngle.append(getSpecimenAngle(i))
            specimenLabels.append(i)

    # print(listFractureForce)

    plt.title(nameOfPlot)
    plt.scatter(listSpecimenAngle, listFractureForce)

    # for i, txt in enumerate(listName):
    #     print(i)
    #     print(txt)
    #     if str(txt) in glof.getListOfFolders():
    #         plt.annotate(str(txt), (listSpecimenAngle[i], int(listFractureForce[i])))

    for i, txt in enumerate(specimenLabels):
        print(i)
        print(txt)
        if str(txt) in glof.getListOfFolders():
            if txt in DIC:
                plt.annotate(str(txt), (listSpecimenAngle[i], int(listFractureForce[i])), c="red")
            else:
                plt.annotate(str(txt), (listSpecimenAngle[i], int(listFractureForce[i])))

    print(specimenLabels)
    print(listFractureForce)

    # plt.savefig(f"{nameOfPlot} scatter")
    # plt.show()

"""Exectute plotter here"""
###########################################################################################
plot(allSpecimen,"LayingRed")
###########################################################################################
```

```python
#Used to plot specimen by angle and fracture load to evaluate the data during the testing period

import pandas as pd

import getListOfFolders as glof
import matplotlib.pyplot as plt


layingBi = [i for i in range(1,29)]         #Make list from 1 to 28
layingGray = [i for i in range(29,45)]      #Make list from 29 to 44
layingRed = [i for i in range(45,61)]       #Make list from 45 to 60
standingBi = [i for i in range(61,89)]      #Make list from 61 to 88
standingGray = [i for i in range(89,105)]   #Make list from 89 to 104
standingRed = [i for i in range(105,121)]   #Make list from 105 to 120
DIC = [1,6,10,13,17,22,26,29,33,37,41,45,49,53,57,61,67,71,74,78,81,87,89,93,97,101,105,109,113,117]

testList = [62,64,66,68,70,72,73,75,77,79,83,84,86,88]
currentlyTestedRed = ["46","47","50","54","55"]




Load = "Load(Linear:Load) (N)"
Displacement = "Displacement(Linear:Digital Position) (mm)"



"""Get angle for specimen"""

def getSpecimenAngle(specimen): #Function to get crack angle of specimen
    angleDataFrame = pd.read_csv("SpecimenAngles.csv",sep=";")

    return angleDataFrame[str(specimen)][0]


def getFractureForce(specimen): #function to get fracture force of a specimen

    df = pd.read_csv("C:/Users/stein/OneDrive - NTNU/Master Thesis/Python/Plotter/Data/" + str(specimen) + "/" + str(glof.getNameOfCSV(specimen)), sep=";", decimal=",")

    df.drop(["Total Time (s)", "Cycle Elapsed Time (s)", "Total Cycles", "Elapsed Cycles", "Step", "Total Cycle Count(Linear Waveform)"], axis=1, inplace=True)

    df[Load] = df[Load] * -1 #Inverting values
    df[Displacement] = (df[Displacement] - df.iloc[0,2] ) * -1 # Inverting values

    for c in range(100, len(df.index)):  # Loop to interate through data and find fracture point
        if df.iloc[c, 1] < 100: #Finds fracture point

```

```python
            return df.iloc[c-2,1]   #Returns fracture force

    return df.iloc[-1,1] #returns last datapoint of no fracture point is found


def plot(listName,nameOfPlot):
    listFractureForce = []
    listSpecimenAngle = []
    specimenLabels = []

    for i in listName:
        if str(i) in glof.getListOfFolders():
            listFractureForce.append(getFractureForce(i))
            listSpecimenAngle.append(getSpecimenAngle(i))
            specimenLabels.append(i)

    # print(listFractureForce)

    plt.title(nameOfPlot)
    plt.scatter(listSpecimenAngle, listFractureForce)



    for i, txt in enumerate(specimenLabels):
        print(i)
        print(txt)
        if str(txt) in glof.getListOfFolders(): #Plots specimen captured with DIC in red
            if txt in DIC:
                plt.annotate(str(txt), (listSpecimenAngle[i], int(listFractureForce[i])), c="red")
            else:
                plt.annotate(str(txt), (listSpecimenAngle[i], int(listFractureForce[i])))

    plt.savefig(f"{nameOfPlot} scatter")
    plt.show()

"""Exectute plotter here"""
#############################################################################################
plot(layingRed,"LayingRed")
#############################################################################################
```

```python
#Code used to plot every specimen to evaluate the test

import pandas as pd
import getListOfFolders as glof
import matplotlib.pyplot as plt


listOfAllSpecimen = [i for i in range(1,121)]        #Make list from 1 to 120

Load = "Load(Linear:Load) (N)"
Displacement = "Displacement(Linear:Digital Position) (mm)"

for i in listOfAllSpecimen:

    if str(i) in glof.getListOfFolders():
        df = pd.read_csv("C:/Users/stein/OneDrive - NTNU/Master Thesis/Python/Plotter/Data/" + str(i) + "/" + str(glof.getNameOfCSV(i)), sep=";", decimal=",") #Reads .CSV files

        df.drop(["Total Time (s)", "Cycle Elapsed Time (s)", "Total Cycles", "Elapsed Cycles", "Step","Total Cycle Count(Linear Waveform)"], axis=1, inplace=True) #Removes data not being used

        df[Load] = df[Load] * -1  # Inverting values
        df[Displacement] = (df[Displacement] - df.iloc[0, 2]) * -1  # Inverting values

        df.plot(x=Displacement, y=Load) #Plots data
        plt.title(str(i))               #Adds title to plot
        plt.show()                      #Shows plot

        input("Press Enter to dispaly next plot!")  #Waits for user input before showing plot of next specimen.
```

E Fracture Loads

Specimen	Angle:	Type	Material	Fracture Load	Mode Mixity	Mean	St.Dev
1	0	Bi-material	PLA/PLA	1642.2	1.0		
2	0	Bi-material	PLA/PLA	1442.4	1.0		
3	0	Bi-material	PLA/PLA	1375.2	1.0		
4	0	Bi-material	PLA/PLA	1780.1	1.0	1560.0	160.6
5	15	Bi-material	PLA/PLA	1922.3	0.78		
6	15	Bi-material	PLA/PLA	2069.9	0.78		
7	15	Bi-material	PLA/PLA	1130.9	0.78		
8	15	Bi-material	PLA/PLA	2303.1	0.78		
9	15	Bi-material	PLA/PLA	2044.7	0.78		
10	15	Bi-material	PLA/PLA	2574.4	0.78		
11	15	Bi-material	PLA/PLA	1817.3	0.78		
12	15	Bi-material	PLA/PLA	2264.8	0.78	2015.9	401.8
13	30	Bi-material	PLA/PLA	3340.2	0.46		
14	30	Bi-material	PLA/PLA	3638.0	0.46		
15	30	Bi-material	PLA/PLA	3418.8	0.46		
16	30	Bi-material	PLA/PLA	3854.9	0.46		
17	30	Bi-material	PLA/PLA	3511.8	0.46		
18	30	Bi-material	PLA/PLA	3231.2	0.46		
19	30	Bi-material	PLA/PLA	4253.5	0.46		
20	30	Bi-material	PLA/PLA	4008.0	0.46	3657.1	331.3
21	40	Bi-material	PLA/PLA	2510.6	0.65		
22	40	Bi-material	PLA/PLA	2594.6	0.65		
23	40	Bi-material	PLA/PLA	2315.7	0.65		
24	40	Bi-material	PLA/PLA	3215.0	0.65		
25	40	Bi-material	PLA/PLA	3141.9	0.65		
26	40	Bi-material	PLA/PLA	2966.7	0.65		
27	40	Bi-material	PLA/PLA	2665.5	0.65		
28	40	Bi-material	PLA/PLA	2786.5	0.65	2774.6	293.8
29	0	Single-material	GRAY PLA	2048.1	1.0		
30	0	Single-material	GRAY PLA	2264.4	1.0		
31	0	Single-material	GRAY PLA	1920.8	1.0		
32	0	Single-material	GRAY PLA	2528.5	1.0	2190.4	230.6
33	15	Single-material	GRAY PLA	2289.9	0.78		
34	15	Single-material	GRAY PLA	1963.1	0.78		
35	15	Single-material	GRAY PLA	2066.1	0.78		
36	15	Single-material	GRAY PLA	1799.9	0.78	2029.8	177.7
37	30	Single-material	GRAY PLA	3187.1	0.46		
38	30	Single-material	GRAY PLA	3741.1	0.46		
39	30	Single-material	GRAY PLA	3359.7	0.46		
40	30	Single-material	GRAY PLA	3148.2	0.46	3359.0	234.5
41	40	Single-material	GRAY PLA	2586.2	0.65		
42	40	Single-material	GRAY PLA	2506.2	0.65		
43	40	Single-material	GRAY PLA	2480.3	0.65		
44	40	Single-material	GRAY PLA	2578.3	0.65	2537.7	45.5
45	0	Single-material	RED PLA	2091.0	1.0		
46	0	Single-material	RED PLA	2249.4	1.0		
47	0	Single-material	RED PLA	2082.3	1.0		
48	0	Single-material	RED PLA	2183.0	1.0	2151.4	68.9
49	15	Single-material	RED PLA	2173.9	0.78		
50	15	Single-material	RED PLA	2622.7	0.78		
51	15	Single-material	RED PLA	2864.3	0.78		
52	15	Single-material	RED PLA	2230.2	0.78	2472.8	284.6

53	30	Single-material	RED PLA	2769.6	0.46		
54	30	Single-material	RED PLA	3121.0	0.46		
55	30	Single-material	RED PLA	Excluded	0.46		
56	30	Single-material	RED PLA	Excluded	0.46	2945.3	175.7
57	40	Single-material	RED PLA	2355.2	0.65		
58	40	Single-material	RED PLA	2355.4	0.65		
59	40	Single-material	RED PLA	2080.8	0.65		
60	40	Single-material	RED PLA	2034.7	0.65	2206.5	149.7
61	0	Bi-material	PLA/PLA	1197.2	1.0		
62	0	Bi-material	PLA/PLA	1245.0	1.0		
63	0	Bi-material	PLA/PLA	974.5	1.0		
64	0	Bi-material	PLA/PLA	773.0	1.0	1047.4	188.5
65	15	Bi-material	PLA/PLA	1881.5	0.78		
66	15	Bi-material	PLA/PLA	2029.9	0.78		
67	15	Bi-material	PLA/PLA	1976.2	0.78		
68	15	Bi-material	PLA/PLA	2060.2	0.78		
69	15	Bi-material	PLA/PLA	2228.5	0.78		
70	15	Bi-material	PLA/PLA	2143.3	0.78		
71	15	Bi-material	PLA/PLA	2190.4	0.78		
72	15	Bi-material	PLA/PLA	2660.5	0.78	2146.3	221.7
73	30	Bi-material	PLA/PLA	Excluded	0.46		
74	30	Bi-material	PLA/PLA	3009.7	0.46		
75	30	Bi-material	PLA/PLA	Excluded	0.46		
76	30	Bi-material	PLA/PLA	4233.3	0.46		
77	30	Bi-material	PLA/PLA	Excluded	0.46		
78	30	Bi-material	PLA/PLA	3849.8	0.46		
79	30	Bi-material	PLA/PLA	5720.8	0.46		
80	30	Bi-material	PLA/PLA	Excluded	0.46	4203.4	981.5
81	40	Bi-material	PLA/PLA	2588.5	0.65		
82	40	Bi-material	PLA/PLA	2603.4	0.65		
83	40	Bi-material	PLA/PLA	4049.8	0.65		
84	40	Bi-material	PLA/PLA	2692.6	0.65		
85	40	Bi-material	PLA/PLA	2937.8	0.65		
86	40	Bi-material	PLA/PLA	3453.0	0.65		
87	40	Bi-material	PLA/PLA	3222.5	0.65		
88	40	Bi-material	PLA/PLA	2987.5	0.65	3066.9	467.2
89	0	Single-material	GRAY PLA	1204.0	1.0		
90	0	Single-material	GRAY PLA	1230.2	1.0		
91	0	Single-material	GRAY PLA	1241.9	1.0		
92	0	Single-material	GRAY PLA	1140.9	1.0	1204.3	39.1
93	15	Single-material	GRAY PLA	1761.0	0.78		
94	15	Single-material	GRAY PLA	1773.8	0.78		
95	15	Single-material	GRAY PLA	1798.6	0.78		
96	15	Single-material	GRAY PLA	1889.8	0.78	1805.8	50.4
97	30	Single-material	GRAY PLA	3750.3	0.46		
98	30	Single-material	GRAY PLA	N/A	0.46		
99	30	Single-material	GRAY PLA	3594.8	0.46		
100	30	Single-material	GRAY PLA	Excluded	0.46	3672.5	77.8
101	40	Single-material	GRAY PLA	2245.4	0.65		
102	40	Single-material	GRAY PLA	2548.4	0.65		
103	40	Single-material	GRAY PLA	2400.7	0.65		
104	40	Single-material	GRAY PLA	Excluded	0.65	2398.2	123.7
105	0	Single-material	RED PLA	1258.2	1.0		

106	0	Single-material	RED PLA	2158.8	1.0		
107	0	Single-material	RED PLA	1338.3	1.0		
108	0	Single-material	RED PLA	2172.6	1.0	1732.0	434.7
109	15	Single-material	RED PLA	2101.8	0.78		
110	15	Single-material	RED PLA	3312.6	0.78		
111	15	Single-material	RED PLA	2374.1	0.78		
112	15	Single-material	RED PLA	3010.6	0.78	2699.8	483.7
113	30	Single-material	RED PLA	Excluded	0.46		
114	30	Single-material	RED PLA	3668.4	0.46		
115	30	Single-material	RED PLA	Excluded	0.46		
116	30	Single-material	RED PLA	Excluded	0.46	3668.4	0.0
117	40	Single-material	RED PLA	2404.7	0.65		
118	40	Single-material	RED PLA	Excluded	0.65		
119	40	Single-material	RED PLA	2532.2	0.65		
120	40	Single-material	RED PLA	Excluded	0.65	2468.5	63.7

F Average Strain Energy Density

	Laying Red	Laying Gray	Laying Bi	Standing Gray	Standing Red	Standing Bi	Unit:
UTS	56.1	48.6	46.2	37.3	40.0	25.0	MPa
ν	0.32	0.31	0.33	0.33	0.33	0.30	
K_{Ic}	162.43	165.38	117.78	90.92	130.76	79.08	Mpa mm^0.5
K_{Ic}	5.14	5.23	3.72	2.88	4.14	2.50	Mpa m^0.5
R_c	2.17	3.07	1.62	1.49	2.66	2.67	mm
E	2949	2997	3037	3042	3217	2544	MPa
W_cr(Formel)	0.5343	0.3939	0.3517	0.2283	0.2491	0.1230	

ASED:	Laying Red	Laying Gray	Laying Bi	Standing Gray	Standing Red	Standing Bi	
0	9.62E-08	6.53E-08	1.26E-07	1.38E-07	6.93E-08	9.12E-08	mJ/mm^3
15	7.97E-08	5.40E-08	1.05E-07	1.15E-07	5.76E-08	7.54E-08	
30	5.20E-08	3.63E-08	6.70E-08	7.31E-08	1.26E-07	4.96E-08	
40	8.49E-08	5.87E-08	1.09E-07	1.19E-07	2.08E-07	8.17E-08	

Predicted Fracture Loads:	Laying Red	Laying Gray	Laying Bi	Standing Gray	Standing Red	Standing Bi
0	2357.1	2456.8	1669.7	1284.2	1895.6	1161.4
15	2589.1	2701.9	1833.9	1409.9	2079.2	1276.8
30	3206.1	3295.2	2290.6	1767.2	1404.2	1574.9
40	2508.1	2589.7	1794.0	1383.6	1093.7	1226.8

Actual Fracture Loads:	Laying Red	Laying Gray	Laying Bi	Standing Gray	Standing Red	Standing Bi
0	2151.4	2190.4	1560.0	1204.3	1732.0	1047.4
15	2472.8	2029.8	2015.9	1805.8	2699.8	2146.3
30	2945.3	3359.0	3657.1	3672.5	3668.4	4203.4
40	2206.5	2537.7	2774.6	2398.2	2468.5	3066.9

Delta	Laying Red	Laying Gray	Laying Bi	Standing Gray	Standing Red	Standing Bi		
0	9.56 %	12.16 %	7.04 %	6.64 %	9.45 %	10.88 %	Average:	-16.0448 %
15	4.71 %	33.11 %	-9.03 %	-21.93 %	-22.99 %	-40.51 %		
30	8.86 %	-1.90 %	-37.37 %	-51.88 %	-61.72 %	-62.53 %		
40	13.67 %	2.05 %	-35.34 %	-42.30 %	-55.69 %	-60.00 %		

	Laying Red		Laying Gray		Laying Bi		Standing Gray		Standing Red	
Degrees:	ELSE	EVOL	ELSE	EVOL	ELSE	EVOL	ELSE	EVOL	ELSE	EVOL
0	8.54E-06	88.8	1.16E-05	177.4	6.27E-06	49.7	5.80E-06	41.9	9.23E-06	133.2
15	7.07E-06	88.8	9.58E-06	177.4	5.20E-06	49.7	4.81E-06	41.9	7.68E-06	133.2
30	4.61E-06	88.8	6.44E-06	177.4	3.33E-06	49.7	3.06E-06	41.9	1.68E-05	133.2
40	7.54E-06	88.8	1.04E-05	177.4	5.43E-06	49.7	5.00E-06	41.9	2.77E-05	133.2

Radius:	2.17001933	3.06819186	1.62389262	1.49132269	2.65835693
E:	2949	2997	3037	3042	3217
v:	0.32	0.31	0.33	0.33	0.33

Standing Bi	
ELSE	EVOL
1.22E-05	134.0
1.01E-05	134.0
6.64E-06	134.0
1.09E-05	134.0

2.66588057
2544
0.30

Steinar Hunskaar

Structural Integrity of Bimaterials Fabricated via Fused Deposition Modeling

NTNU

Kunnskap for en bedre verden